LA-11389-T
Thesis

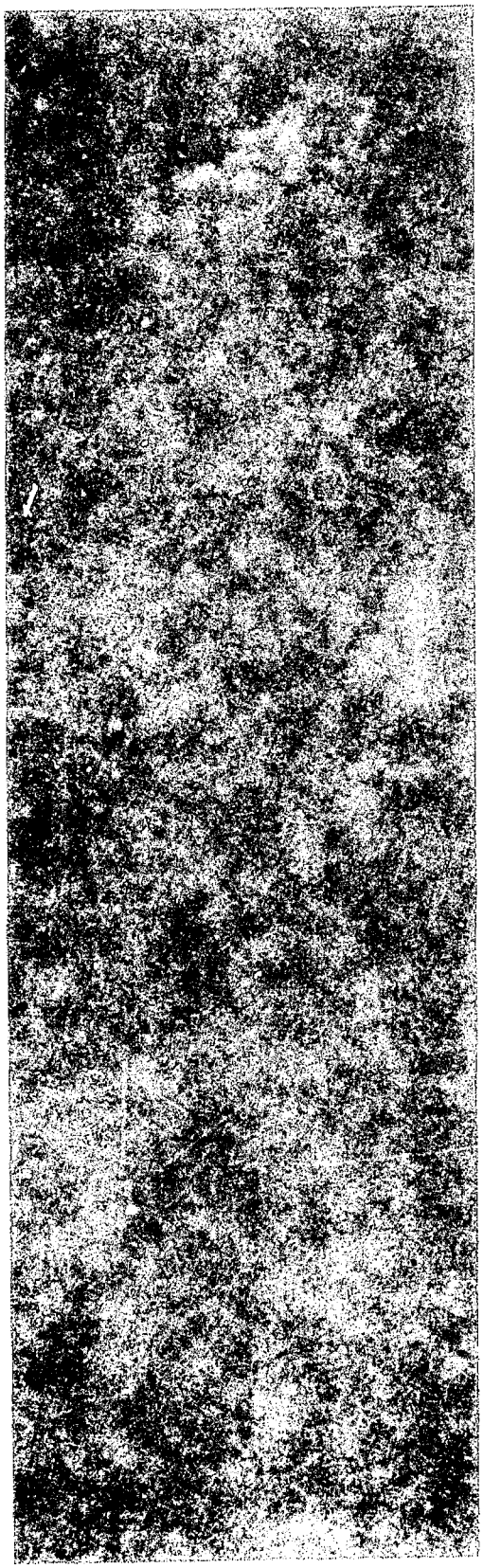

The Recoil Proton Polarization in πp Elastic Scattering

Los Alamos

Los Alamos National Laboratory is operated by the University of California for the United States Department of Energy under contract W-7405-ENG-36.

This thesis was accepted by the Graduate School of Arts and Sciences, The George Washington University, Washington, DC, in partial fulfillment of the degree of Doctor of Philosophy. It is the independent work of the author and has not been edited by the IS-11 Writing and Editing staff.

This work was supported by the US Department of Energy and the National Science Foundation.

An Affirmative Action/Equal Opportunity Employer

LA-11389-T
Thesis

UC-000
Issued: September 1988

LA--11389-T

DE88 016524

The Recoil Proton Polarization in πp Elastic Scattering

*Colin Jamie Seftor**

**Collaborator at Los Alamos. Physics Department, The George Washington University, Washington, DC 20052.*

Los Alamos National Laboratory
Los Alamos, New Mexico 87545

ABSTRACT

The polarization of the recoil proton for π^+p and π^-p elastic scattering has been measured for various angles at 547 MeV/c and 625 MeV/c by a collaboration involving The George Washington University; the University of California, Los Angeles; and Abilene Christian University. The experiment was performed at the P^3 East experimental area of the Los Alamos Meson Physics Facility. Beam intensities varied from 0.4 to 1.0 $\times 10^7$ π^-'s/sec and from 3.0 to 10.0 $\times 10^7$ π^+'s/sec. The beam spot size at the target was 1 cm in the horizontal direction by 2.5 cm in the vertical direction. A liquid-hydrogen target was used in a flask 5.7 cm in diameter and 10 cm high. The scattered pion and recoil proton were detected in coincidence using the Large Acceptance Spectrometer (LAS) to detect and momentum analyze the pions and the JANUS recoil proton polarimeter to detect and measure the polarization of the protons. Results from this experiment are compared with previous measurements of the polarization, with analyzing power data previously taken by this group, and to partial-wave analysis predictions.

TABLE OF CONTENTS

LIST OF FIGURES

LIST OF TABLES

The Recoil Proton Polarization in πp Elastic Scattering

By

Colin Jamie Seftor

INTRODUCTION

The concept of a nuclear force was developed in the 1930's after it was determined that an atom was composed of a core nucleus with electrons orbiting around it. This "strong" force was needed to explain why the nucleus does not break apart due to the electromagnetic repulsion between protons. While the existence of the strong force (now known as the hadronic force) has been known and studied for over fifty years, a complete dynamical theory has yet to be developed to describe it.

The theory that holds the most promise for providing a complete dynamical description is patterned after Quantum Electrodynamics (QED) and is called Quantum Chromodynamics (QCD). Although the structures of QED and QCD are very similar, calculations involving QCD are much more difficult due to the fact that the hadronic force is much stronger than the electromagnetic force.

In QED most calculations involve a power series expansion in the coupling constant, which is related to the strength of the interaction. The value for the QED coupling constant is 1/137, which is small enough to allow the application of perturbative methods. In QCD the value

of the coupling constant varies and is too large for perturbative calculations at all but the highest energies.

Many models (based on an underlying QCD structure) have recently been developed in an attempt to explain low-energy phenomena.[1-14] These models differ in their predictions of the location and nature of hadronic resonances (hadron spectroscopy).

To compare and test these models, phenomenological methods, usually in the form of partial-wave analyses, are used. These analyses calculate the scattering amplitudes by performing partial-wave fits to the available experimental data. The characteristics of hadronic resonances can then be determined from the values of the scattering amplitudes. For many systems, a complete set of experimental data is not available, or the data that is available is not of high quality. In such cases the unique values for the scattering amplitudes cannot be determined, and unique partial-wave solutions cannot be found. Theoretical constraints (usually in the form of dispersion relations) help to resolve sign and phase ambiguities but, since the form of such constraints vary and because each analysis may use a different data set, differences still remain.

One of the simplest hadronic systems that can be studied experimentally is the pion-nucleon (πN) system. Since the long-range part of the nucleon-nucleon (NN)

interaction is due to π-exchange, the πN interaction is of particular interest.

There are three major partial-wave analyses available for the πN system: Carnegie Mellon University-Lawrence Berkeley Laboratory (CMU-LBL),[15] Karlsruhe-Helsinki (K-H),[16] and Virginia Polytechnic Institute (VPI).[17] Since a complete data set is not yet available for this system, an unambiguous determination of the scattering amplitudes cannot be made. A complete and accurate set of experimental measurements for the πN system is therefore needed to resolve differences between these analyses. Only then can they be used to compare different models of the hadronic interaction.

A series of experiments has been performed by the same group over the last ten years to provide a complete set of πN scattering data in the region of the first two hadronic resonances, the $\Delta(1232)$-P_{33} and the $N(1440)$-P_{11}. This series marks the first time that a complete set of measurements has been made in this region. The measurements have been performed at the same accelerator, at the same momenta, and using the same beam channel. The set will therefore preclude problems involving interpolation between data taken at different momenta using pion beams of different characteristics. Such interpolations, which can lead to large systematic

uncertainties, have plagued partial-wave analyses in the past.

Measurements of the differential cross section and the analyzing power for $\pi^{\pm}p$ elastic scattering and for $\pi^{-}p \rightarrow \pi^{o}n$ have been published.[18-22] Preliminary measurements of the spin-rotation parameters for $\pi^{\pm}p$ elastic scattering have also been reported.[23]

In the experiment described here, the recoil proton polarization was measured from an unpolarized liquid hydrogen target at the following pion energies and angles:

P_{LAB} (MeV/c)	E_{LAB} (MeV)	P_{CM} (MeV/c)	E_{CM} (MeV)	Pol	θ_{LAB} (°)	θ_{CM} (°)	$\cos\theta_{CM}$
547	425	320	210	π^-	97.8	120	-0.50
547	425	358	245	π^+	81.7	105	-0.26
625	501	364	250	π^-	91.4	116	-0.43
625	501	318	208	π^-	97.0	121	-0.52
625	501	318	208	π^+	97.0	121	-0.52

These angles were chosen for the following reasons:

1) All three partial-wave analyses predict the recoil polarization to be near zero at approximately $\cos\theta_{CM} = -0.26$ for $\pi+$ at 547 MeV/c. This point therefore provides a good place to check for any instrumental asymmetries inherent in the experimental apparatus.

2) The measurement of the spin-rotation parameters required the use of a well calibrated recoil proton polarimeter in the high background

area of a secondary beam line. The measurement of the recoil proton polarization provided the calibration needed for this purpose.

3) If parity is conserved, then a measurement of the recoil proton polarization from an unpolarized target is equal to a measurement of the analyzing power of a transversely-polarized target (see Chap. 1, Sec. 1.1.2). At the angle $\cos\theta_{CM} = -0.5$ for π^- at 547 MeV/c, all three partial-wave analyses agree with each other and with this group's previous measurement of the analyzing power. By comparing the measured polarization at this point to the measured analyzing power and to the analyses, a test of the equality can be made. Conversely, by invoking the equality, the polarization measurement can be used as a check on the analyzing power measurements.

4) The measurements of the analyzing power performed by this group exhibit gaps at angles where differences between the three partial-wave solutions can be clearly distinguished. The points chosen for π^- and π^+ at 625 MeV/c fill in two of these gaps in an effort to choose unambiguously between the analyses.

Chapter 1 provides the background needed for the experiment, Chapter 2 provides a brief overview of the experiment itself, Chapter 3 explains the calibration of each experimental apparatus, Chapter 4 provides details on the analysis of the data obtained from the experiment, and Chapter 5 presents the results of the experiment and discusses their implications.

CHAPTER 1

BACKGROUND

Section 1: Formalism

1.1.1 πN Scattering

The asymptotic wave function for spinless elastic scattering can be written as

$$\langle \vec{r} | \Psi \rangle = e^{i\vec{k}\cdot\vec{r}} + f(\theta,\varphi)\frac{e^{ikr}}{r} \qquad (1\text{-}1.1)$$

where f represents the scattering amplitude. The first term on the right represents the incoming plane-wave amplitude for a particle of momentum $\vec{k}$ and the outgoing part of the plane wave that did not scatter, while the second term represents the outgoing scattered spherical wave emanating from a scattering event at the origin.

In the πN system the nucleon spin must also be taken into account (the spin of the pion is zero). The wave function can then be factored to give

$$|\Psi_\mu\rangle = |\psi\rangle|\chi_\mu\rangle$$

where $|\chi_\mu\rangle$ represents a two-component spinor for the spin-1/2 nucleon ($\mu = \pm 1/2$). The asymptotic form of the

wave function can therefore be written as

$$|\Psi_\mu\rangle = e^{i\vec{k}\cdot\vec{r}}|\chi_\mu\rangle + \frac{e^{ikr}}{r}M_{\nu\mu}|\chi_\nu\rangle \quad . \qquad (1\text{-}1.2)$$

The 2×2 matrix M, acting in a two-dimensional spin space, relates the outgoing spinor to the incident one. The scattering amplitudes are the matrix elements of M.

M can be written as a linear combination of a complete set of 2×2 matrices; the unit matrix,

$$I = \begin{bmatrix} 1 & 0 \\ 0 & 1 \end{bmatrix} \quad ,$$

and the three Pauli spin matrices,

$$\sigma_1 = \begin{bmatrix} 0 & 1 \\ 1 & 0 \end{bmatrix} \quad \sigma_2 = \begin{bmatrix} 0 & -i \\ i & 0 \end{bmatrix} \quad \sigma_3 = \begin{bmatrix} 1 & 0 \\ 0 & -1 \end{bmatrix} \quad ,$$

form such a set. M may then be written as

$$M = a_0 I + a_1\sigma_1 + a_2\sigma_2 + a_3\sigma_3$$

$$= a_0 I + \sum_{i=1}^{3} a_i\sigma_i \quad ,$$

where a_0, a_1, a_2, and a_3 are complex numbers. Since the orientation of the scattering event in space has no effect upon the outcome, the total angular momentum of the πN system is conserved. This implies that M is invariant under rotations. Therefore, the coefficients a_1, a_2, and a_3 must form a three-component vector $\vec{a}$ in order to make $\Sigma a_i\sigma_i = \vec{a}\cdot\vec{\sigma}$ a scalar.

The only two independent vectors that are available to form $\vec{a}$ are the incident pion momentum ($\vec{k}_i$) and final pion

momentum ($\vec{k}_f$). From these a third vector can be formed which is normal to the scattering plane:

$$\hat{n} = \frac{\vec{k}_i \times \vec{k}_f}{|\vec{k}_i \times \vec{k}_f|} \quad . \tag{1-1.3}$$

The most general form of M becomes:

$$M = f + g(\vec{\sigma}\cdot\hat{n}) + h(\vec{\sigma}\cdot\vec{k}_i) + j(\vec{\sigma}\cdot\vec{k}_f). \tag{1-1.4}$$

Under the time-reversal transformation,

$$\left.\begin{aligned} T\vec{k}_i T^{-1} &= -\vec{k}_f \\ T\vec{k}_f T^{-1} &= -\vec{k}_i \\ T\vec{\sigma}T^{-1} &= -\vec{\sigma} \end{aligned}\right\} \Rightarrow T\hat{n}T^{-1} = -\hat{n} \ ,$$

Hadronic interactions are invariant under time reversal, which means that M must be invariant for such a transformation. Thus, h = j.

Similarly, under the parity transformation,

$$\left.\begin{aligned} P\vec{k}_i P^{-1} &= -\vec{k}_i \\ P\vec{k}_f P^{-1} &= -\vec{k}_f \\ P\vec{\sigma}P^{-1} &= \vec{\sigma} \ ; \end{aligned}\right\} \Rightarrow P\hat{n}P^{-1} = \hat{n}$$

this implies that h = j = 0 if M is invariant under parity transformation. In this case invariance under parity transformation is more restrictive than invariance under time reversal. For other spin systems this is not necessarily true.[24]

Therefore, the most general form of M that is invariant under parity is

$$M = f + g(\vec{\sigma}\cdot\hat{n}) \qquad (1\text{-}1.5)$$

where f and g are complex amplitudes and depend on the scattering angle, θ, and the energy, and where it is assumed that f is multiplied by the 2×2 identity matrix.

The calculation of M (apart from an overall phase) requires the determination of f, g, and, since they are complex, the phase between them. Four measurements are needed to unambiguously determine these three quantities.[25] One such set of measurements includes the determination of the unpolarized differential cross section, the measurement of the recoil proton polarization using an unpolarized target (or, equivalently, the analyzing power using a transversely polarized target), and the measurement of the two spin-rotation parameters using a proton target polarized in the scattering plane. The experiment described here involved the measurement of the recoil proton polarization. For a description of the other measurements needed see App. A.

1.1.2 The Polarization-Analyzing Power Equality

The initial proton polarization is defined as

$$\vec{P}_i \equiv \frac{\langle \chi_i | \vec{\sigma} | \chi_i \rangle}{\langle \chi_i | \chi_i \rangle} \ , \qquad (1\text{-}1.6)$$

where $|\chi_i\rangle$ is the initial proton state spinor and is normalized such that

$$\langle\chi_i|\chi_i\rangle = 1 \ .$$

The differential cross section for scattering from an initial state $|\chi_i\rangle$ to a final state $|\chi_f\rangle$ can be calculated from the scattering amplitude:

$$\frac{d\sigma}{d\Omega} = |\langle\chi_f|M|\chi_i\rangle|^2$$

$$= \langle\chi_i|M^t|\chi_f\rangle\langle\chi_f|M|\chi_i\rangle \ . \qquad (1.1\text{-}7)$$

If the spin orientation of the final state is not measured

$$\frac{d\sigma}{d\Omega} = \sum_{\chi_f} \langle\chi_i|M^t|\chi_f\rangle\langle\chi_f|M|\chi_i\rangle$$

$$= \langle\chi_i|M^t M|\chi_i\rangle$$

Substituting Eq. (1.1-5) into this expression yields

$$\frac{d\sigma}{d\Omega} = \langle\chi_i|(f+g\vec{\sigma}\cdot\hat{n})^t(f+g\vec{\sigma}\cdot\hat{n})|\chi_i\rangle$$

$$= \langle\chi_i|(f^*+g^*\vec{\sigma}\cdot\hat{n})(f+g\vec{\sigma}\cdot\hat{n})|\chi_i\rangle$$

$$= \langle\chi_i|\left[|f|^2 + (f^*g+fg^*)\vec{\sigma}\cdot\hat{n} + |g|^2(\vec{\sigma}\cdot\hat{n})^2\right]|\chi_i\rangle \ . \qquad (1\text{-}1.8)$$

Now

$$\langle\chi_i||f|^2|\chi_i\rangle = |f|^2 \qquad (1\text{-}1.9)$$

$$\langle\chi_i|(f^*g+fg^*)\vec{\sigma}\cdot\hat{n}|\chi_i\rangle = (f^*g+fg^*)\langle\chi_i|\vec{\sigma}|\chi_i\rangle\cdot\hat{n}$$

$$= (f^*g+fg^*)\vec{P}_i\cdot\hat{n} \qquad (1\text{-}1.10)$$

$$\langle \chi_i | |g|^2 (\vec{\sigma}\cdot\hat{n})^2 | \chi_i \rangle = \langle \chi_i | |g|^2 | \chi_i \rangle = |g|^2 . \quad (1\text{-}1.11)$$

Substitution of Eqs. (1-1.9), (1-1.10), and (1-1.11) into Eq. (1-1.8) yields:

$$\frac{d\sigma}{d\Omega} = |f|^2 + |g|^2 + (f^* g + f g^*)\vec{P}_i \cdot \hat{n}.$$

$$= |f|^2 + |g|^2 + 2\mathrm{Re}(f^* g)\vec{P}_i \cdot \hat{n} . \quad (1\text{-}1.12)$$

If $\vec{P}_i = 0$ (corresponding to an unpolarized target), then

$$\left[\frac{d\sigma}{d\Omega}\right]_{unpol} \equiv I_o = |f|^2 + |g|^2 . \quad (1\text{-}1.13)$$

The analyzing power is defined as

$$A_n \equiv \frac{2\mathrm{Re}(f^* g)}{|f|^2 + |g|^2} , \quad (1\text{-}1.14)$$

so that

$$\frac{d\sigma}{d\Omega} \equiv I = I_o(1 + A_n \vec{P}_i \cdot \hat{n}) . \quad (1\text{-}1.15)$$

By analogy to Eq. (1-1.6) the polarization of the scattered particles can be written

$$\vec{P}_f \equiv \frac{\langle \chi_f | \vec{\sigma} | \chi_f \rangle}{\langle \chi_f | \chi_f \rangle} .$$

The final state spinor is related to the initial-state spinor through the scattering matrix,

$$|\chi_f\rangle = M|\chi_i\rangle ,$$

so that

$$\vec{P}_f = \frac{\langle \chi_i | M^{\dagger} \vec{\sigma} M | \chi_i \rangle}{\langle \chi_i | M^{\dagger} M | \chi_i \rangle} \quad . \qquad (1\text{-}1.16)$$

The denominator was already found to be equal to $d\sigma/d\Omega$ [Eq. (1-1.7)]. Substitution of Eq. (1-1.5) into the numerator of Eq. (1-1.16) gives

$$\begin{aligned} &\langle \chi_i | (f + g\vec{\sigma}\cdot\hat{n})^{\dagger} \vec{\sigma} (f + g\vec{\sigma}\cdot\hat{n}) | \chi_i \rangle \\ &= \langle \chi_i | (f^* + g^* \vec{\sigma}\cdot\hat{n}) \vec{\sigma} (f + g\vec{\sigma}\cdot\hat{n}) | \chi_i \rangle \\ &= \langle \chi_i | \left[f^* f \vec{\sigma} + f^* g \vec{\sigma}(\vec{\sigma}\cdot\hat{n}) + f g^* (\vec{\sigma}\cdot\hat{n})\vec{\sigma} + g^* g (\vec{\sigma}\cdot\hat{n})\vec{\sigma}(\vec{\sigma}\cdot\hat{n}) \right] | \chi_i \rangle \quad . \end{aligned} \qquad (1\text{-}1.17)$$

By using the identities

$$\vec{\sigma}(\vec{\sigma}\cdot\hat{n}) = \hat{n} - i(\vec{\sigma}\times\hat{n}) \quad ,$$

$$(\vec{\sigma}\cdot\hat{n})\vec{\sigma} = \hat{n} + i(\vec{\sigma}\times\hat{n}) \quad , \text{ and}$$

$$(\vec{\sigma}\cdot\hat{n})\vec{\sigma}(\vec{\sigma}\cdot\hat{n}) = 2\hat{n}(\vec{\sigma}\cdot\hat{n}) - \vec{\sigma} \quad ,$$

Eq. (1-1.17) becomes

$$\begin{aligned} &\langle \chi_i | (|f|^2 - |g|^2) \vec{\sigma} | \chi_i \rangle + \langle \chi_i | (f^* g + f g^* - 2|g|^2 \vec{\sigma}\cdot\hat{n}) | \chi_i \rangle \hat{n} \\ &\qquad + \langle \chi_i | i(f g^* - f^* g) \vec{\sigma} | \chi_i \rangle \times \hat{n} \\ &= (|f|^2 - |g|^2) \vec{P}_i + (f^* g + f g^* - 2|g|^2 \vec{P}_i \cdot \hat{n}) \hat{n} + i(f g^* - f^* g) \vec{P}_i \times \hat{n} \end{aligned} \qquad (1\text{-}1.18)$$

Substitution of Eq. (1-1.12) and Eq. (1-1.18) into Eq. (1-1.15) yields the following result for the final polarization:

$$\vec{P}_f = \frac{(|f|^2-|g|^2)\vec{P}_i + (f^*g+fg^*-2|g|^2\vec{P}_i\cdot\hat{n})\hat{n} + i(fg^*-f^*g)\vec{P}_i\times\hat{n}}{|f|^2 + |g|^2 + (f^*g + fg^*)\vec{P}_i\cdot\hat{n}} . \qquad (1\text{-}1.19)$$

If the initial polarization is zero,

$$\vec{P}_f = \frac{f^*g + fg^*}{|f|^2 + |g|^2}\hat{n} .$$

Comparing to Eq. (1-1.14),

$$|\vec{P}_f| \equiv P = A_n . \qquad (1\text{-}1.20)$$

Eq. (1-1.20) is known as the polarization-analyzing power equality. It states that a measurement of the analyzing power with a transversely-polarized target is equivalent to a measurement of the recoil-proton polarization from scattering from an unpolarized target. As can also be seen from Eq. (1-1.19), the recoil-proton polarization must be perpendicular to the scattering plane.

The equality holds only if M has the form of Eq. (1-1.5). If parity is not conserved, M will contain parity-violating terms that will produce components of $\vec{P}_f$ in the scattering plane.

1.1.3 Measurement of the Recoil Polarization

The recoil polarization can be measured by rescattering the recoil proton from a material whose spin is zero and whose analyzing power is known (such as carbon). The formalism that has already been developed can then be adapted for this system.

For the following discussion it will be assumed that the target is unpolarized, that the recoil proton will be moving along the z-axis, and that the original scattering plane defines the x-z plane. "Up" will be considered to be along the unit normal (positive y).

The z'-axis is defined to be along the direction of the proton after being rescattered by the carbon, and the x'-z' plane is defined as the rescattering plane. In general, a prime will denote quantities after the proton has been rescattered.

The direction of the momentum of the recoil proton before rescattering is therefore

$$\hat{k}_r = (0,0,1) \ .$$

The direction of the momentum of the recoil proton after rescattering becomes

$$\hat{k}'_r = (\sin\theta\cos\varphi, \sin\theta\sin\varphi, \cos\theta)$$

where θ and φ are the polar and azimuthal angles of rescattering, respectively. The normal to the rescattering

plane is defined by $\hat{k}_r \times \hat{k}_r'$:

$$\hat{n}' = (-\sin\varphi, \cos\varphi, 0).$$

Eq. (1-1.15) therefore becomes

$$\frac{d\sigma}{d\Omega} \equiv I = I_o(1 + A_C\vec{P}_r\cdot\hat{n}') \quad . \qquad (1\text{-}1.21)$$

where A_C is the analyzing power of the carbon and $\vec{P}_r$ refers to the polarization of the recoil proton. Eq. (1-1.18) shows that the polarization of the recoil proton must be perpendicular the original scattering plane:

$$\vec{P}_r = (0, P_r, 0) \quad .$$

Eq. (1-1.21) can therefore be written as

$$I = I_o(1 + A_C P_r \cos\varphi) \quad , \qquad (1\text{-}1.22)$$

If the proton is rescattered in the same plane as that of the first scatter, then φ must be equal to 0 or π. For scattering to the left, $\varphi=0$ and

$$\left[\frac{d\sigma}{d\Omega}\right]_{\varphi=0} \equiv \mathcal{L} = I_o(1+A_C P_r) \quad . \qquad (1\text{-}1.23)$$

For scattering to the right, $\varphi=\pi$ and

$$\left[\frac{d\sigma}{d\Omega}\right]_{\varphi=\pi} \equiv \mathcal{R} = I_o(1-A_C P_r) \quad . \qquad (1\text{-}1.24)$$

Dividing Eq. (1-1.23) by (1-1.24) yields

$$\frac{\mathcal{L}}{\mathcal{R}} = \frac{(1+A_C P_r)}{(1-A_C P_r)} \quad .$$

After rearranging terms:

$$P_r A_C = \frac{\mathcal{L} - \mathcal{R}}{\mathcal{L} + \mathcal{R}} \equiv \epsilon_{LR} ,$$

or

$$P_r \equiv \epsilon_{LR}/A_C \qquad (1\text{-}1.25)$$

where ϵ_{LR} is called the left-right asymmetry. Eq. (1-1.22) becomes:

$$I = I_o(1 + \epsilon_{LR}\cos\varphi). \qquad (1\text{-}1.26)$$

Eq. (1-1.26) shows that the left-right asymmetry can be determined by measuring the azimuthal angle of the rescattered event. If the analyzing power of carbon is known, Eq. (1-1.26) shows how the polarization of the recoil proton can be calculated.

If the recoil proton polarization does contain components in the x and z directions,

$$\vec{P}_r = (P_{rx}, P_{ry}, P_{rz}) ,$$

then Eq. (1-1.14) becomes

$$I = I_o(1 - A_C P_{rx}\sin\varphi + A_C P_{ry}\cos\varphi) . \qquad (1\text{-}1.27)$$

If the scattering is upward, then $\varphi=\pi/2$ and

$$\left[\frac{d\sigma}{d\Omega}\right]_{\varphi=\pi/2} \equiv \mathcal{U} = I_o(1-A_C P_{rx}) . \qquad (1\text{-}1.28)$$

If the scattering is downward, then $\varphi = 3\pi/2$ and

$$\left[\frac{d\sigma}{d\Omega}\right]_{\varphi=3\pi/2} \equiv \mathcal{D} = I_o(1+A_C P_{rx}) . \qquad (1\text{-}1.29)$$

Dividing Eq. (1-1.26) by (1-1.27) yields

$$P_{rx}A_C = \frac{D - U}{D + U} \equiv \epsilon_{DU} = -\epsilon_{UD}.$$

Substitution of the left-right asymmetry and the up-down asymmetry into Eq. (1-1.27) yields

$$I = I_o(1 + \epsilon_{UD}\sin\varphi + \epsilon_{LR}\cos\varphi) \ . \qquad (1\text{-}1.30)$$

Since the recoil proton polarization does not contain x or z components, the up-down asymmetry must be equal to zero. A measurement of this quantity provides a check on any systematic errors in the experiment.

As stated previously, this experiment determined the recoil proton polarization of an unpolarized target. Besides this measurement and a measurement of the unpolarized differential cross section, the spin-rotation parameters, A and R, must be measured for scattering from a polarized target in order to determine M and, therefore, the scattering amplitudes completely. Measurement of these parameters is discussed in App. A.

Section 2: Partial-Wave Analysis

1.2.1 Partial-Wave Expansion

The complex scattering amplitudes, f and g, depend upon the scattering angle, θ, and the incoming pion energy. In order to obtain a complete description of πN elastic scattering, $f(\theta)$ and $g(\theta)\vec{\sigma}\cdot\hat{n}=g(\theta,\varphi)$ must be determined for

all θ, φ, and pion energy.

Since no complete theory has yet been developed yet and because experimental determination of the amplitudes for all θ is not a practical possibility, phenomenological methods have been relied upon to bridge the gap. These methods generally depend upon a partial-wave expansion of the asymptotic wave function, and are discussed in App. B.

If a complete set of data (such as described in App. A) is not available, then ambiguities arise in determining the partial waves. A discussion of ambiguities is presented in App. A. Even if a complete set is available, inaccuracies in, and disagreement among, data sets makes a unique determination extremely difficult. In order to obtain such a unique solution, theoretical constraints in the form of dispersion relations are imposed on the scattering amplitudes. App. C contains a brief discussion of the dispersion relations used in πN scattering.

1.2.2 Comparisons Between Partial-Wave Analyses

The partial-wave analyses of VPI, CMU-LBL, and K-H differ in their use of experimental data and theoretical constraints. These differences provide valuable insights into how partial waves are obtained. (For definitions of the variables and amplitudes mentioned below, see Appendix B).

Carnegie Mellon University-Lawrence Berkeley Laboratory

The CMU-LBL partial-wave analysis covers the momentum range 0.43 to 2.0 GeV/c at all angles for $\pi^{\pm}p$ and $\pi^{o}p$ scattering. It consists of three stages: 1) data amalgamation, 2) partial-wave analysis, and 3) theoretical constraints for the energy dependence.

1) Data amalgamation

The momentum and center-of-mass angle ranges are divided into bins which have widths of about 50 Mev/c and 3°, respectively. Smooth momentum and angle-dependent interpolation surfaces are constructed from the original data for each data type; these surfaces cover about three adjacent momentum bins. The central bin is then shifted to the nearest multiple of θ=3° and the central momentum, k, using the surfaces. The result is a set of shifted data at 35 momenta and 61 center-of-mass angles.

2) Partial-wave analysis

The real and imaginary parts of each invariant amplitude are separately parameterized as a sum of a fixed term and a polynomial term whose coefficients are adjustable parameters to be determined in the fits. The expansion is cut off in a smooth way by adding a penalty function to the χ^2 of the fit.

3) Analyticity constraints

To determine a unique final solution, an iterative procedure is used in which the predictions from the dispersion relations along hyperbolas in the Mandelstam s, t, u plane are input into the fits. Five hyperbolas are sufficient for a resolution of all discrete ambiguities.

Karlsruhe-Helsinki

The K-H analysis is also energy-independent and covers the momentum range 0 to 10 GeV/c. Besides the experimental data, the basic input to the analysis is the forward amplitude as derived from total cross sections and forward dispersion relations for the invariant amplitude C. The fits are done to a simple partial-wave expansion and carried out using 1) fixed-t dispersion relations, 2) fixed-θ dispersion relations and 3) fixed-s dispersion relations. For the three different analyses, the data are shifted to the selected values of s, t, and θ; data whose momentum shifts were too large are omitted.

1) Fixed-t

The fixed-t analysis was carried out at 40 t-values in the range $0 > t > -1.0$ GeV^2.

2) Fixed-θ

The data were shifted to 18 center-of-mass angles in the range $-0.9 < \cos\theta < 0.8$.

3) Fixed-s

A total of 92 values of momenta were used in the range $0 < k < 200$ GeV/c.

The three analyses are iterated simultaneously until the amplitudes agree to within 3%.

Virginia Polytechnic Institute

The VPI partial-wave analysis is an energy dependent fit where all partial waves are determined simultaneously in the momentum range $0 < k < 1.2$ GeV/c.

All data contributing a χ^2 greater than 6 for π^+p scattering and 5 for π^-p scattering are eliminated in the fits. The remaining data is then fit using an empirical parameterization; predictions for the forward amplitude from dispersion relations are used as part of the input.

To insure that the energy-dependent fit does not smooth over significant structure in the amplitudes, single energy analyses are also done at 23 energies from 0.3 to 1.1 Gev.

Any systematic variations between the single-energy partial waves and those of the energy-dependent partial waves indicate structure not properly encoded in the energy dependent fit; the energy dependent fit is then modified to reflect the structure.

CHAPTER 2

THE EXPERIMENT

Section 1: The Accelerator

The experiment was performed at the Clinton P. Anderson Meson Physics Facility (LAMPF). LAMPF is a high-intensity (typically between 800 and 1000 μA), half-mile long linear proton accelerator. Three beams are available at LAMPF: H^+ (protons), H^- (hydrogen atoms with an extra electron), and P^- (polarized H^-). The facility utilizes a three-stage linear accelerator that can simultaneously accelerate the H^+ beam and either the H^- or P^- beam.

The first stage is an injector which produces and accelerates the beams to 750 keV. Sources for the beams are pulsed at 120 Hz, while each beam pulse is 570 μsec long, giving a duty factor of about 7% for the accelerator (i.e., the beam is on only for 570 μsec every 8.33 msec). Higher duty factors are possible and are achieved by lengthening the macropulses.

The second stage consists of Alvarez-type drift tubes, which accept ions from two of the three injectors and accelerate them to 100 MeV. The drift tubes operate at a

frequency of 201.25 MHz, giving the beam a microstructure; each of the 570 μs long macropulses consist of "micro buckets" every 4.97 ns.

The 100 MeV ions are sent to the third stage, where side-coupled cavity waveguides are used to boost their energy to a maximum of 800 MeV. The energy of the beam can be step-wise varied from 100 MeV to 800 MeV.

The H^+ and H^- (or P^-) beams then enter the switchyard, where they are magnetically separated and directed to four main lines, with Area A receiving most of the H^+ (proton) beam. The beam switchyard and the various experimental areas are shown in Fig. 2-1.

The experiment was performed in the P^3E channel of Area A, which is shown in Fig. 2-2. Pions are produced on a carbon production target (designated A-2 on the figure) that is oriented at 20° with respect to the primary proton beam. Three dipoles provide momentum selection, momentum dispersion for selecting the momentum bite, and switching to either the P^3E or P^3W experimental channels; the layout for both channels is shown in Fig. 2-3. Focusing for the P^3E channel is accomplished by six quadrupole doublets and the beam phase space is controlled by two horizontal and two vertical slits. Details of the channel can be found in Ref. 26. A seventh quadrupole doublet and two steering magnets have been installed the work of Ref. 26 was performed. The final focusing done by these magnets helped

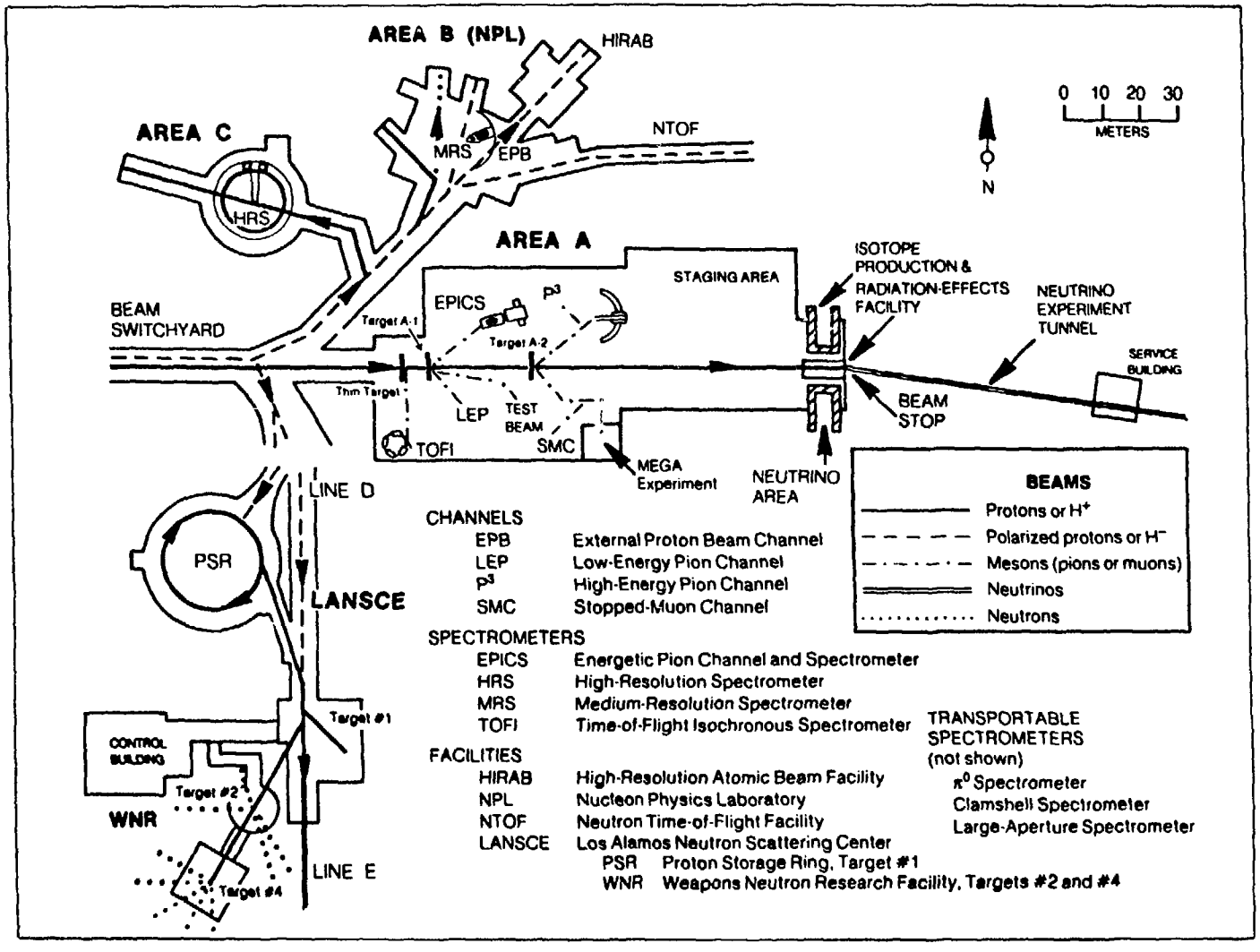

Figure 2-1

LAMPF Beam Switchyard and Experimental Areas

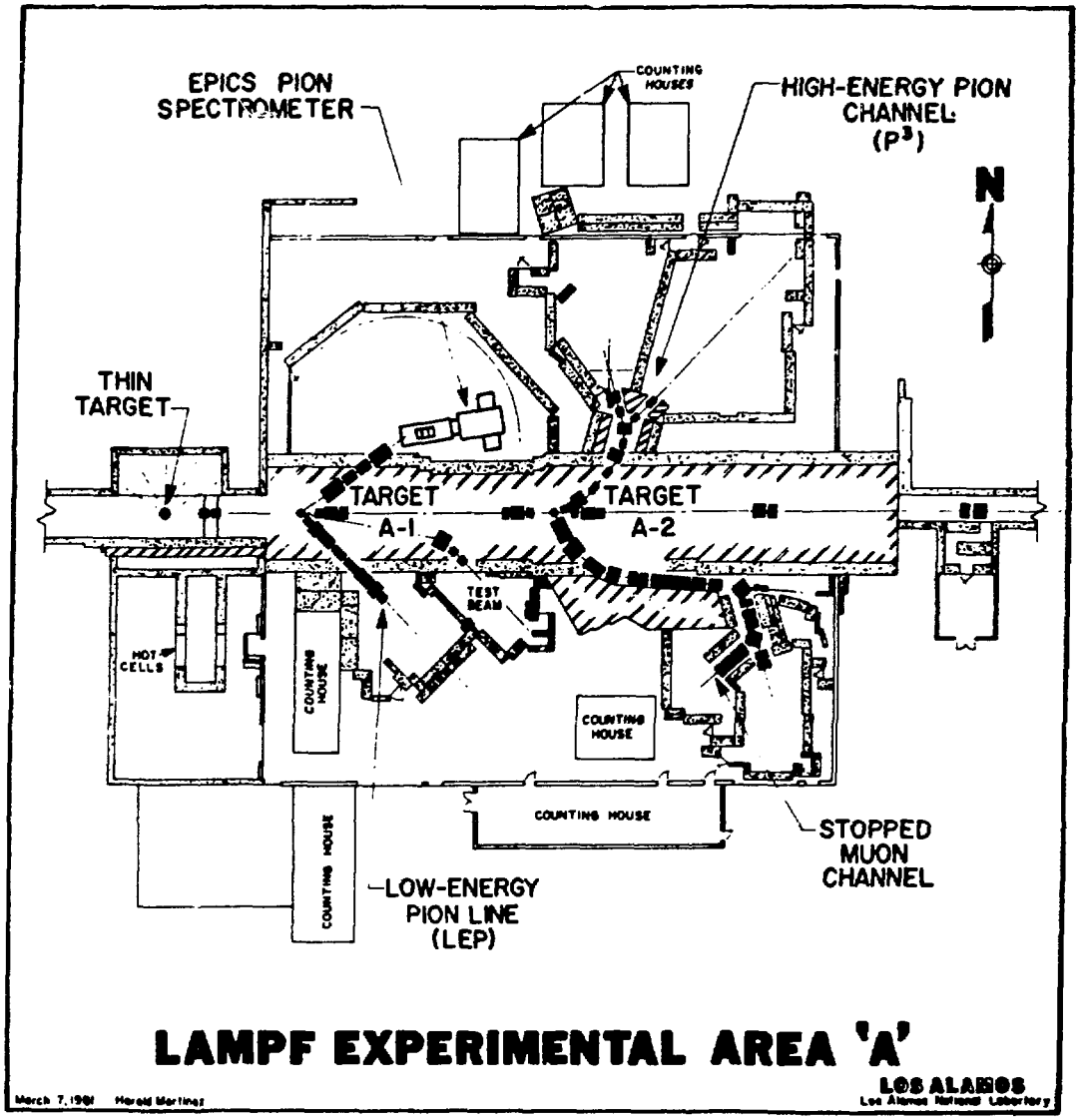

Figure 2-2

LAMPF Experimental Area A

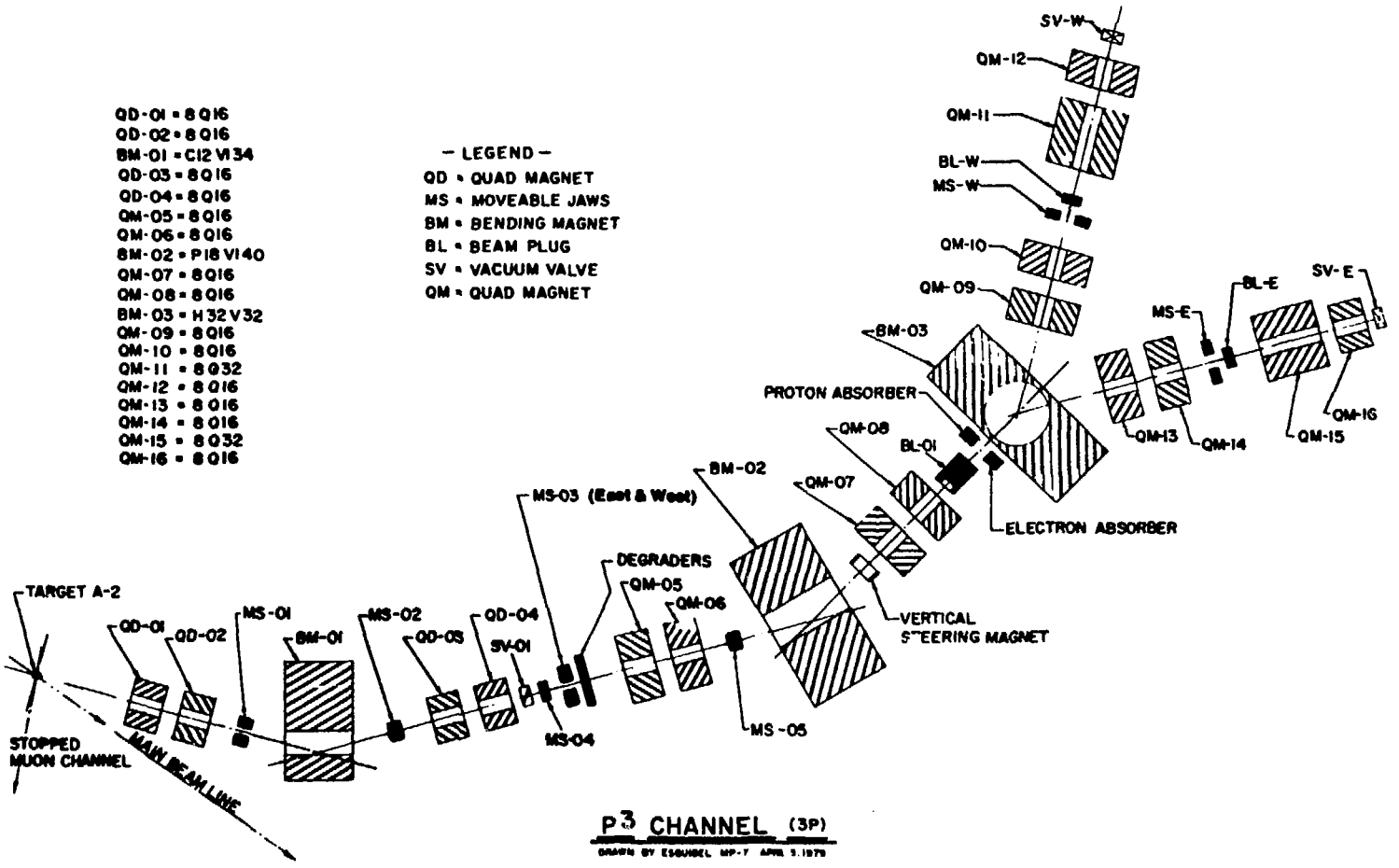

Figure 2-3

The Particle and Pion Physics (P^3) Beam Channels

to provide a small beam spot at the target at higher intensities than those possible without the doublet. Details of the beam characteristics are given in Ref. 26. A summary of the pion beam characteristics is given in Table 2-1.

Section 2: The Experimental Setup

The layout of the experimental setup is shown in Fig. 2-4. The incident pion was scattered from a liquid hydrogen (LH_2) target; the Large Acceptance Spectrometer (LAS) was used to detect and momentum analyze the pion after scattering. The recoil proton was detected and its polarization measured by the JANUS polarimeter.

In order to check for systematic errors, it was desirable to have at least one set of measurements in which JANUS was placed at the same angle on either side of the beam line. Because the LAS could not be moved to the positions necessary to take measurements on the left side of the beam (see Sec. 2.2.3), a set of measurements, performed for π^+ at an incident pion beam energy of 547 MeV/c, used a two-scintillator pion telescope in place of the LAS. The telescope and JANUS were then switched to the side of the beam line opposite to their original positions midway into the collection of this data set.

TABLE 2-1

PION BEAM CHARACTERISTICS

Beam Mom (MeV/c)	Pol	Rate (10^7 π/s)	$\Delta p/p$ (%)	Spot Size (cm)
547	π^-	1.0	1.0	1.5×2.5
547	π^+	10.0	1.0	1.5×2.0
625	π^-	0.4	2.0-3.0	1.0×2.0
625	π^+	3.0	3.0	1.0×1.5

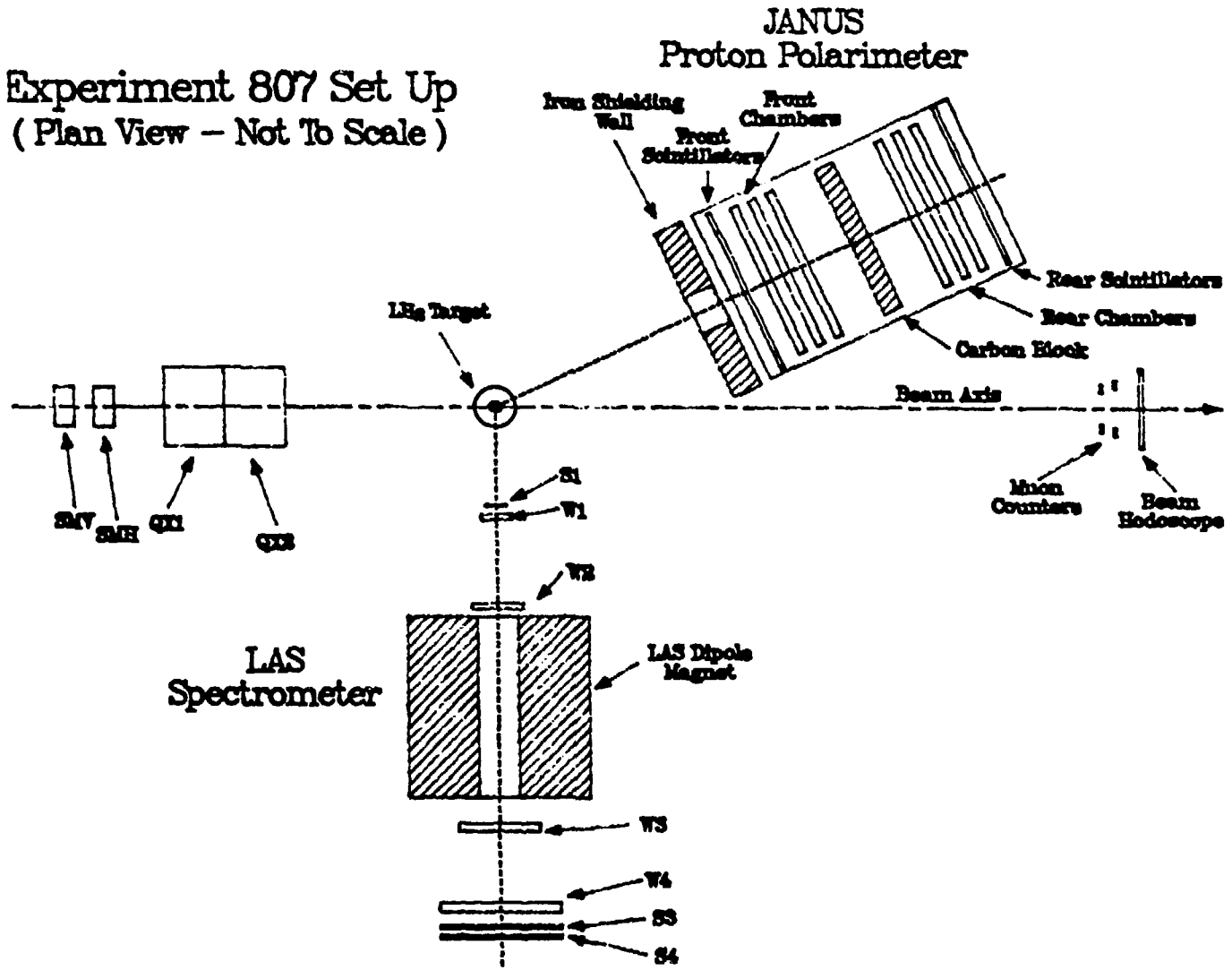

Figure 2-4

The Experimental Setup

Data were also taken with the LAS at the same beam momentum for comparison purposes.

2.2.1 Beam Monitors

Two particle telescopes and a beam hodoscope were used during the experiment to monitor the beam characteristics. Both telescopes consisted of two scintillation counters set at an angle of approximately 3° from the beam line and looking at the target. They monitored the beam intensity by looking at the muon halo produced by the decay of pions in the beam. The front counters were 4.5 cm by 4.5 cm. The back counters were approximately 22 cm behind the front ones and were 10.2 cm by 10.2 cm. All four counters were 0.64 cm thick.

The beam hodoscope monitored any beam drift. It consisted of four 10.2 cm by 10.2 cm, 0.64 cm thick counters. Two of the counters were placed on either side of the beam and slightly below beam height. The other two counters were placed the same distance to either side of the beam as the first two but slightly above beam height.

2.2.2 The Target

The experiment used a cryogenic LH_2 target system. The system consisted of two parts: 1) a LAMPF standard refrigerator system and 2) a target flask.

The refrigerator was a CTI Model 1020 with a nominal cooling capacity of 10 Watts at 20 K. It was fitted with a

condensing chamber for the liquid hydrogen, a reservoir for the condensed liquid, and a remotely operated valve in the vapor return line between the target flask and the condensing chamber.

In normal operation the target flask was filled with liquid hydrogen and there was an additional small amount of liquid, approximately 0.22 liters, in the reservoir. The target flask had carbon-resistor level sensors to indicate full and empty conditions; the reservoir had level sensors at 0.22 liters and every 0.1 liters thereafter. Vapor generated by heating in the target flask returned to the condenser to be recondensed.

The characteristics of the target flask are given in Table 2-2.

2.2.3 The LAS Spectrometer

As shown in Fig. 2-5, the LAS consisted of a dipole bending magnet sandwiched between four sets of multi-wire proportional chambers (MWPC's). The bend plane was vertical, with a nominal bend of 30°. The LAS rolled on a leveled semi-circular steel track and could be positioned at any angle between 0° and approximately 150° in the horizontal plane (chosen as the x-z plane).

The dimensions and wire spacings of the MWPC's are given in Table 2-3. All chambers were delay-line readout chambers, whereby the point at which a particle passes

TABLE 2-2

TARGET FLASK CHARACTERISTICS

Geometry	Cylindrical Mylar body with metal caps (symmetry axis trans to beam dir)
Window Material	Mylar
Window Thickness	0.005 in
Window Length	3.00 in
Window Width	2.25 in diameter
Liquid Capacity	0.35 liters
Normal Operating Pressure	14.0 psia
Insulation	10 layers 0.00025 in Super Insulation on window area with 0.125 in around center

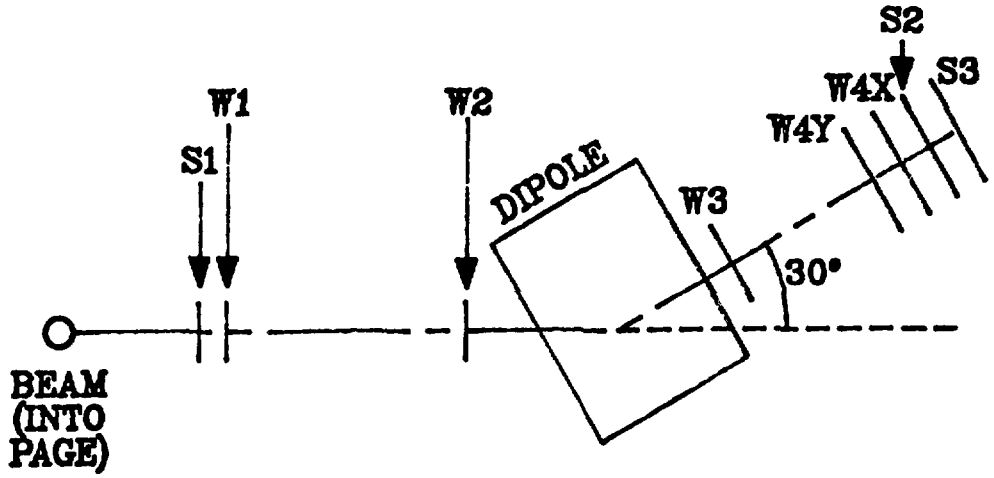

Figure 2-5

The LAS Spectrometer

TABLE 2-3

LAS WIRE CHAMBER DIMENSIONS

Chamber Plane	Active Area (hor×ver cm)	Wire Spacing (cm)
X1	12.7×12.7	0.2
Y1	12.7×12.7	0.1
X2	29.2×40.6	0.2
Y2	29.2×40.6	0.2
X3	35.6×56.0	0.2
Y3	35.6×56.0	0.2
X4	40.6×81.3	0.4
Y4	40.6×81.3	0.2

through is determined by measuring the time difference between pulses reaching two ends of a delay line to which the wires are attached. Chambers W1 and W2 were located before the dipole magnet. Each chamber contained one plane of signal wires to determine the x-position and one plane to determine the y-position. The chambers provided the information necessary to determine the track of the pion before it entered the field of the dipole magnet. Chambers W3 and W4 were located behind the magnet and were used to determine the track of the pion after leaving the field of the magnet. Chamber W3 also contained one plane of wires for determining the x-position and one plane to determine the y-position. However, the delay line connected to the y-plane was split into two segments; the position information obtained from the two segments was smoothly joined together in the computer software. Chamber W4 was actually two different chambers, one containing the x-plane wires and one containing the y-plane wires. In this case, the delay line for the y-plane was split into three segments while the delay line for the x-plane was split into two segments; again, position information from the different segments were joined together in the software. A standard "magic" gas formulation of 62% argon, 38% isobutane, 0.1% isopropyl alcohol, and .03% freon was used for all the chambers.

The momentum was calculated from the pion track information from the wire chambers. A front scintillation counter and two scintillator planes (each composed of five overlapping counters) in the back provided time-of-flight and pulse-height information. Coincidence between the front scintillator and the back scintillator planes was used to signal that a potentially good event occurred in the LAS.

2.2.4 The Pion Telescope

The pion telescope used for the measurements performed at 547 MeV/c consisted of the front LAS scintillator, S1, in coincidence with a scintillation counter, PS2, placed 60 cm behind S1. The dimensions of PS2 were 10.2 cm by 10.2 cm by 0.64 cm thick.

2.2.5 The JANUS Polarimeter

Coincidence between front and back scintillator planes located on JANUS signaled the potential for a good event in JANUS. Along with pulse-height information obtained from these planes, the time-of-flight difference was recorded between the front plane of JANUS and the front counter of the LAS. For the set of runs at 547 MeV/c π^+, time of flight was recorded between the front plane of JANUS and the front scintillator of the pion telescope.

In addition to the front and back scintillator planes, JANUS contained three multi-wire drift chambers, a carbon

analyzer, and three more chambers. The three chambers in front provided proton track information before the analyzer while the three rear chambers provided track information after the proton had been rescattered from the carbon. Again, standard "magic" gas was used in the chambers. An iron shielding wall with a hole matching the acceptance of the LAS was installed in front of JANUS to reduce the background in the chambers. A schematic of JANUS is shown in Fig. 2-6.

A schematic diagram of the inside wire arrangement of a JANUS chamber plane is shown in Fig. 2-7. Each of the six chambers had a nominal active area of 60 cm by 60 cm and consisted of two wire planes (one used to determine the x-position and one the y-position), three cathode planes, and two cover plates. The sequence was cover, cathode, x-position plane, cathode plane, y-position plane, cathode plane, and cover. The wire planes consisted of alternating anode and cathode (also known as field-shaping) wires that were evenly spaced with a 0.4064 cm separation. Each anode wire was attached to a 200 ns delay line. The cathode wires were alternately attached to two bus lines, referred to as odd and even, so that the pulses induced on the cathode wires on either side of an anode wire could be distinguished. The difference between the two pulse heights was then used to determine on which side of a wire an event occurred (see Chap. 3).

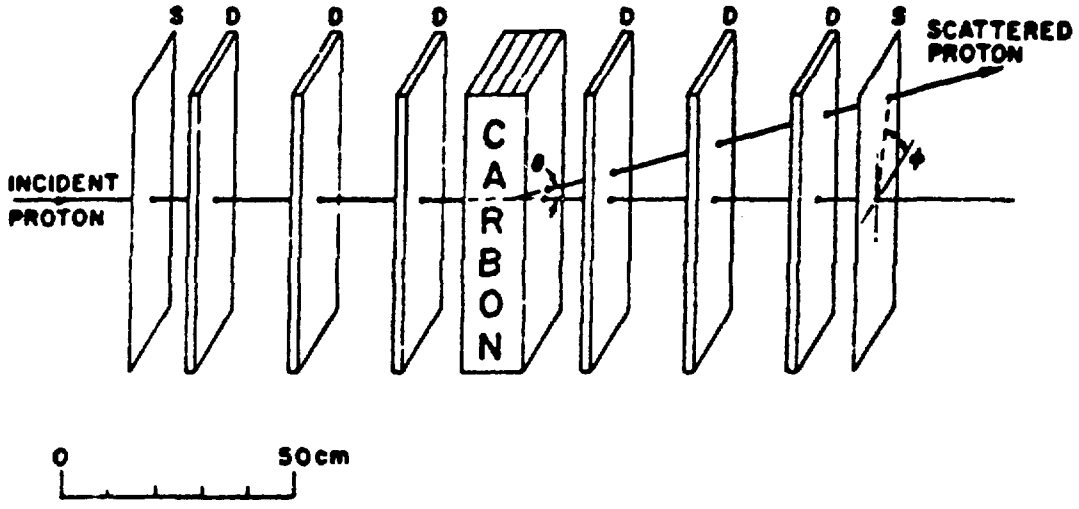

Figure 2-6

The JANUS Polarimeter

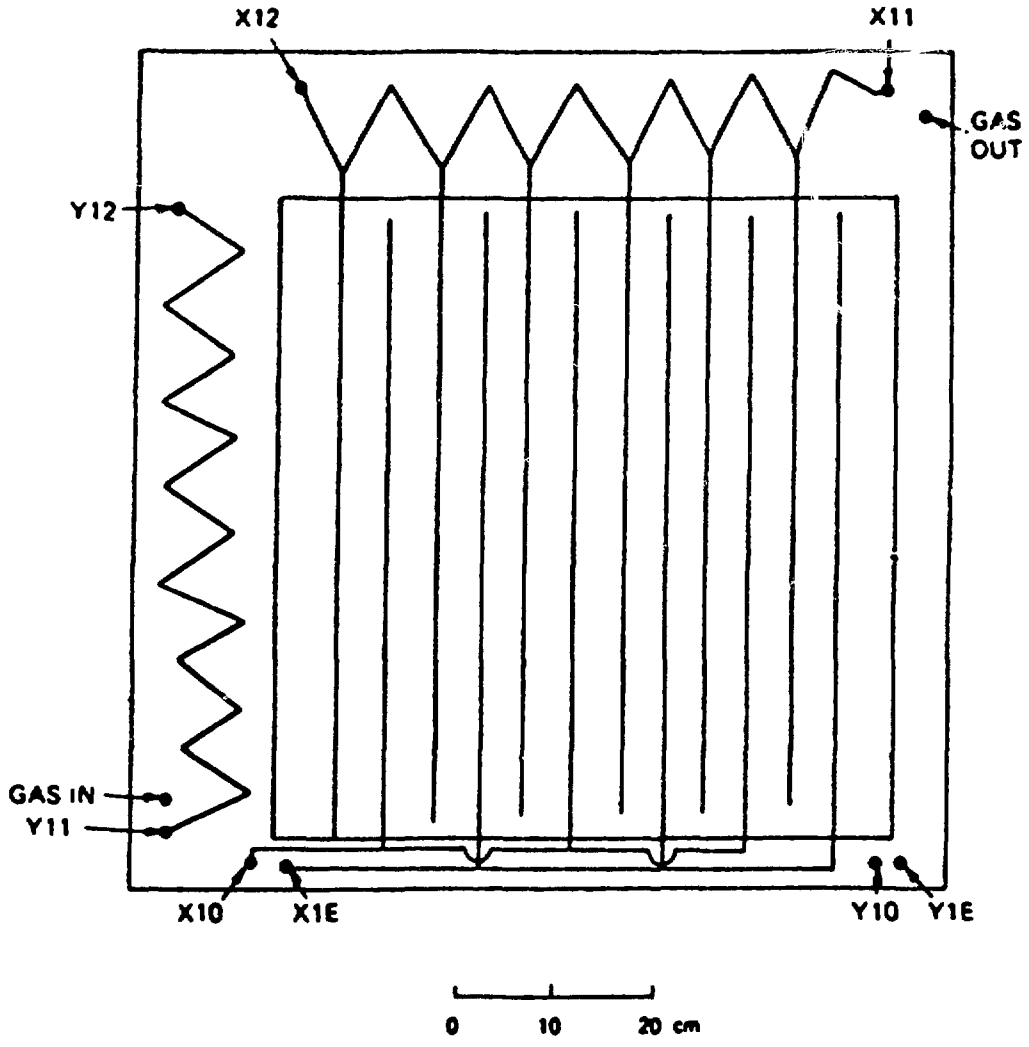

Figure 2-7

Inside Wire Arrangement for a JANUS Wire Chamber

2.2.6 Data Acquisition and Software

The data acquisition components consisted of a computer, a Micro-programmable Branch Driver (MBD), and CAMAC and NIM electronic modules. A Digital Equipment Corporation (DEC) PDP-11/45 minicomputer with 124 K words of memory was used for on-line data processing, while the MBD handled the transfer of data from the electronics to the main computer.

Data for each event were obtained from the NIM analog modules and converted into 120 16-bit integers by CAMAC analog-to-digital (ADC), time-to-digital (TDC), and scaler modules. CAMAC delivered these data to the MBD, which buffered the data until it was released to the computer. After receiving an event, the MBD reset the CAMAC modules to make the system ready for the next event; meanwhile, events from the buffer were transferred by the MBD to the computer and subsequently recorded onto magnetic tape.

The events were routed to the MBD via the LAMPF Event Trigger Module, which has a series of inputs labelled 4 to 11. Whenever a NIM signal was received at one of the inputs to the trigger module, the corresponding input was triggered. Two inputs were used during the course of this experiment. Input 6 was used as the main event trigger; it was triggered by the master trigger described below.. Input 7 was used to read the scalers and was triggered by a

pulse generator. Whenever either event was triggered, the data corresponding to that event were read and then written to tape. The data record included the run number, event number, and the number of data words in the event.

The computer was run in "MAY PROCESS" mode. In this mode all incoming events are written onto tape, but an event is processed on-line only if time is available (meaning that the computer is not busy). There are two advantages of running this way: first, the tape can be replayed later and all the events that were recorded may be retrieved, and second, fewer events are lost due to computer dead time.

The analysis was performed using the Q data acquisition and analysis system developed at LAMPF.[27] The data processing was done with a program called the event analyzer. During a data run the analyzer indicated what data should be acquired from CAMAC in response to an event trigger and what analysis was required on these data.

Q allows users to change the values of various parameters and flag settings during the course of a data run. The user can therefore see the effect of such a change during real time. In this experiment, these parameters contained all the factors necessary for the calibration of both the LAS and JANUS chambers. Also included is a display package that allows the user to histogram or dot-plot any of the raw information being

processed, or any quantities calculated from this information, in real time. Another feature included in the Q system is a package that allows the user to place tests on any of the data words being recorded. These tests can take the form of cuts as well as logical AND, OR, or NOR combinations of previous tests in the package, and any histogram or dot-plot may be gated from any test in the package.

Section 3: Electronics

The electronic circuits used to provide information to the computer for each event can be conveniently divided into the following:

1) The beam monitor circuit,
2) The LAS wire chamber circuit,
3) The LAS event trigger circuit,
4) The JANUS wire chamber circuit,
5) The JANUS event trigger circuit, and
6) The master event trigger circuit.

2.3.1 The Beam Monitor Circuit

In the beam monitor circuit (shown in Fig. 2-8) the signals from the beam hodoscope counters were first fed into discriminators located in the counting house and then sent directly into scalers. Signals from the two counters

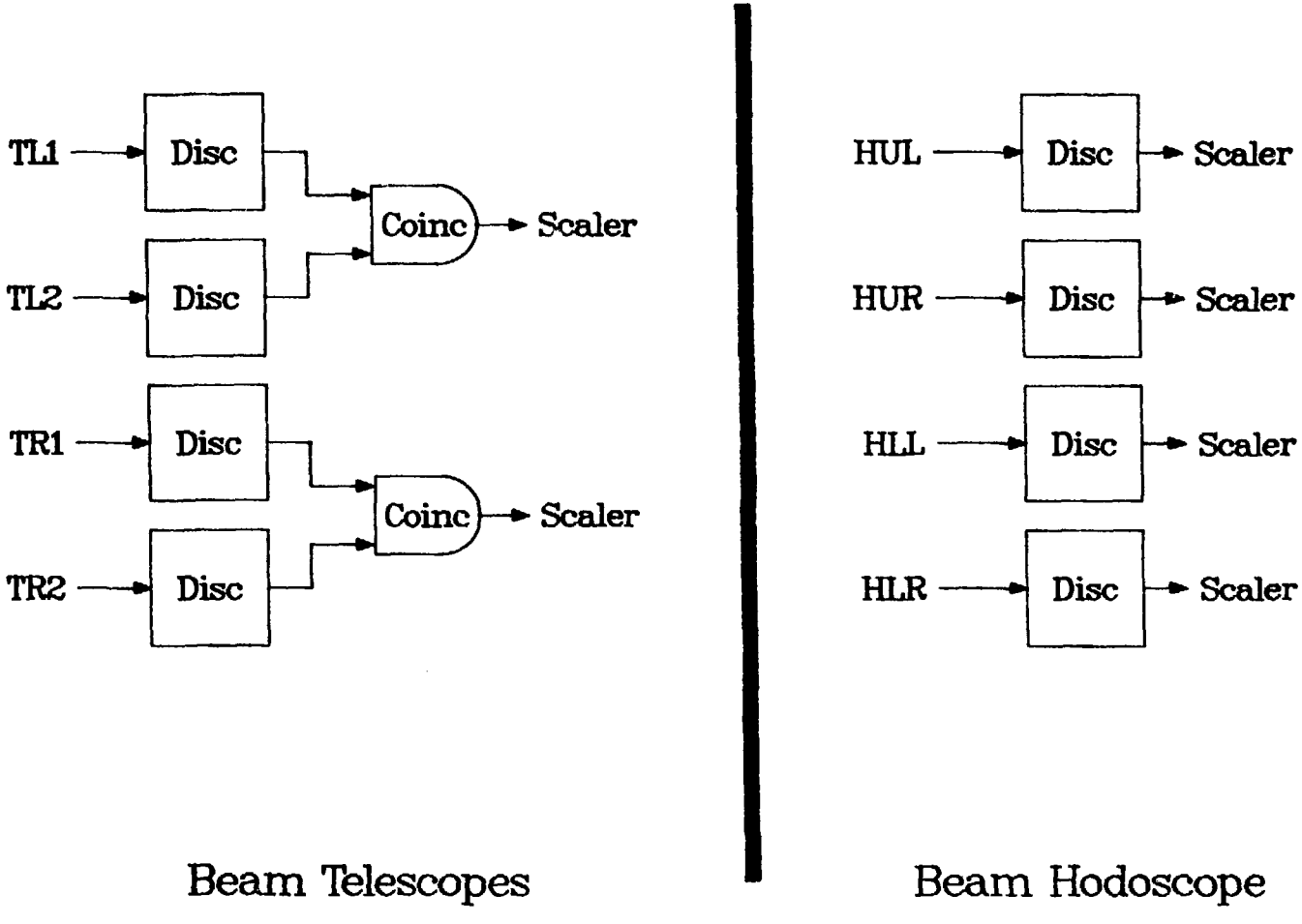

Figure 2-8

The Beam Monitor Circuit

in the telescope were also fed into discriminators. The two signals were then sent to a coincidence module which determined if there was a coincidence between them; if so, the module sent out its own signal. The output signals of the coincidence modules from both telescopes were then sent to scalers.

2.3.2 The LAS Wire Chamber Circuit

Since high voltage was fed to the wire chambers along the same delay line as the signal being processed, a decoupler was attached to both ends of the line so that the signal could be separated from this voltage. From the decoupler, the signal proceeded to an amplifier and then to a constant fraction discriminator; both were located on the spectrometer. The signal was then carried approximately 100 feet by 50 ohm, low-loss cable into the P^3E counting house. To reshape the pulse after attenuation through the cable, the signal was fed into another discriminator for retriggering; the signal was finally delivered to a scaler and to a TDC stop. A schematic diagram of the LAS electronics (for one chamber) is shown in Fig. 2-9.

2.3.3 LAS Event and Pion Telescope Trigger Circuit

The LAS event trigger circuit and counter designations are shown in Fig. 2-10. The trigger for the LAS consisted of a coincidence between the front scintillator (labelled

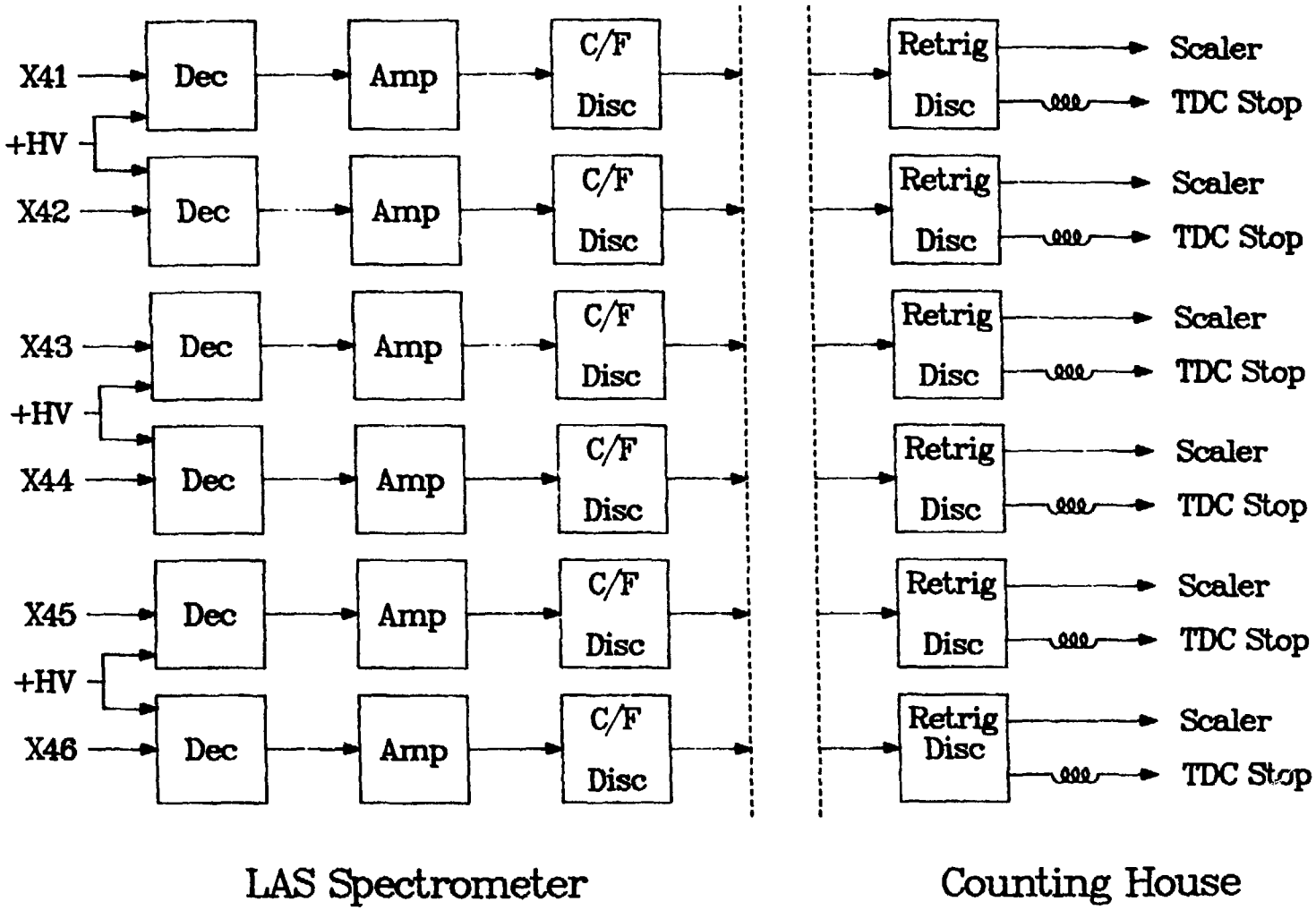

Figure 2-9

The LAS Wire Chamber Circuit

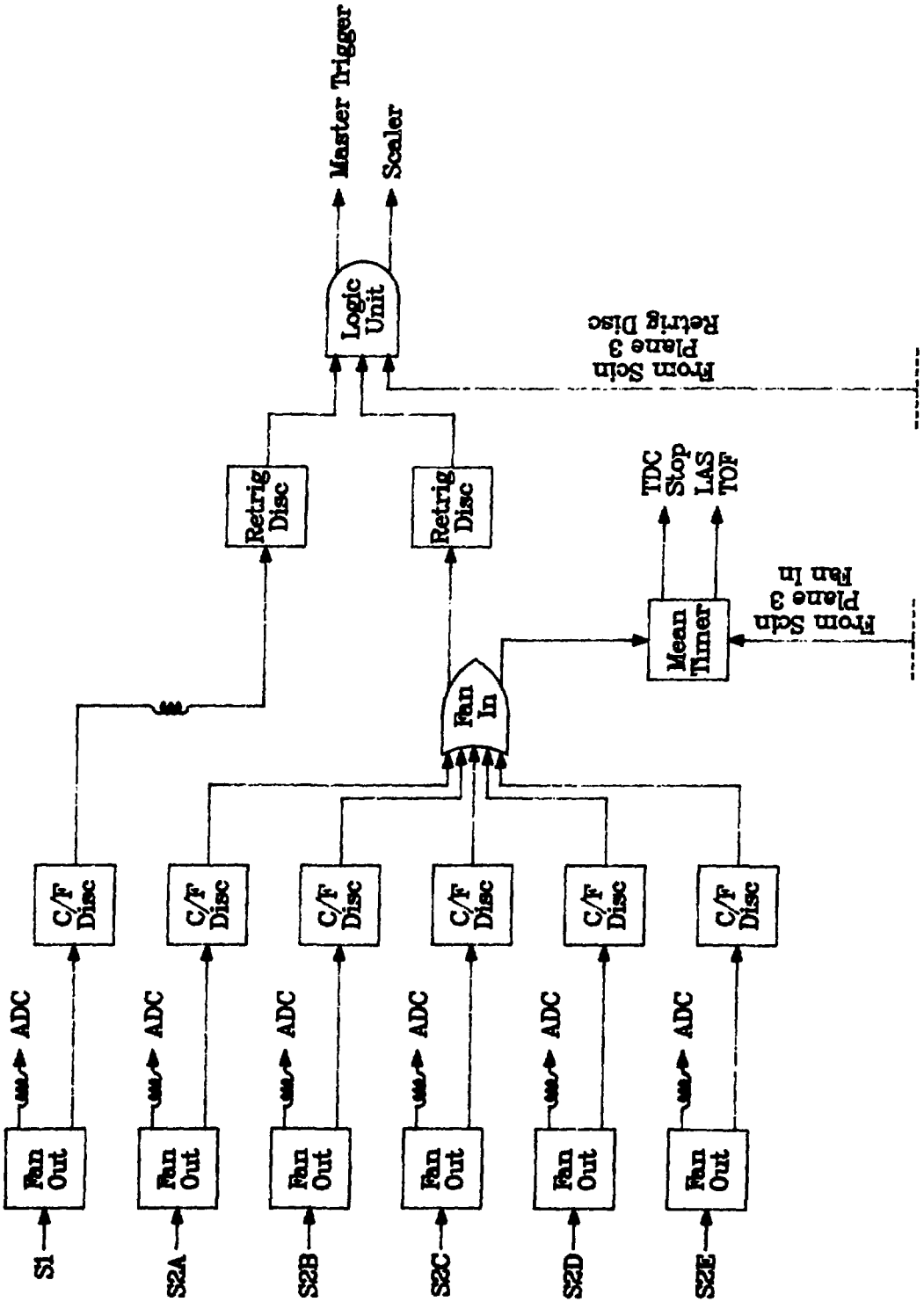

Figure 2-10

The LAS Event Trigger Circuit

S1) and the rear scintillator planes (labelled S2A-E and S3A-E, respectively).

The signal from each scintillator was passed through a linear fan-out where the signal was split; one output of each fan-out was delivered to an ADC located in the counting house while another output was sent to a discriminator located on the LAS. One of the outputs from each of the discriminators was sent to a scaler inside the counting house. For the front scintillator, a second output from the discriminator was used as a TDC start. A second output was also needed for the second and third scintillator planes. The outputs for counters 2A through 2E were sent to a logical fan-in; the fan-in would send out a signal if it received a signal from any one of the counters. The output signals from counter 3A through 3E were similarly treated. These two signals, along with the signal from S1, were then fed into retriggering discriminators in the counting house and then into a coincidence module. The output from the coincidence module then went to a scaler and to the master event trigger. Another set of signals from the fan-ins for S2 and S3 were sent to a meantimer; the signal from the meantimer was then sent to stop the TDC of S1 in order to obtain time-of-flight information.

The trigger circuit for the pion telescope used the coincidence circuit already set up for the LAS trigger

circuit; the signals from the back planes were simply replaced by the signal from PS2 of the pion telescope.

2.3.4 The JANUS Wire Chamber Circuit

The electronics used on the anode wires of a JANUS chamber was similar to the electronics used on the LAS chambers: the signal was first decoupled from the high voltage, then sent to an amplifier and a discriminator located on JANUS, and finally sent to the P^3E counting house, where it was fed into a retriggering discriminator and then to a scaler and a TDC stop (see Fig. 2-11a).

The electronics used on the cathode wires was different than that used for the anode wires. The signals from both the "odd" and "even" wires were fed into a differential amplifier on JANUS, and the sums and the differences of these signals were produced. The summed signal (O+E) was carried to the counting house, where it was fed into a retriggering discriminator and then to a TDC stop and to one of the gates of a separate-gate analog-to-digital converter (ADC); this type of ADC has a separate gate for each input signal, hence the name. The difference between the two signals (O-E) was carried to the counting house and into the ADC for which the (O+E) signal was used as the gate. This circuit is shown in Fig. 2-11b.

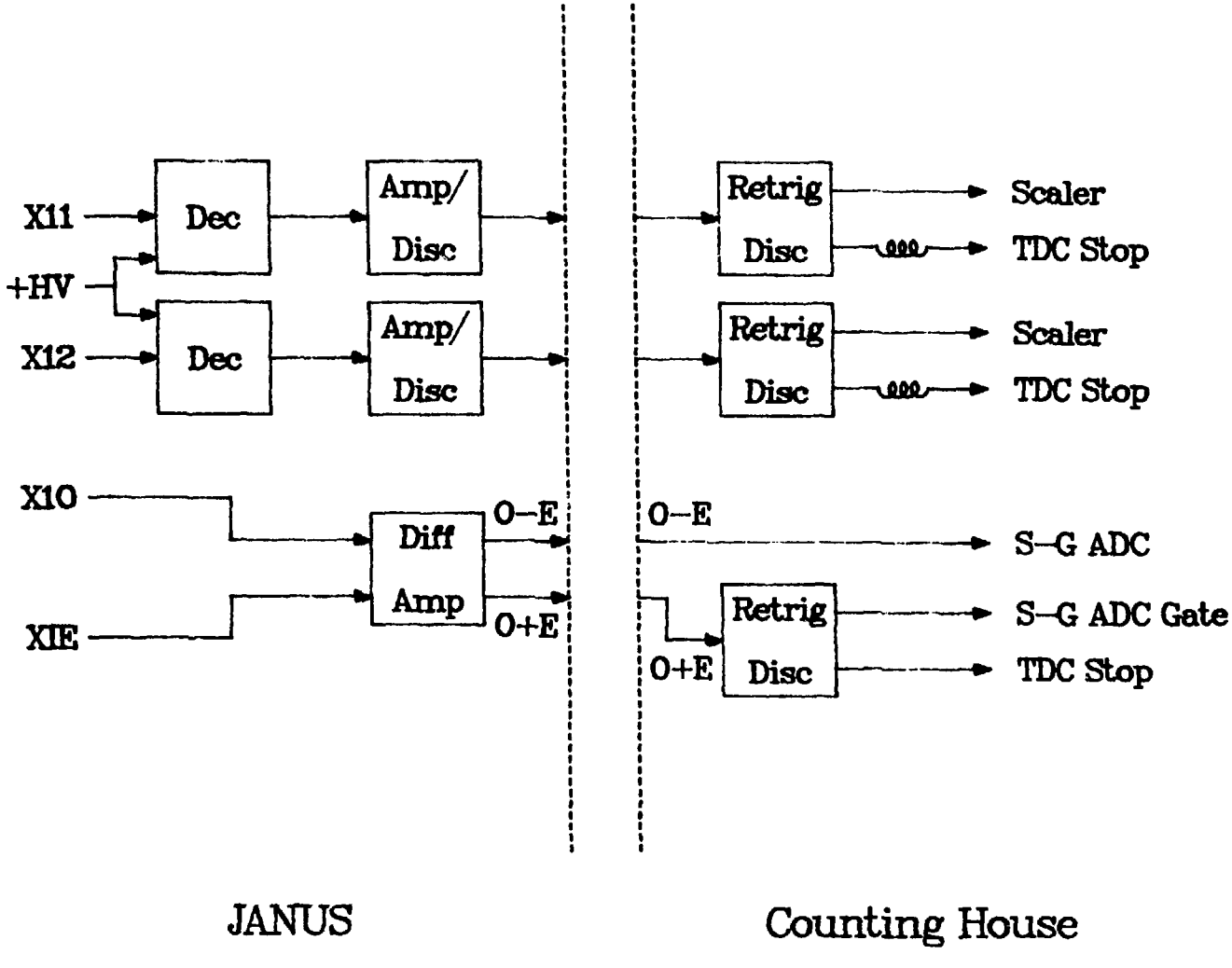

Figure 2-11

The JANUS Wire Chamber Circuits

2.3.5 The JANUS Event Trigger Circuit

Fig. 2-12 shows the JANUS event trigger circuit along with the front and back counter designations. Two double-ended counters made up the front plane and two made up the rear. A phototube was attached to each end of each scintillator. All of the signals from the phototubes were fed into the counting house before being processed. The signals were first split into two; one of the two signals went directly to an ADC while the other was fed into a discriminator. The discriminated signals from the two ends of the same scintillator were fed into a meantimer. The outputs of the meantimer for both the upper and lower counter in the plane were then fed into a logic unit; if the unit received a signal from either meantimer it would send out a signal. A signal from the logic unit for the front plane was used as a TDC start; the stop for this TDC was provided by the front LAS scintillator and provided time-of-flight information. Signals from the logic units for both planes were sent to a coincidence register. The signal from the register then went to a scaler and to the master event trigger.

2.3.6 The Master Event Trigger Circuit

The master event trigger circuit is shown in Fig. 2-13. The trigger was composed of four elements: the beam gate, the run gate, a coincidence between the LAS and

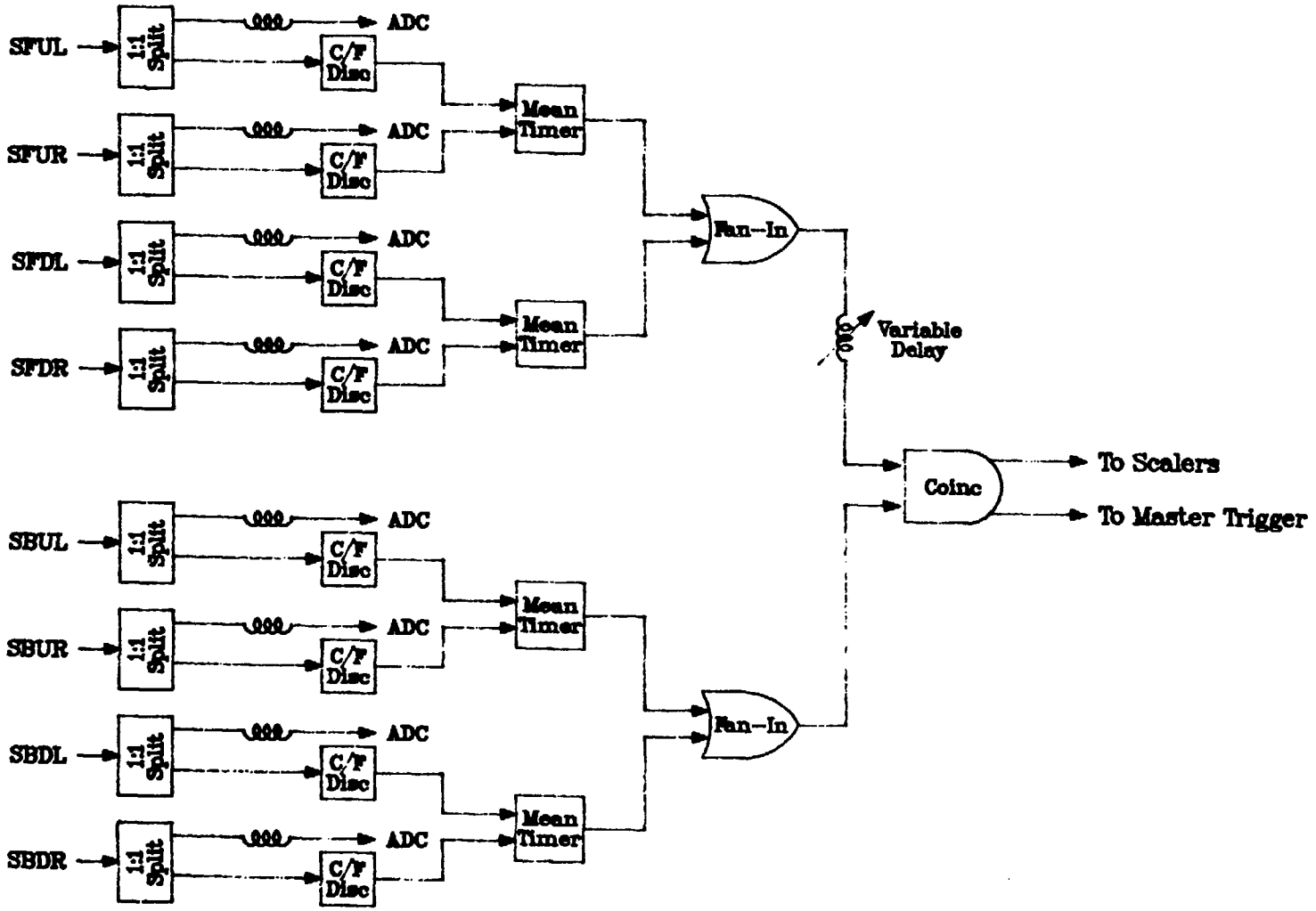

Figure 2-12

The JANUS Event Trigger Circuit

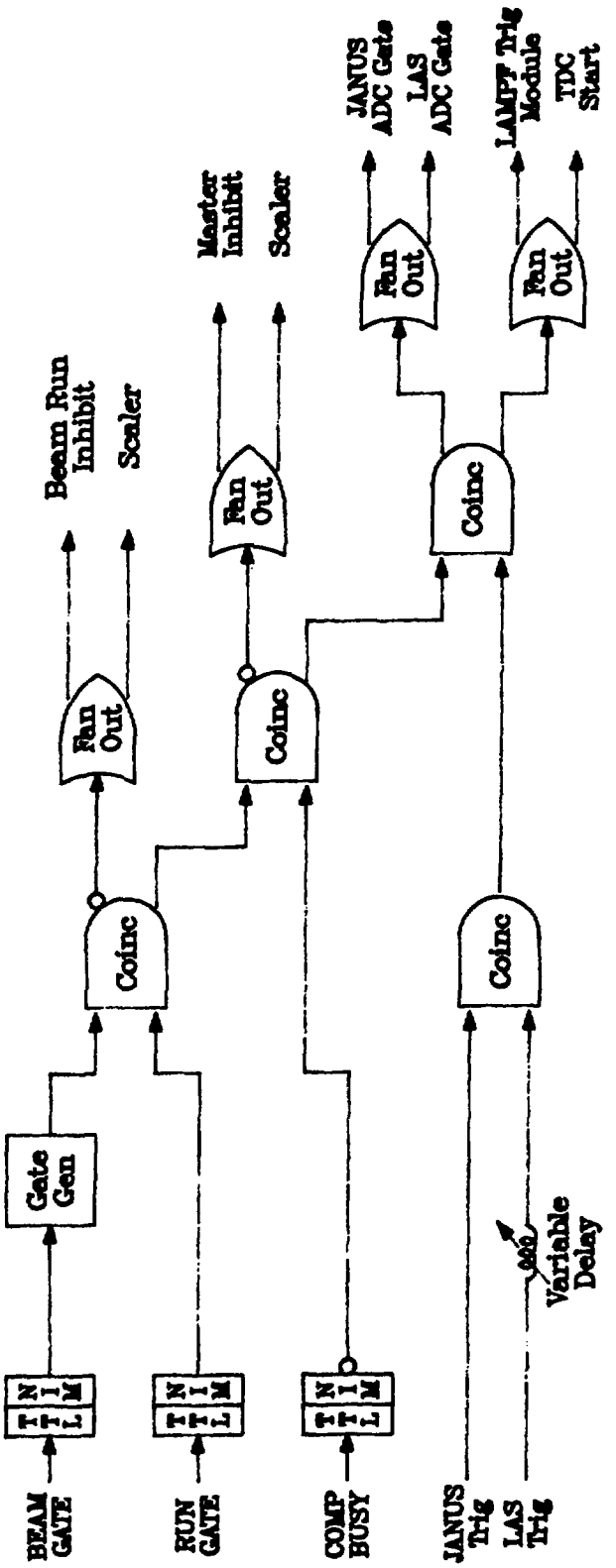

Figure 2-13

The Master Event Trigger Circuit

JANUS trigger signals described above, and a "computer busy" signal (which served as an inhibit).

The beam gate was a logic pulse received from the accelerator to signal that the beam was on. The run gate was a flip-flop signal produced by the LAMPF Gate Generator (LGG) that permitted computer control over starting and stopping data runs through CAMAC. Both of these signals were converted from a TTL to a NIM signal before further processing was done. A coincidence between these two signals and the LAS-JANUS coincidence signal was fed to the LAMPF Event Trigger Module.

The "computer busy" signal was also generated by the event trigger module by either the "Event 6" or "Event 7" signals. This signal was placed in anti-coincidence with the above three signals and served to inhibit the collection of data while the computer was busy with a previous event. Because the system was effectively "dead" during this time, this part of the circuit was also known as a dead time generator.

Besides providing the event trigger, the master trigger signal was used as the gate for all the LAS ADC's, as the start for the JANUS separate-gate ADC, and as the start pulse for all of the TDC's except those used for time-of-flight measurements.

CHAPTER 3

CALIBRATION

The off-line calibration and analysis was performed on a MicroVAX II and a VAX 8650, both manufactured by Digital Equipment Corporation. The replay version of the Q system, which does not contain the data acquisition part of the event analyzer, was used.

Section 1: Calibration of the LAS Spectrometer

The four sets of wire chambers in the LAS were multi-wire delay-line readout chambers. In the event analyzer, the position at which a particle passed through each plane in the chamber was determined using the following equation:

$$POS = (T2-T1)A + B \ . \qquad (3\text{-}1.1)$$

T1 is the time difference between the master trigger and the pulse from one end of the delay line (as determined by the TDC) and T2 is the time difference between the master trigger and the pulse at the other end of the delay line. (T2-T1) indicated where along the delay line the pulse originated and, therefore, which anode wire along the delay line fired. This anode wire was the nearest one to the

traversing particle. Since this was the only information obtained, the uncertainty of the position of the event was one full wire spacing (one-half wire-spacing on either side of the anode wire). The factor A in Eq. 3-1.1 set the scale of the histogram used to represent the wire chamber position; A was determined for each chamber plane so that 1 bin of the histogram corresponded to 1 mm. The factor B gave an overall offset to the plane position in the histogram. For the chambers with single-segment delay lines B was used to center the chamber planes in the software. For those planes that had more than one delay-line segment, the values of B were varied until the segments were joined together and the whole plane was centered (see Fig. 3-1).

Section 2: Calibration of the JANUS Polarimeter

As in the calibration procedure for the LAS, the calibration of the JANUS polarimeter is designed to ensure the proper determination of the position of a particle traversing a drift chamber plane and the proper centering of the chambers in the software. An overview of the procedure is given here with details following in subsections.

As in the LAS, the raw anode wire position in a plane is proportional to (T2-T1), where T1 and T2 are defined in

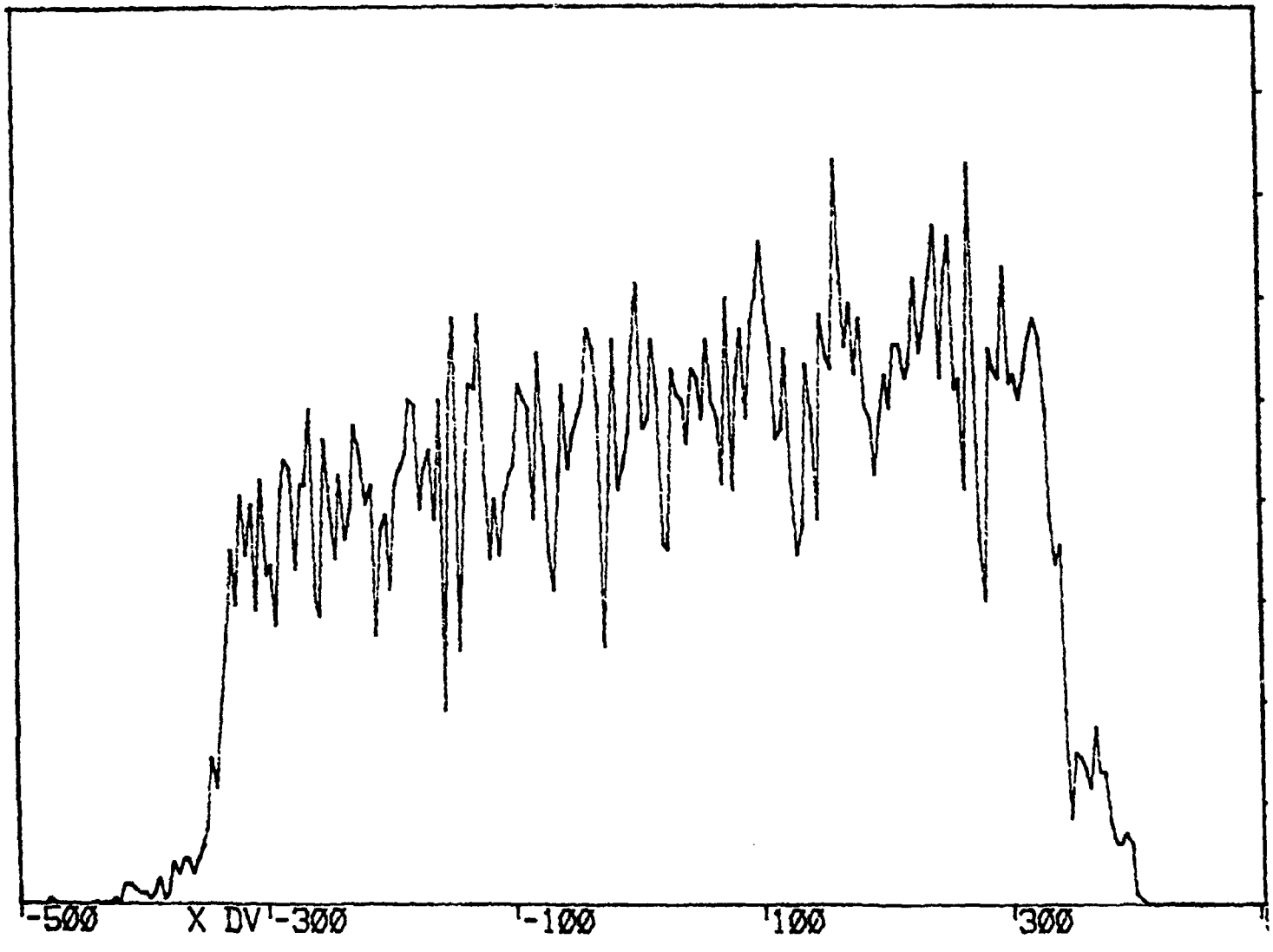

Figure 3-1

Example of an LAS Position Histogram

(Scale is 0.22 mm/channel)

a similar fashion to the quantities associated with the LAS chambers.

The JANUS drift chamber could now be used in the same way as the LAS spectrometer delay-line readout chambers, where the point of interaction is taken to be at the wire with an uncertainty of half the wire spacing on either side (in this case, 0.4064 cm). However, much finer position resolution was needed, due to the fact that very good angular resolution was necessary for properly analyzing events scattering in the carbon analyzer. The needed resolution was accomplished by determining the time it took for the ionized electrons produced by the traversing particle to drift to the anode wire (called the drift time, DTIM). The distance from the nearest anode wire, known as the drift position, DPOS, could then be determined from DTIM.

The value of DPOS does not contain any information about which side of the anode wire the traversing particle crossed; this uncertainty is known as the left-right ambiguity and was resolved in these drift chambers by looking at the pulse height of the (O-E) ADC signals produced on the odd and even cathode bus lines. The (O-E) signal determines on which side of the anode wire the particle traversed.

3.2.1 Calculation of the Anode Position

Fig. 3-2 shows a typical wire position spectrum for a drift chamber plane; all 73 wires (seen as peaks) can be clearly distinguished. During the calibration runs, enough data was collected so that each peak consisted of at least 10 events. The anode wire position (AP) was determined from the following formula:

$$AP = c_0 + c_1(AA) + c_2(AA)^2 , \qquad (3\text{-}2.1)$$

where AA is (T2-T1). If the chamber peaks were already centered in the histogram (i.e. the center wire was in the middle of the histogram) then c_0 would be set equal to zero. If the chamber was offset, the value of c_0 (in cm) was adjusted until the middle wire was centered. The constant c_1 set the scale of the histogram and, therefore, changed the peak spacing. It was a linear function of wire spacing, delay line speed, and TDC gain. In this experiment, the TDC gain was set at 0.5 ns per channel. As the signal goes through the delay line, it covers 1 cm of distance in the wire chamber every 2.5 ns;[28] by dividing the TDC gain by this effective speed a value of 0.2 cm per channel is obtained. However, these numbers assume that the calculations were done with respect to one of the ends of the wire chamber. Since all measurements were instead taken with respect to the center of the chamber, the value obtained from the calculation of $c_1(AA)$

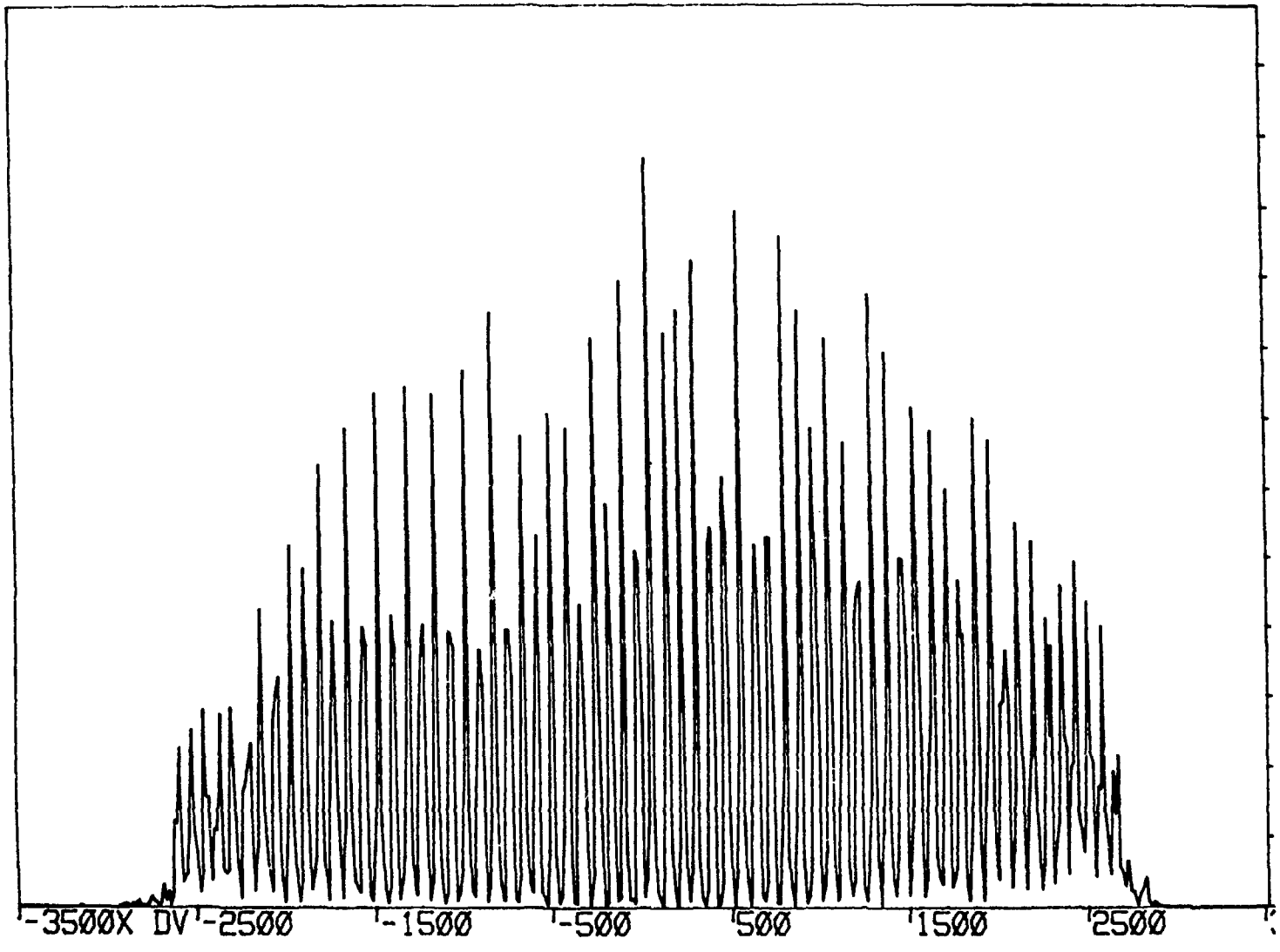

Figure 3-2

Example of a JANUS Anode Position Histogram

(Scale is 0.01 cm/channel)

produced a value twice as big as it should have been. Therefore, to obtain the correct result, the value of c_1 must be divided by two; c_1 was therefore initially set to 0.1 cm per channel. The constant c_2 adjusts for time walk at the ends of the delay line and was typically on the order of 10^{-4} to 10^{-5} cm per channel squared.[8]

Since JANUS consisted of twelve chamber planes (two planes in each chamber) there are 36 constants (12 c_0, 12 c_1, and 12 c_2) that were determined as follows. First, c_0 was determined for each chamber by calculating the offset necessary to center the central (37th) wire. After this was done, the spectra were fed through a fitting routine called EZCAL, which optimized c_1 and c_2.

For each spectrum, EZCAL determined the position of each peak by creating a window that was one wire spacing wide (and given in histogram channels). With the middle channel of the window set equal to zero, the channels on the left became negative and those on the right became positive. EZCAL calculated the number of events inside the window. If the number of events inside the window was below 10, the window was moved to the right. If the number of events was greater than 10, EZCAL calculated a correlation function:

$$\text{cor} = \sum \left[\begin{matrix}\text{number of events} \\ \text{in channel}\end{matrix}\right] \times \left[\begin{matrix}\text{channel} \\ \text{number}\end{matrix}\right]^2 \quad . \quad (3\text{-}2.2)$$

If the window was centered on a peak, this correlation function would be a minimum. EZCAL checked to see if the correlation function was decreasing as it moved the window; if it started to increase EZCAL stopped the window at the minimum and calculated the centroid of the peak:

$$\text{cen} = \frac{\text{cor}}{\sum \begin{matrix}\text{number of events} \\ \text{in channel}\end{matrix}} \quad . \qquad (3\text{-}2.3)$$

If the correlation function stayed above a the value 0.15, EZCAL would continue to move the window even though it found a minimum.

After finding the position of all the peaks in a spectrum, EZCAL calculated a truncated anode position, TAP, for each peak from the relations

$$\text{NAP} = \text{AP/WS} \quad , \qquad (3\text{-}2.4)$$

$$\text{TAP} = (\text{NAP})\text{WS} \quad , \qquad (3\text{-}2.5)$$

where WS is the spacing between anode wires (0.8128 cm). The calculation of NAP above was truncated to the nearest integer and therefore indicated the number of the wire which was hit. TAP is therefore the integer multiple of the wire spacing nearest to a particle traversing the plane. The values of TAP appear as a line on a plot of anode wire position versus anode wire number, while the values of AP appear as points scattered about the line (see Fig. 3-3). EZCAL performed a "reverse least-squares fit"

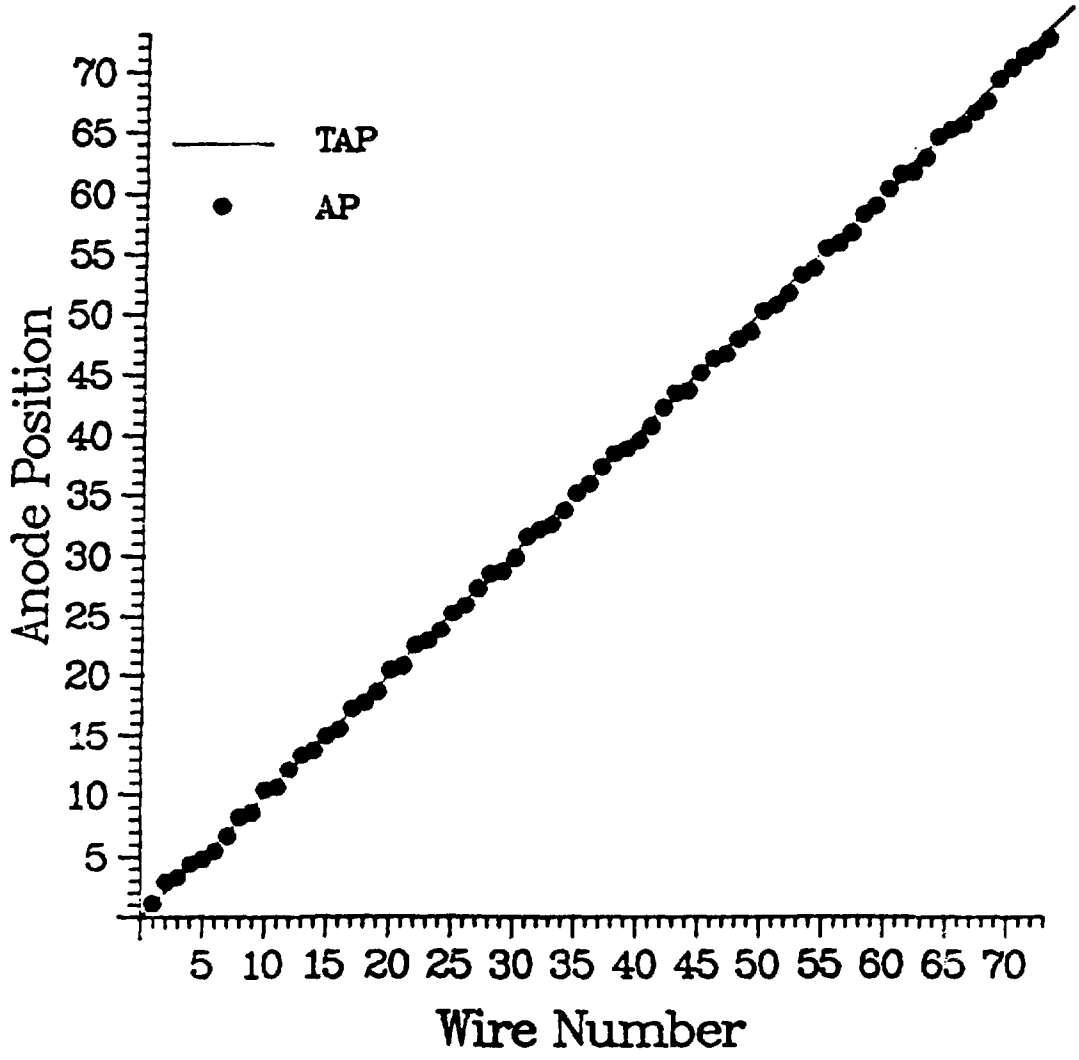

Figure 3-3

Plot of TAP and AP Versus Wire Number

in which the values of c_1 and c_2 (and, therefore, the values of AP) were varied until the sum of $(TAP-AP)^2$ was minimized (the values of c_1 were allowed to vary within a few percent of their nominal values).

3.2.2 Calculation of the Drift Position (DPOS)

T1 and T2 were added together in order to determine the drift time. The sum of these two signals contained the length (in time) of the delay line to which all the anode wires were attached plus twice the drift time. A determination of DTIM was therefore made by calculating:

$$DTIM = \tfrac{1}{2}(T2 + T1) - (\text{delay line length}) \quad . \quad (3\text{-}2.6)$$

An example of a drift-time histogram is shown in Fig. 3-4.

If the drift time were linearly related to distance from the wire, the spectrum would be rectangular (for uniform illumination over one wire spacing). Fig. 3-4 shows that, apart from a peak near the wire and a tail far from the wire, this is approximately true for the real spectrum. The peak near the wire results from an avalanche occurring at a small distance (approximately .1 mm) from the wire. Any time ions are created within some critical distance, a near-immediate avalanche will occur and all events will appear to have the same time. The tail results when a particle traverses the plane near the midpoint between two anode wires. The electric fields of the two

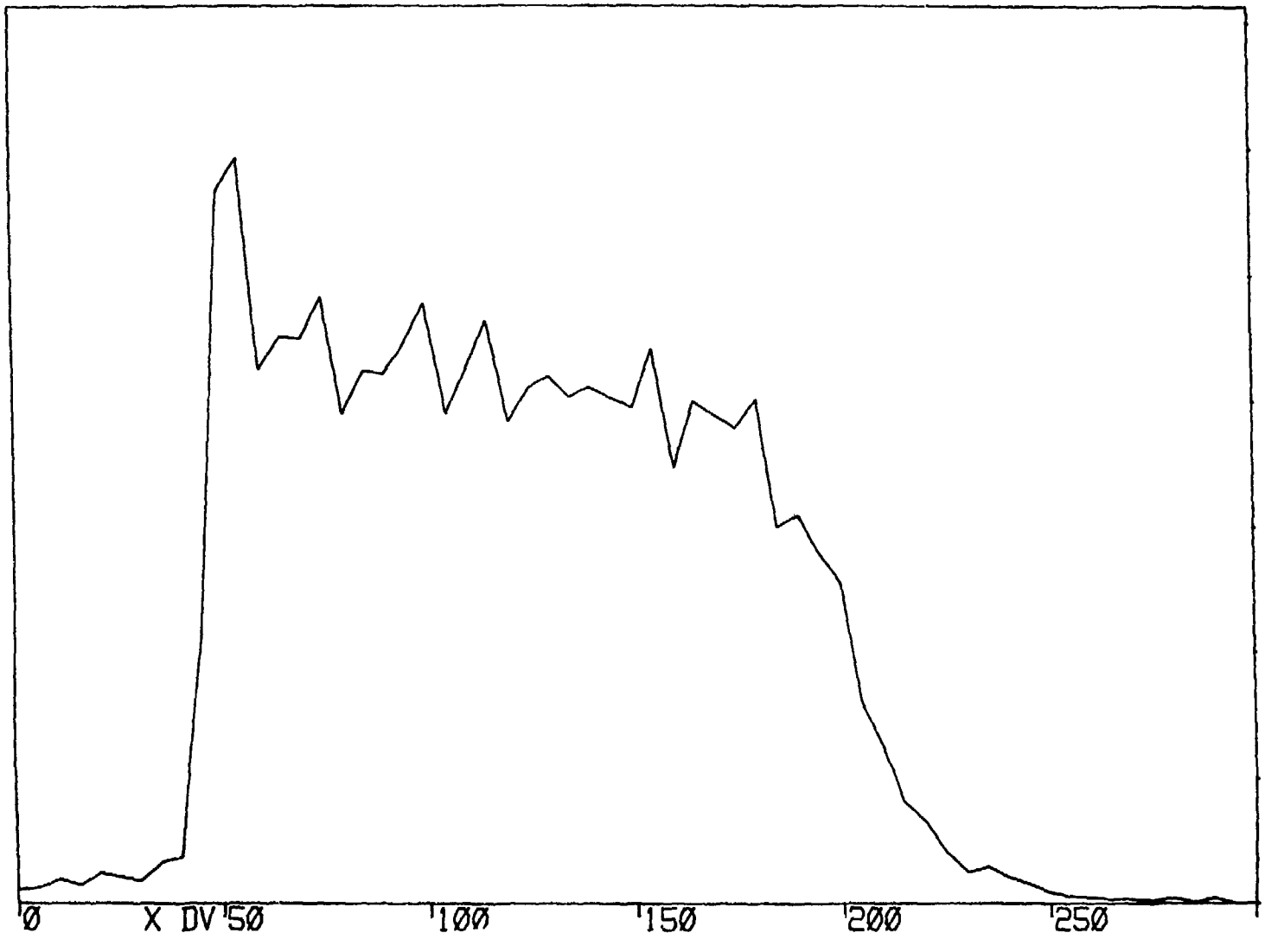

Figure 3-4

Example of a JANUS Drift Time Histogram

(Scale is 100 ps/channel)

wires combine to produce a weak field in which the electrons move more slowly at first. This slows down the time of arrival for them, resulting in a tail.

The drift-time information must then be transformed into drift-position information. The distribution of particles in time, dN/dt, is related to the distribution of particles in space, dN/ds, by[29]

$$\frac{dN}{dt} = \frac{dN}{ds}\frac{ds}{dt} = \frac{dN}{ds}\,v(t) \quad , \qquad (3\text{-}2.7)$$

where $ds/dt = v(t)$ is the drift velocity. If the distribution of events across one wire spacing were uniform, then dN/ds is constant, $dN/ds = c$, and

$$s(t) = \frac{1}{c}\int \left[\frac{dN}{dt}\right] dt \quad . \qquad (3\text{-}2.8)$$

The integral in Eq. 3-2.8 is simply the number of particles detected across one wire spacing during a certain time.

An offset was applied to each of the twelve DTIM histograms so that they all overlapped when superimposed (see Fig. 3-5). After the offsets were applied, all twelve histograms were added together and a table of s was made by integrating, as in Eq. 3-2.8. Examples of drift-position histograms made using the resulting table are shown in Fig. 3-6; they are relatively flat and can be seen to span one-half of the wire spacing (the histogram scale is 0.1 mm per bin).

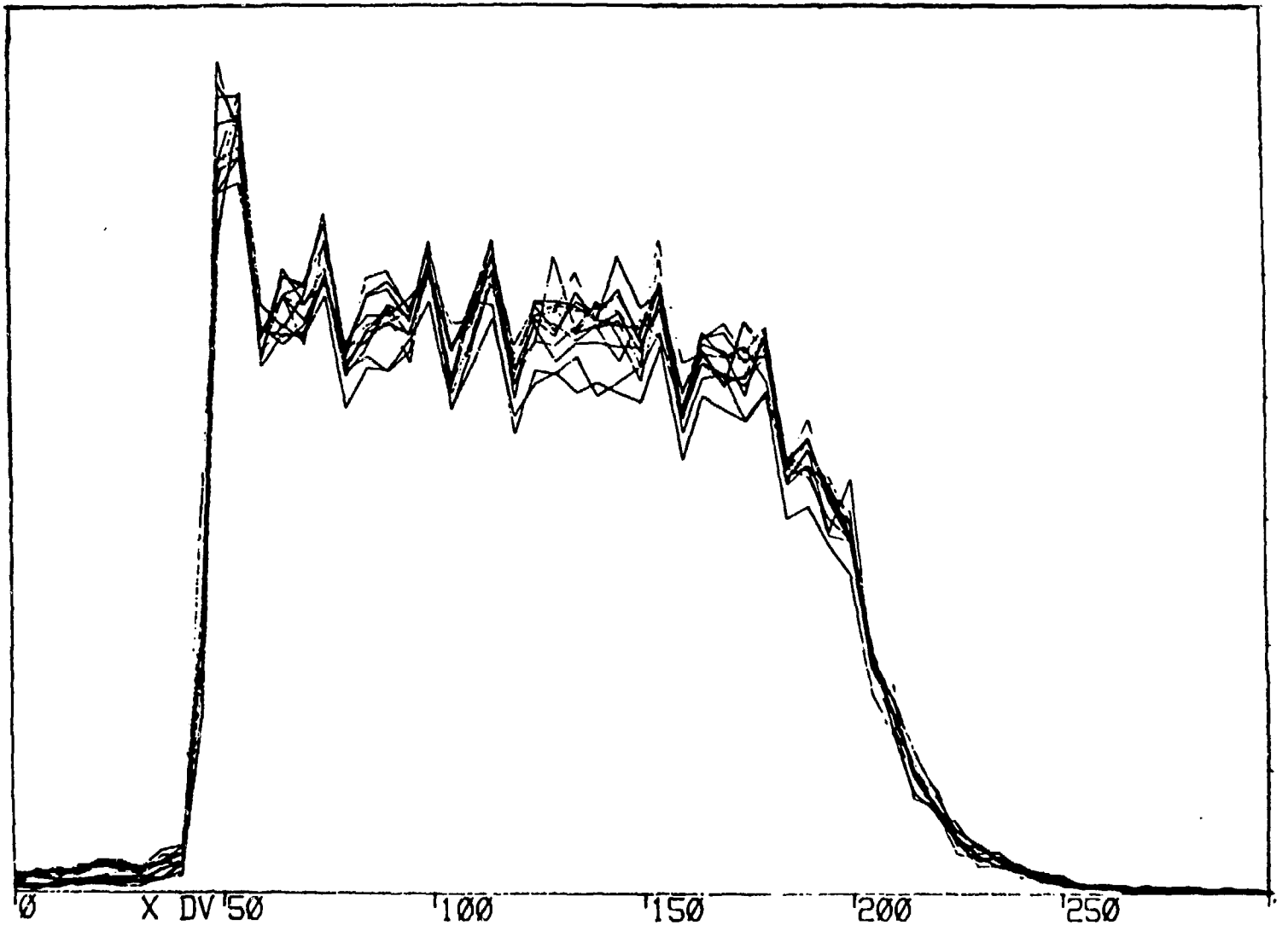

Figure 3-5

Overlay of all 12 Drift Time Spectra

(Scale is 100 ms/channel)

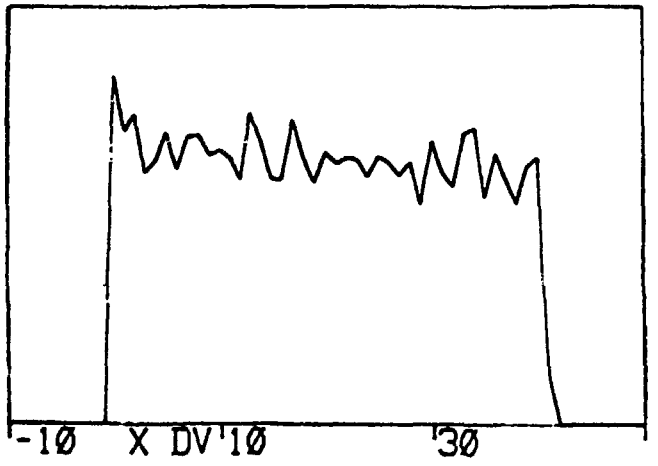

DPX1

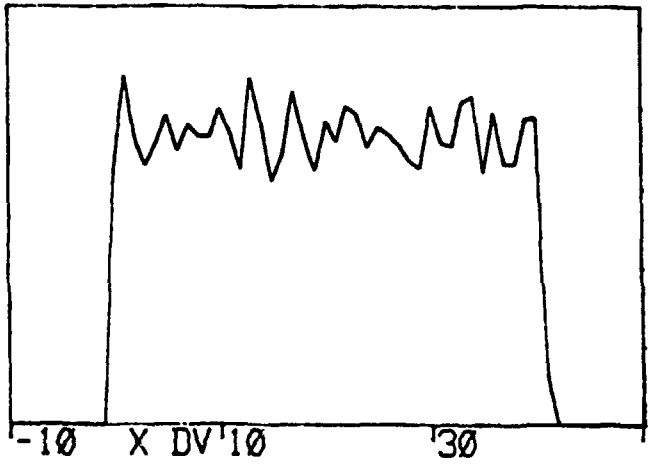

DPX6

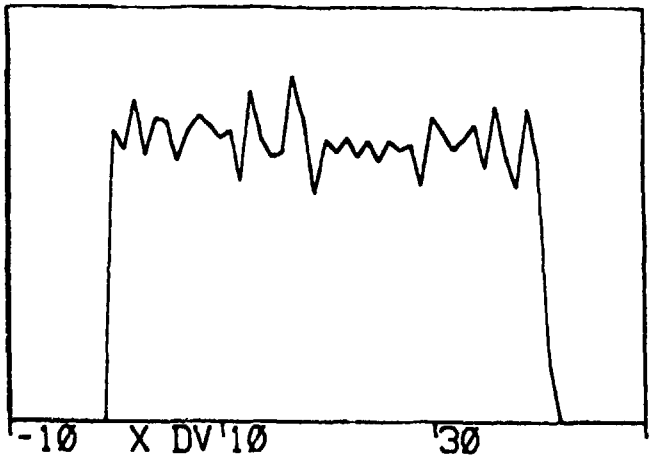

DPY1

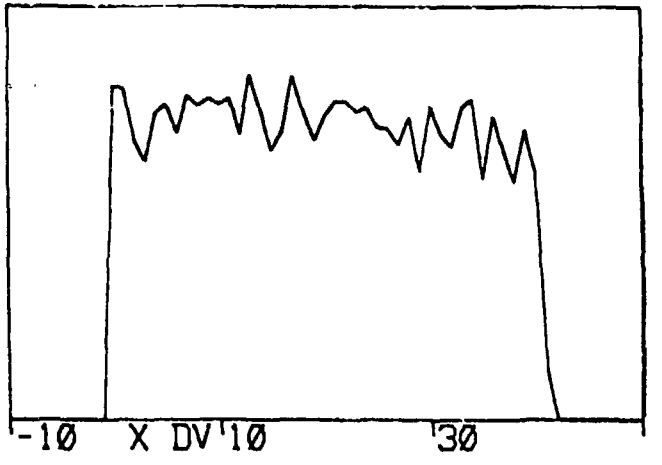

DPY6

Figure 3-6

Examples of Drift Position Histograms

(Scale is 0.1 mm/channel)

3.2.3 Resolving the Left-Right Ambiguity

The electron avalanche produced on an anode wire by a traversing particle induces pulses on the two neighboring cathode wires. The pulse height on the cathode wire which is on the same side as the traversing particle is 20-30% larger than the pulse on the opposite cathode wire.[30] By subtracting the two pulse heights, a determination can be made of which side the particle passed through.

As stated earlier, the O-E pulse from each chamber plane is fed into a separate-gate ADC. The ADC can only accept negative pulses. However, since the signal from the odd bus line can be larger than that from the even bus line, the O-E signal can be positive. The O-E amplifiers must therefore be adjusted so that all signals reaching the ADC are negative (see Fig. 3-7).

Two different modes of this signal are possible: 1) a high-gain mode that is dominant when the wire chamber is run at 2200 volts, and 2) a low-gain mode that is dominant at 2000 volts. The low-gain signal is due to the fact that the amplification due to avalanching is not large at 2000 volts. Since the chambers were run close to 2200 volts to maximize their efficiency, the high-gain mode dominated with a small admixture of low-gain signal.

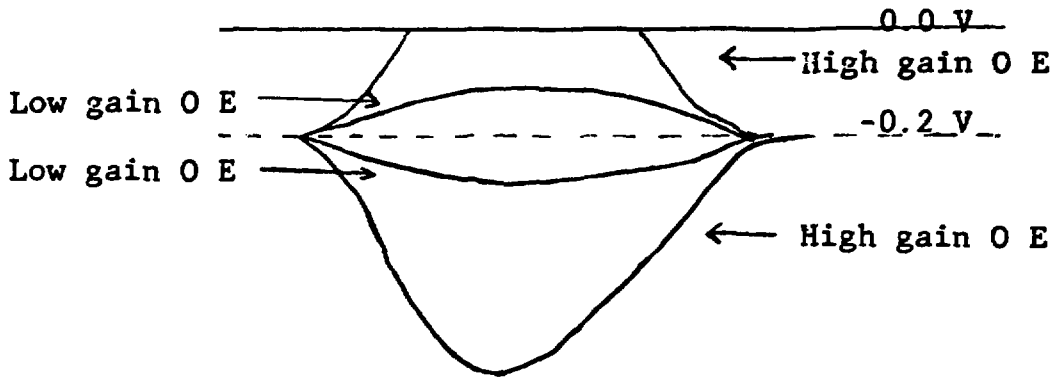

Figure 3-7

The Odd Minus Even Signal

A histogram of an ADC spectrum is shown in Fig. 3-8. A sharp peak can be seen at the lower end of the spectrum. This peak corresponds to the O > E high-gain signal and results from the fact that this signal saturates (as shown in Fig. 3-7) and not much current is integrated by the ADC. The peak at the higher end of the spectrum corresponds to the O < E high-gain signal and is broad because the current is integrated over a much larger range than that for the O > E signal.

A smaller peak which is equidistant from the other two is also seen in Fig. 3-8. This peak corresponds to the low gain signal. The O > E signal is contained in the left half of this peak, while the O < E signal is contained in the right half of this peak.

A software offset is used to shift the O > E high-gain peak and the O > E half of the low-gain peak so it has a different sign from the O < E peak. The offset is chosen by visually determining the halfway point of the low-gain peak and shifting the halfway point to 0.0 in the histogram spectra.

In the following discussion, the assumption is made that O > E. As can be seen from Fig. 2-7, if a particle passed close to any odd-numbered anode wire, the particle traversed the right side of the anode wire. However, if the particle passed near any even-numbered anode wire, the

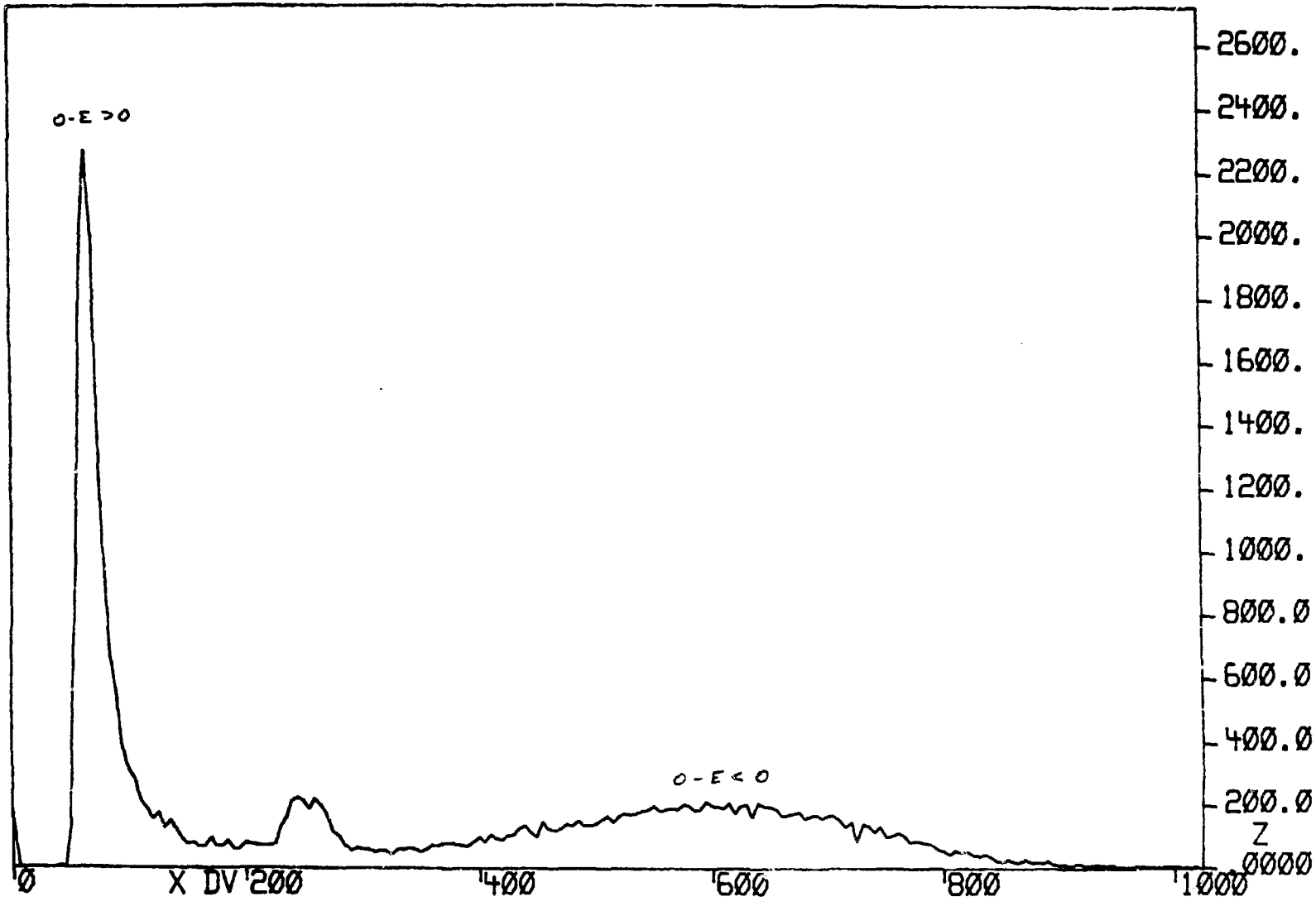

Figure 3-8

Example of a JANUS ADC Spectrum

particle traversed the left side. An equivalent situation holds when O < E. By using a factor $(-1)^{NAP}$ in the calculation of position, however, a consistent determination can be obtained for all wires:
(O > E) & $(-1)^{NAP}$ < 0 –> particle traversed to the right,
(O > E) & $(-1)^{NAP}$ > 0 –> particle traversed to the left.

3.2.4 Final Determination of Position

After TAP, DPOS, and the O-E sign have been determined, the position is obtained from the formula:

$$POS = TAP + (-1)^{NAP} \times sign(O-E) \times DPOS - C \ , \quad (3\text{-}2.9)$$

where sign(O-E) stands for the sign of the O-E signal and C is a constant used to adjust for the alignment of the chambers. C will be explained in a later section.

Section 3: Checks on the Calibration

A number of checks were performed to determine if the chambers were determining particle hit positions correctly.

3.3.1 Sign of the O-E Signal

Alternate cathode wires were bussed together; one set was referred to as "even" and one set was referred to as "odd". The ordering of the two sets (i.e. whether the first cathode wire was designated even or odd) affected the sign of the O-E signal. For example, if the first cathode wire on the left of the plane were designated even, then,

for the first anode wire (see Fig. 3-9a):

$$0 > E \;\&\; (-1)^1 < 0$$

$$\rightarrow \text{ particle traversed to the right.}$$

If the first cathode wire were designated odd, then (see Fig. 3-9b)

$$0 > E \;\&\; (-1)^1 < 0$$

$$\rightarrow \text{ particle traversed to the left.}$$

The ordering of the odd-even bus lines is known as the phase of the plane.

In order to obtain correct track information, the phase of all six x-planes had to be the same and the phase of all six y-planes had to be the same. The following procedure was used to make sure that this was the case.

For both the x-planes and the y-planes, a dot plot of the calculated position in the x-plane (y-plane) of one chamber versus the final position in the x-plane (y-plane) in an adjacent chamber was made (see Figs. 3-10). In such a dot plot, one of three conditions existed: 1) both chambers had the correct phase, 2) one chamber had the correct phase while the other chamber had the incorrect phase, or 3) both chambers had the incorrect phase.

1) If both chambers had the correct phase, the dot plot showed a sharp, straight line, as in Fig. 3-10a.

2) If one chamber had the correct phase while the other chamber had the incorrect phase, then

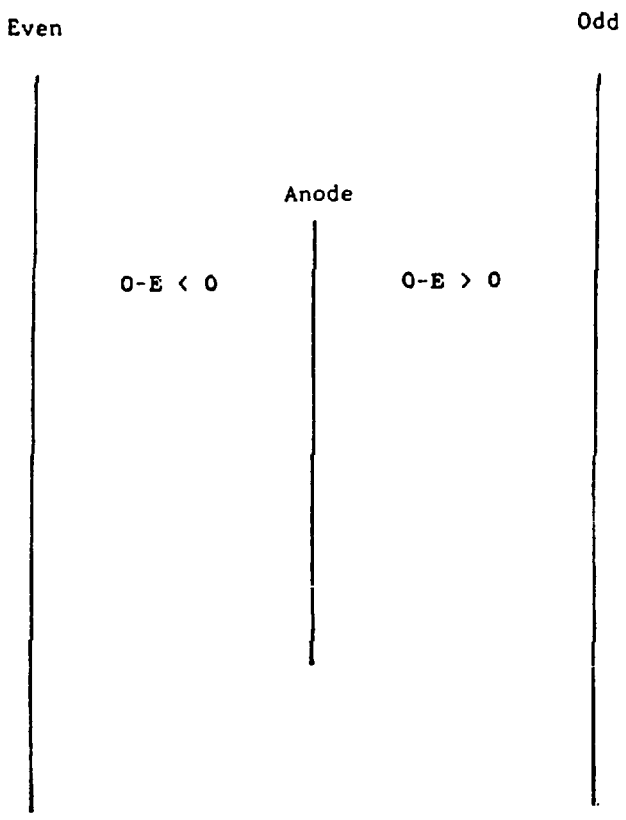

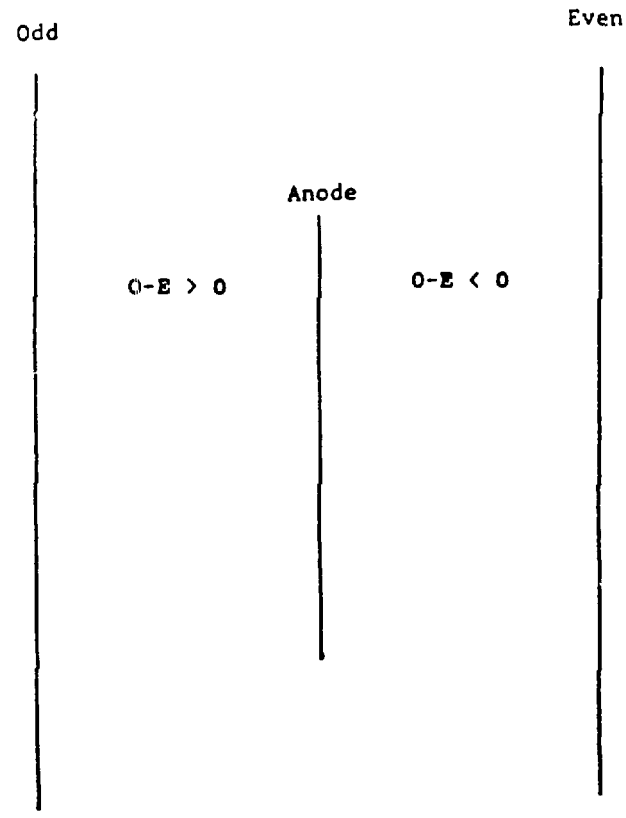

Figure 3-9

Phase of the Odd-Even Cathode Lines

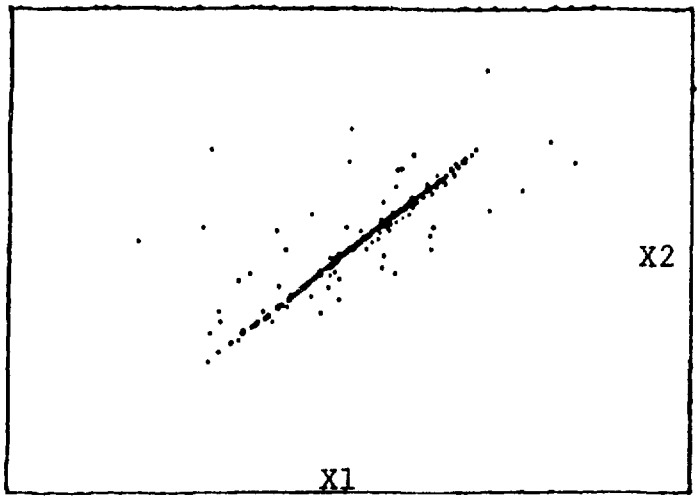

Proper Phase For Both Planes

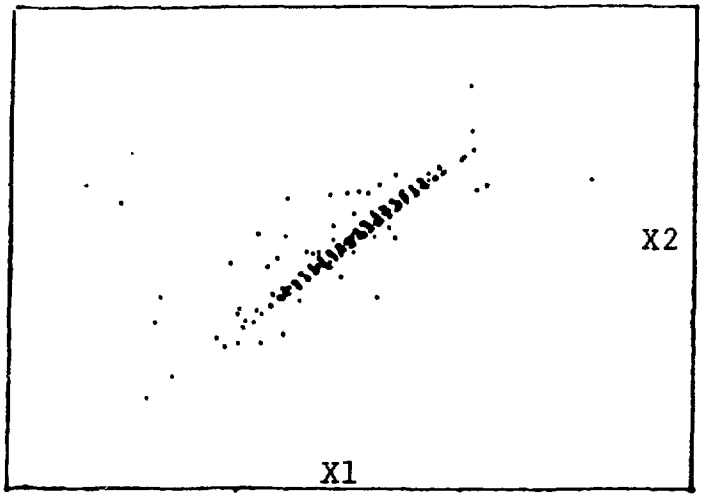

Incorrect Phase For One Plane

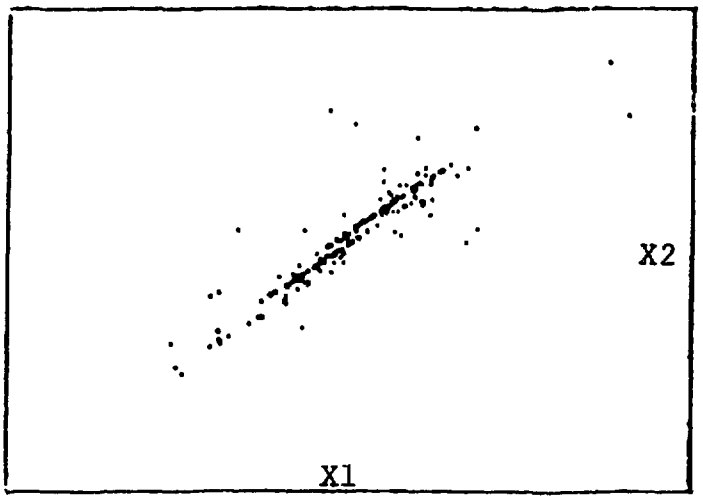

Incorrect Phase For Both Planes

Figures 3-10

Examples of Phase Dot-Plots:

the dot plot had the cross-hatched pattern shown in Fig. 3-10b. This is due to the fact that, as one position increases, the other decreases, with both giving the same value at each anode wire. Each short line segment therefore corresponds to one anode wire.

3) If all particles that were going through the chambers were parallel and if all the planes were perfectly aligned, it would not be possible to tell if both chambers had incorrect phases. In fact, the particles were diverging and the planes were not perfectly aligned, with the result that the dot plot contains a series of parallel lines (Fig. 3-10c).

If it was determined that a chamber was out of phase, a correction was applied to the offset c_0 in the calculation of AP (Eq. 3-2.1) that consisted of the addition or subtraction of one wire spacing; this shifted the wire number by one and also the ordering of the odd and even bus lines.

3.3.2 Physical Alignment

The physical alignment of the chambers was checked by calculating a quantity known as the residual. The x-planes in the front three chambers are used as an example for the following discussion.

The average position in the three chambers was calculated as

$$\frac{X(1) + X(2) + X(3)}{3} ,$$

where X(1) is the hit position in chamber 1, X(2) is the hit position in chamber 2, and X(3) is the hit position in chamber 3. The residual was simply the difference between this point and the actual hit position in chamber 2. A similar residual was calculated for the front y-planes and the back x-planes and y-planes; examples are shown in Figs. 3-11. If these chambers were aligned, the residual should consist of a sharp peak centered about zero. If the peak was not centered, the constant, C, in Eq. (3-2.9) was adjusted for the middle plane of each set to achieve this. A similar procedure was followed for all four sets.

After the above corrections were made, a check of the alignment of the back chambers with respect to the front ones was made by calculating a series of "front-back" residuals. For this procedure a series of calibration runs were performed in which the carbon analyzer was taken out. As an example of how the front-back residuals were calculated, the x-planes are used.

A line drawn through the hit positions in the front three chamber planes was extrapolated to pass through the

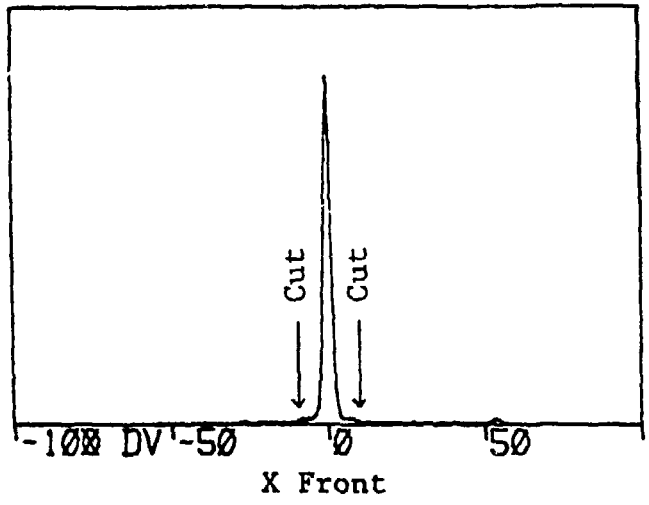

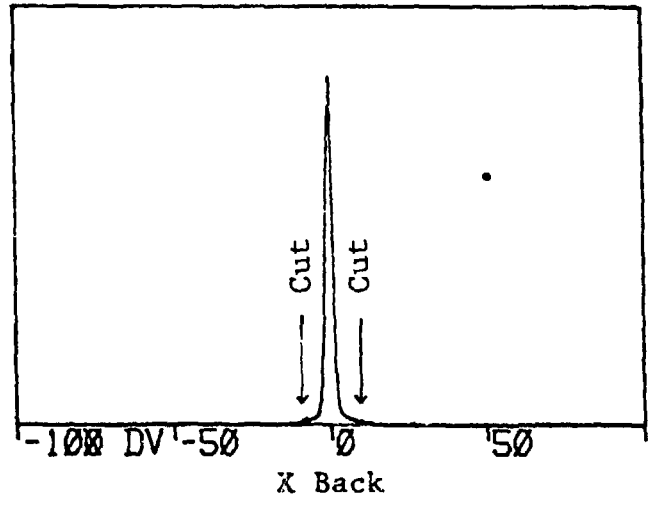

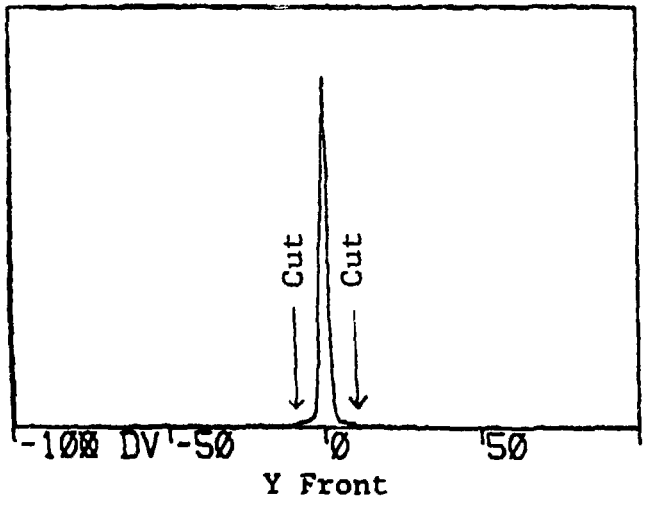

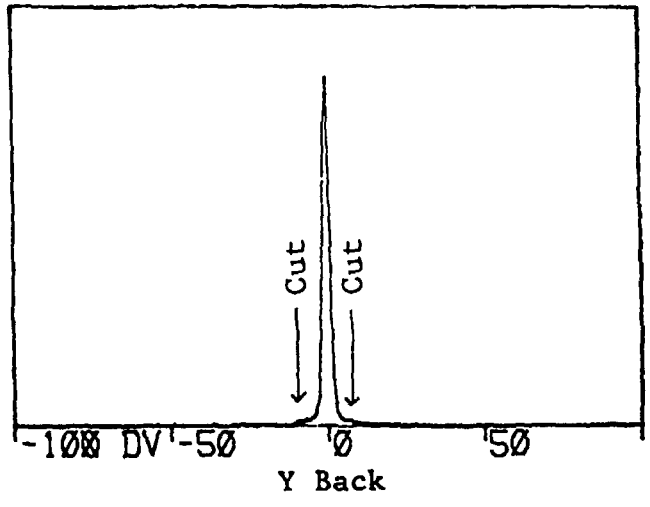

Figure 3-11

Example of Residual Histograms

(Scale is 0.01 cm/channel)

back three chamber planes. The front-back residual for X4 was then the difference between the point where the line intersected the X4 plane and the actual hit position in X4. Front-back residuals for X5 and X6 were calculated in a similar fashion. Similar front-back residuals were calculated for Y4, Y5, and Y6. Examples of the front-back residuals are shown in Figs. 3-12.

3.3.3 Left-Right Determination

The left-right determination was checked by the software for each event. Again, the front x-planes will serve as an example. The event position was switched from one side of the anode wire to the other side for one chamber plane at a time and the residual was recalculated; only one plane at a time out of the three was allowed to have a position opposite to the original. The combination which gave the smallest residual was used. A similar procedure was used for the other three sets of planes (X4-X5-X6, Y1-Y2-Y3, and Y4-Y5-Y6).

3.3.4 The Distance of Closest Approach, DCLOSE

Once the calibration of the polarimeter had been performed using the above procedures, carbon was inserted between chambers 3 and 4 and data acquisition was begun. The calibration was monitored by looking at the distance of closest approach (DCLOSE) between the initial track of the particle calculated from the position information provided

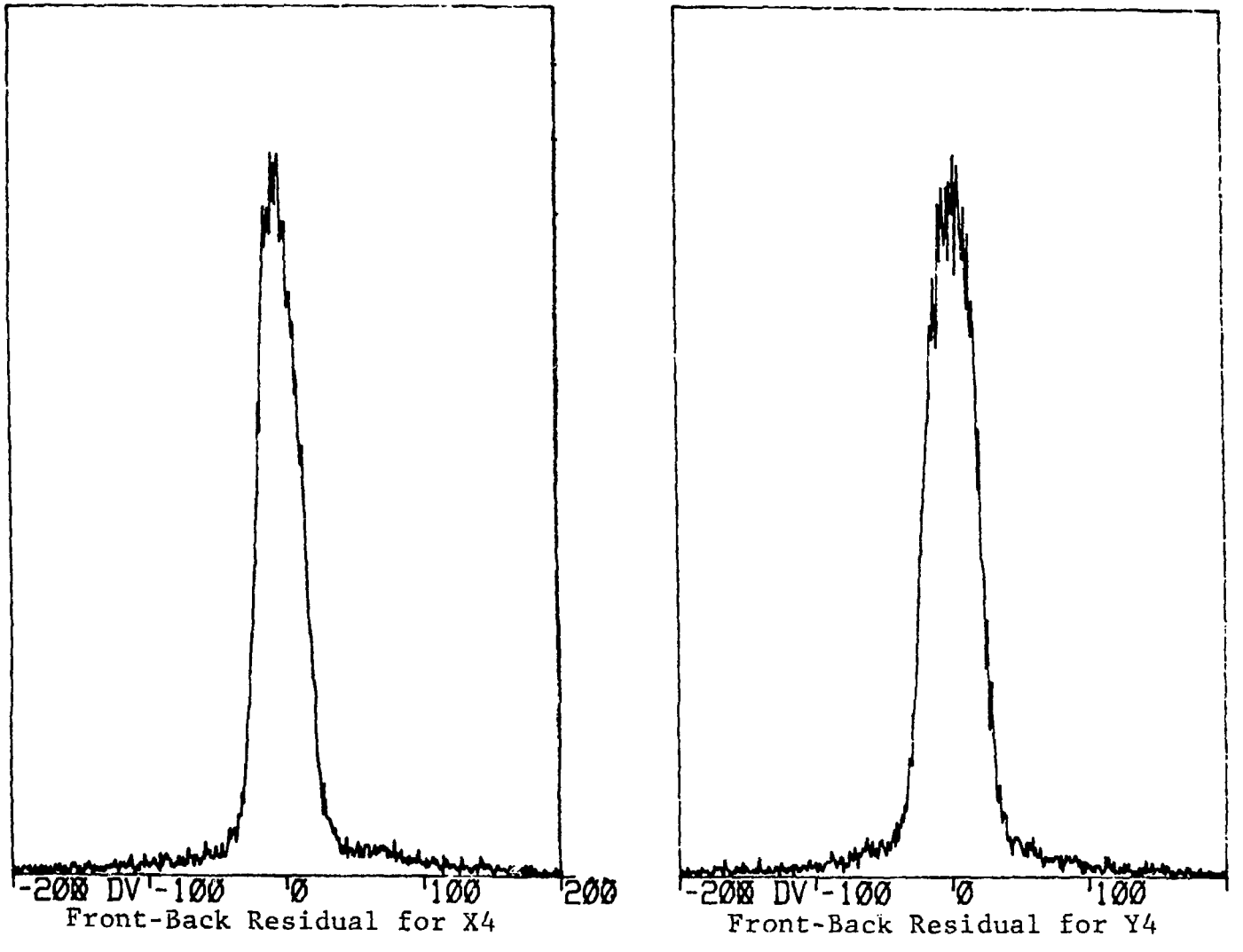

Figure 3-12

Examples of Front-Back Residual Histograms

(Scale is 0.01 cm/channel)

by the chambers in front of the carbon and the final track of the particle calculated from the position information provided by the three chambers behind the carbon (see Fig. 3-13). A spectrum peaked at zero indicated that the calibration was still good. One not peaked at zero indicated that the data acquisition had to be stopped and the polarimeter recalibrated. The initial calibration that done at the beginning of the experiment remained good throughout the data acquisition.

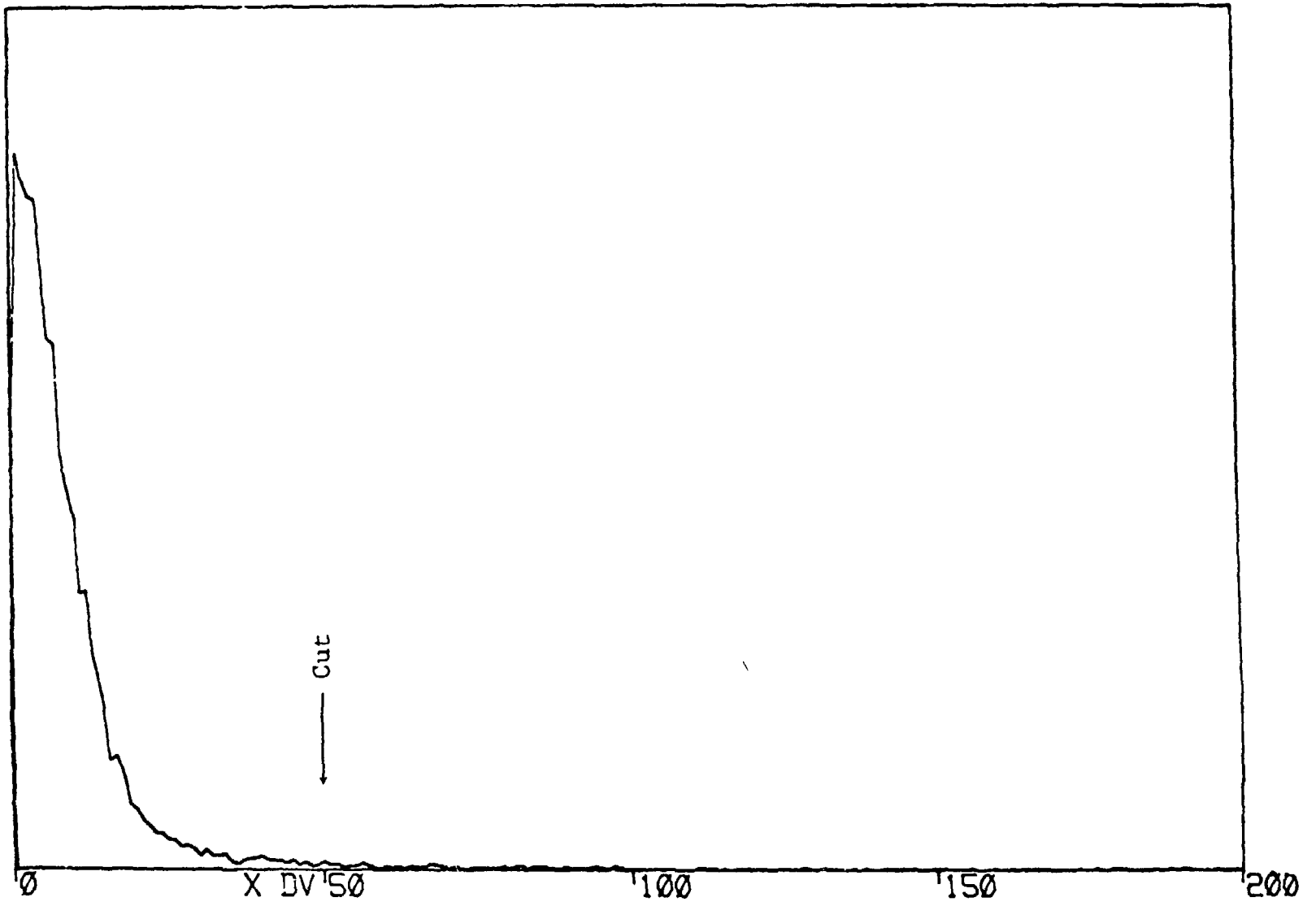

Figure 3-13

Example of Distance of Closest Approach Histogram

(Scale is 0.01 cm/channel)

CHAPTER 4

ANALYSIS

Section 1: Data Reduction

In order to determine the recoil proton polarization, the scattering events recorded on tape had to be analyzed to separate good events from the background. This separation took the form of a series of tests imposed on each event; events which passed all of the tests were considered valid.

4.1.1 Checksum

As discussed in Sec. 3.2.2, the sum T1+T2 represented the length of the delay line (a constant factor) plus twice the drift time. The time difference between the arrival of the master trigger signal and the O+E signal also contained the drift time plus a constant factor. The checksum was defined as

$$CKSM = T1 + T2 - 2T_{OE}$$

and was, therefore, constant. This provided a check on the chamber calibrations and a way to exclude possible background events.

An example of the checksum is shown in Fig. 4-1. It shows a sharp peak (corresponding to a constant value) and some background. Software cuts were placed around the peak to cut out the background.

Since wire chambers are not 100 percent efficient, some events passing through it were not detected. These events, which were counted by the master trigger, were thrown out by the checksum of that chamber. A comparison of the master trigger events with the events thrown out by the checksum, therefore, provided a measure of the inefficiency of the chamber.

Since only two chamber planes in the front and two chamber planes in the back are necessary for track identification in either the x or y direction, an event was only required to pass two out of three checksums for each of the four sets of chamber planes (the front x, front y, back x, and back y). This increased the overall number of good events by approximately one third. As explained in Sec. 4.1.5, at least one of the four sets had to have three good checksums.

For the back y set of planes, there was another reason for requiring only two out of three good checksums. During the experiment, it was discovered that two wires in chamber plane Y5 had broken their connection to the delay line and were not responding (see Fig. 4-2). If three good checksums were required for this set, particles passing

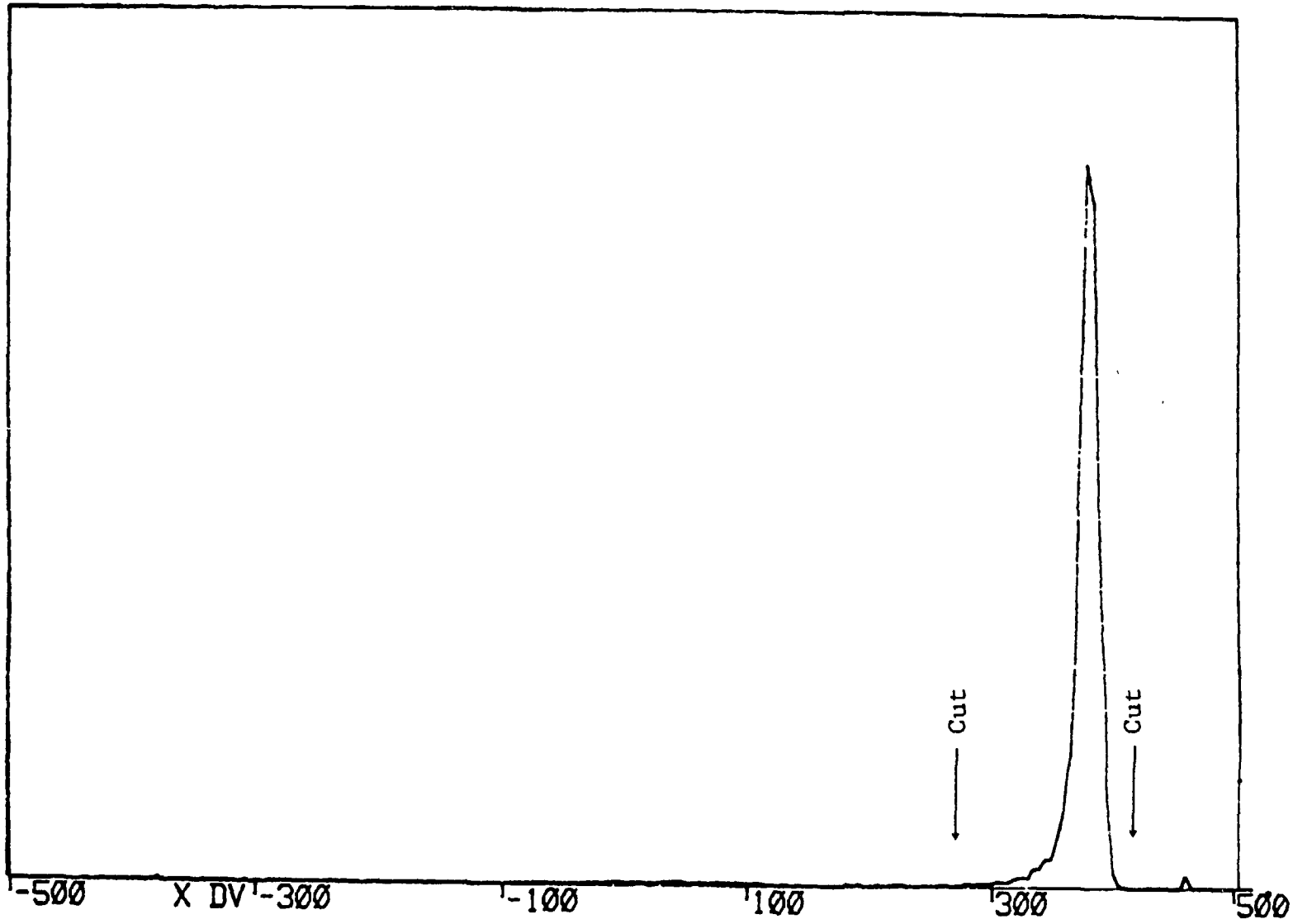

Figure 4-1

Example of a JANUS Checksum Histogram

(Scale is 100 ps/channel)

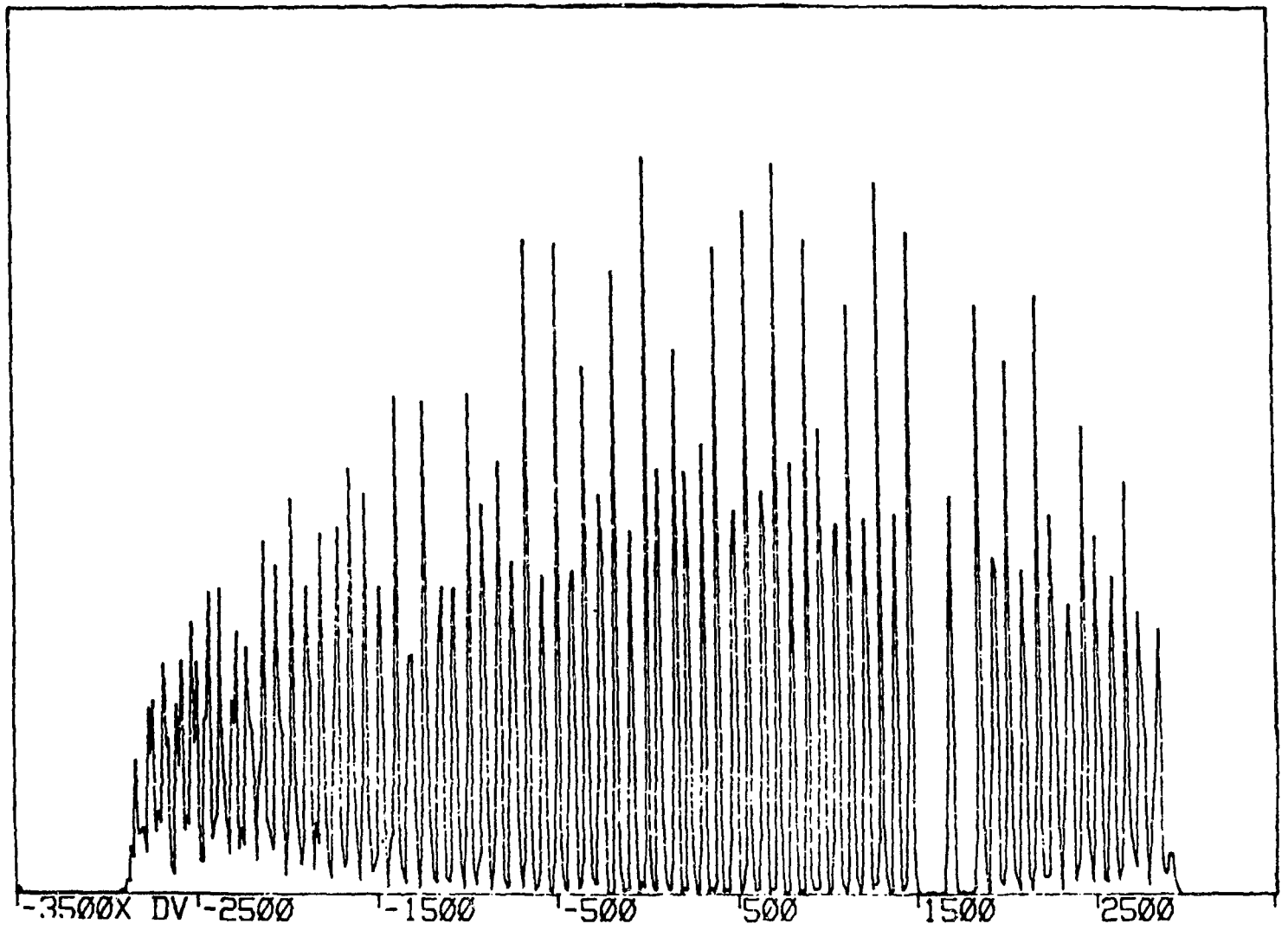

Figure 4-2

Y5 AP histogram Showing Missing Wires

(Scale is 0.01 cm/channel)

through Y6 near those two wires would be thrown out, resulting in a large systematic uncertainty. By requiring only two out of three good checksums, however, these events were recovered and the problem was resolved.

A checksum for the LAS wire chambers was defined as the sum T1+T2. An example of an LAS checksum is shown in Fig. 4-3. Since this quantity contains drift-time information that cannot be extracted for these chambers, T1+T2 had some variation and, therefore, no software cut was placed on them. They did, however, provide some check that the chambers were operating properly and did provide inefficiency information.

4.1.2 Distance of Closest Approach

As discussed in Sec. 3.4.4, the distance of closest approach between a proton track into the carbon and one out of the carbon was calculated from the chamber position information.

The location of the midpoint of the line connecting the two tracks was also calculated. Histograms for the x- and y-coordinates for this point are shown in Fig. 4-4 and show sharply defined peaks well within the acceptance of the spectrometer. A histogram for the z-coordinate is shown in Fig. 4-5. The peak is not as well defined as those for the other two coordinates since it is badly

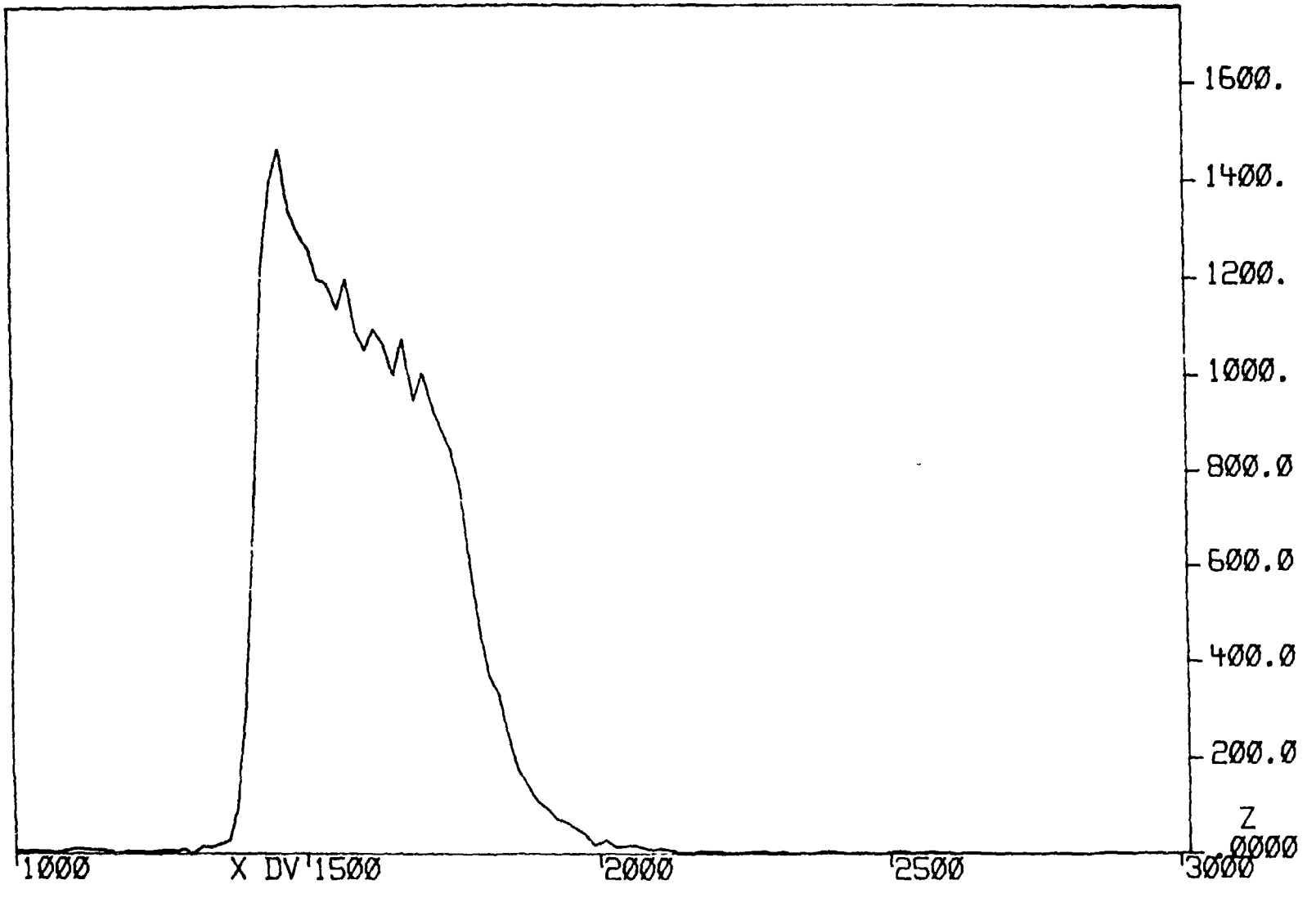

Figure 4-3

Example of an LAS Checksum Histogram

(Scale is 100 ps/channel)

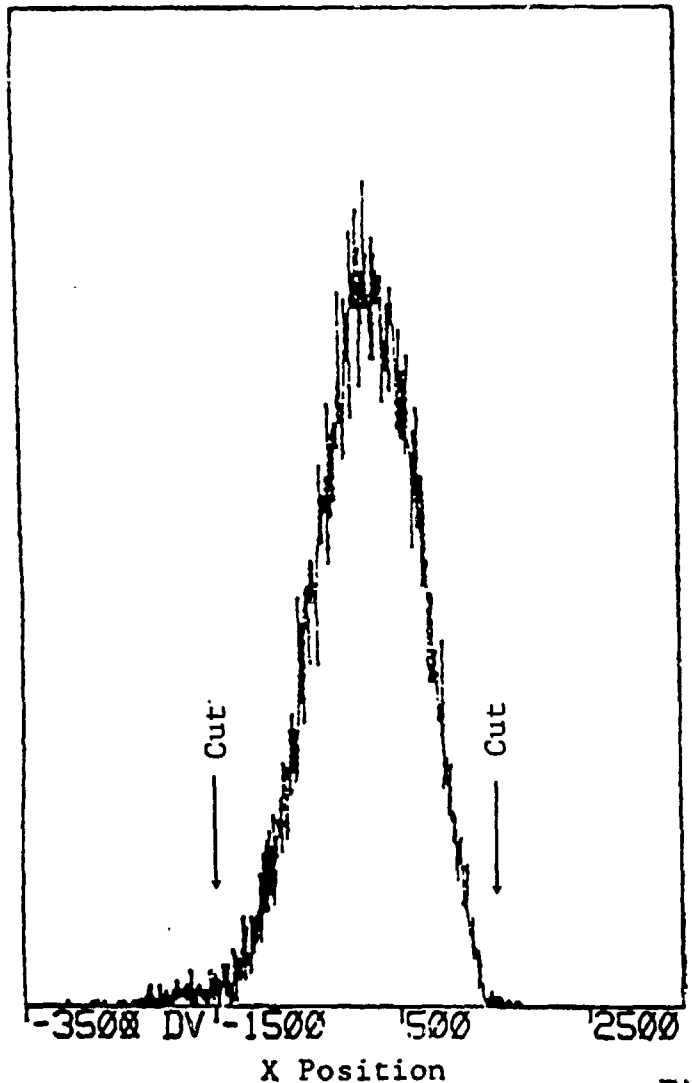

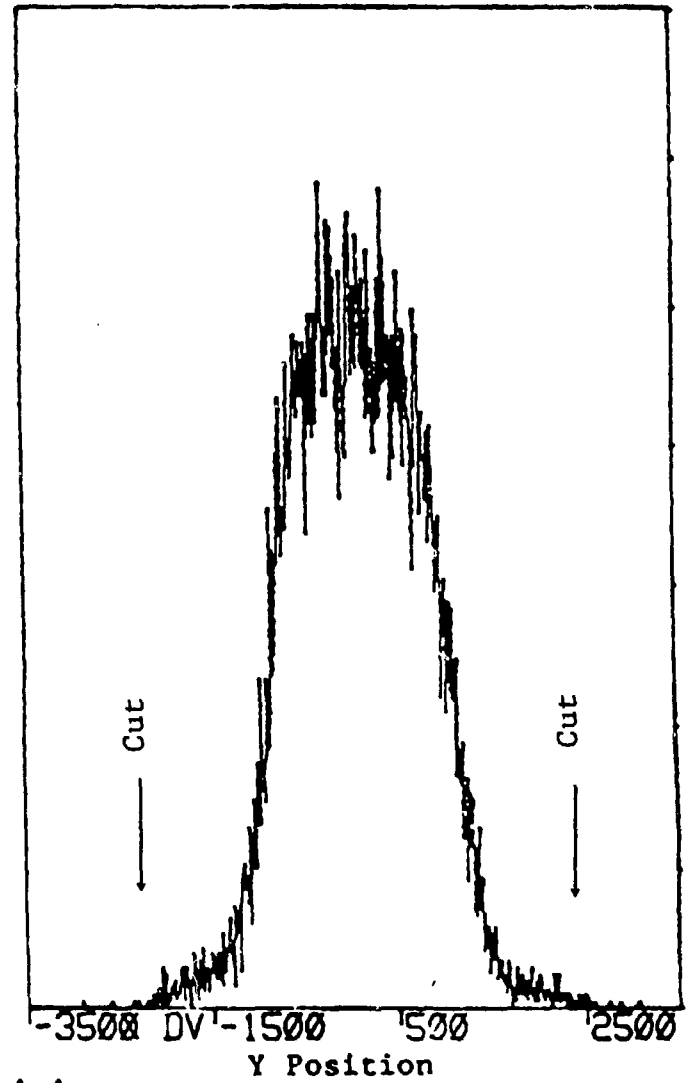

Figures 4-4

Example of Histograms for:

a) the X-Coordinate, and b) the Y-Coordinate,

of the Midpoint of DCLOSE

(Scale is 0.01 cm/channel)

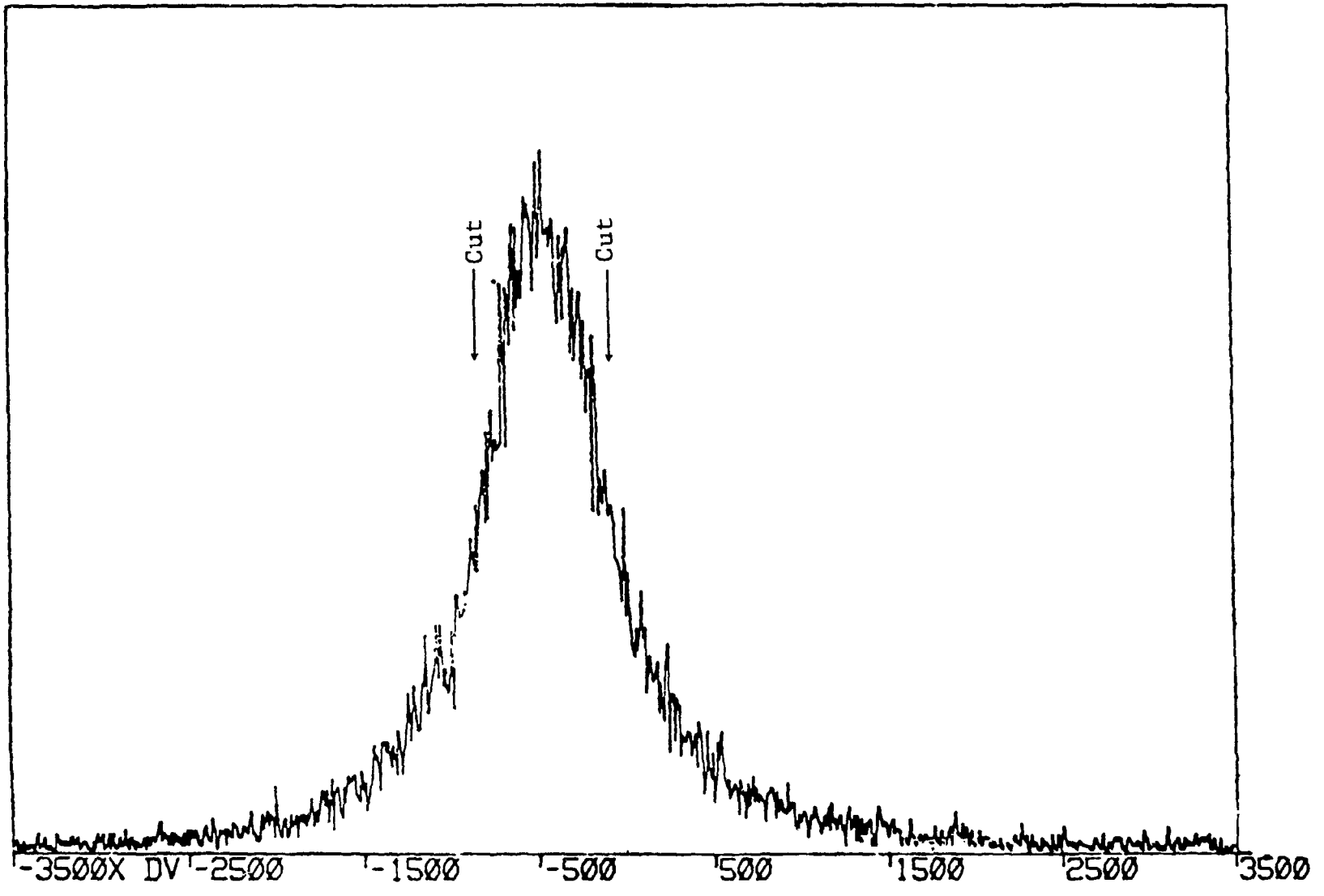

Figure 4-5

Example of the Z-Coordinate for the Midpoint of DCLOSE

(Scale is 0.01 cm/channel)

determined for small scattering angles. Cuts were placed around the peak to ensure that only events scattering within the carbon would be allowed.

A histogram of DCLOSE is shown in Fig. 3-13. A cut of 5 mm was used (this corresponds to the convention used by LAMPF, TRIUMF (in Canada), and SIN (in Switzerland).

4.1.3 Polar Scattering Angle

Fig. 4-6 is a histogram of the sine of the polar scattering angle in the carbon. The distribution is sharply peaked at small angles. This peak contains events scattered by the Coulomb interaction.

Multiple scattering of the proton in the carbon analyzer has no dependence on the spin of a particle.[21] This interaction therefore produces no asymmetries, and the analyzing power of the carbon for a proton scattered this way is therefore zero. These events drastically lower the observed analyzing power of carbon and drastically increase the systematic uncertainties associated with the recoil polarizations. To avoid such large uncertainties, a cut was placed on $\sin\theta_C$ to reject these events. The effect of the placement of this cut at various values of $\sin\theta_C$ for 625 MeV/c π^+ is shown in Table 4-1. For each momenta, cuts were placed at the point where the analyzing power dropped below 0.4. As a result, 95 to 98 percent of the recorded events were rejected.

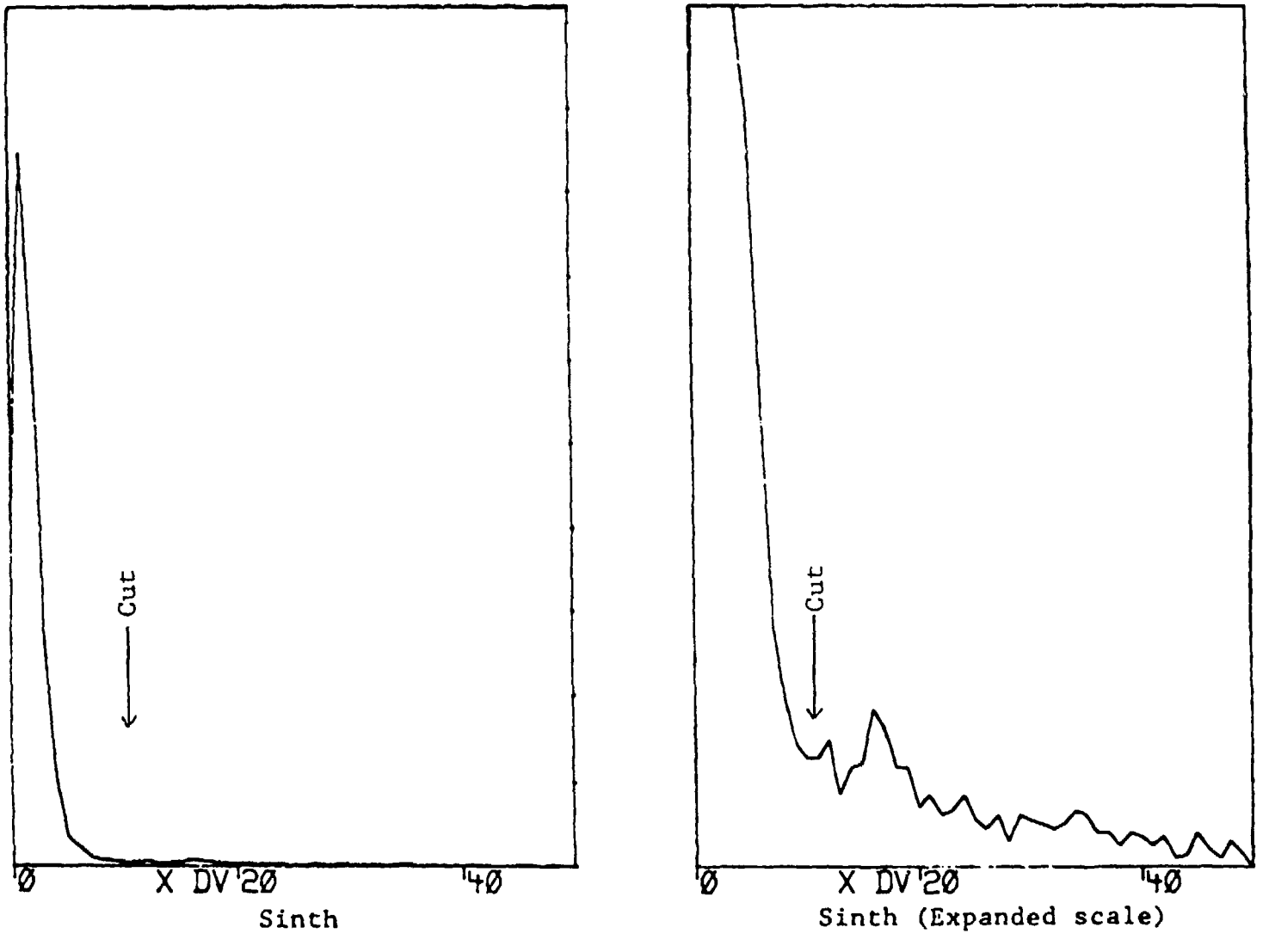

Figure 4-6

Example of the $\sin\theta_c$ Histogram

(Scale is ×100)

TABLE 4-1

ANALYZING POWER OF CARBON VERSUS ANGLE

FOR 625 MeV/c π^+

θ_C (deg)	$\sin\theta_C$	A_C
3.13	.06	.21
3.68	.06	.25
4.29	.08	.29
5.19	.09	.35
CUT		
6.32	.11	.43
7.45	.13	.50
8.63	.15	.57
9.81	.17	.61
11.25	.20	.64
13.26	.23	.60
15.84	.27	.50
CUT		
18.35	.31	.38

The thickness of the carbon analyzer was adjusted to minimize the multiple scattering angle while still allowing for a large number of nuclear scatters. The thickness used throughout this experiment was 6.3 cm.

4.1.4 Symmetry Test

In order to extract the recoil polarization by the method explained in Sec. 4.2.2, it was necessary to require that the probability of detecting an event with an angle φ was equal to the probability of detecting one with an angle $\varphi+\pi$.

Using track information and the azimuthal scattering angle φ, the x- and y-positions of the proton at the back scintillator plane was calculated for each event (examples of the histograms are shown in Fig. 4-7). A similar calculation was performed for a track with an angle of $\varphi+\pi$. Cuts were placed on the histograms shown in Fig. 4-7; the same cuts were placed on the calculation using the angle $\varphi+\pi$. If the event does not pass either set of cuts it is thrown out. In this way the needed symmetry was assured.

4.1.5 Residuals

A residual for a set of chamber planes can be calculated only if the checksums of all three planes are good. For a given event, cuts are imposed on the residuals for as many of the four sets as possible. As mentioned

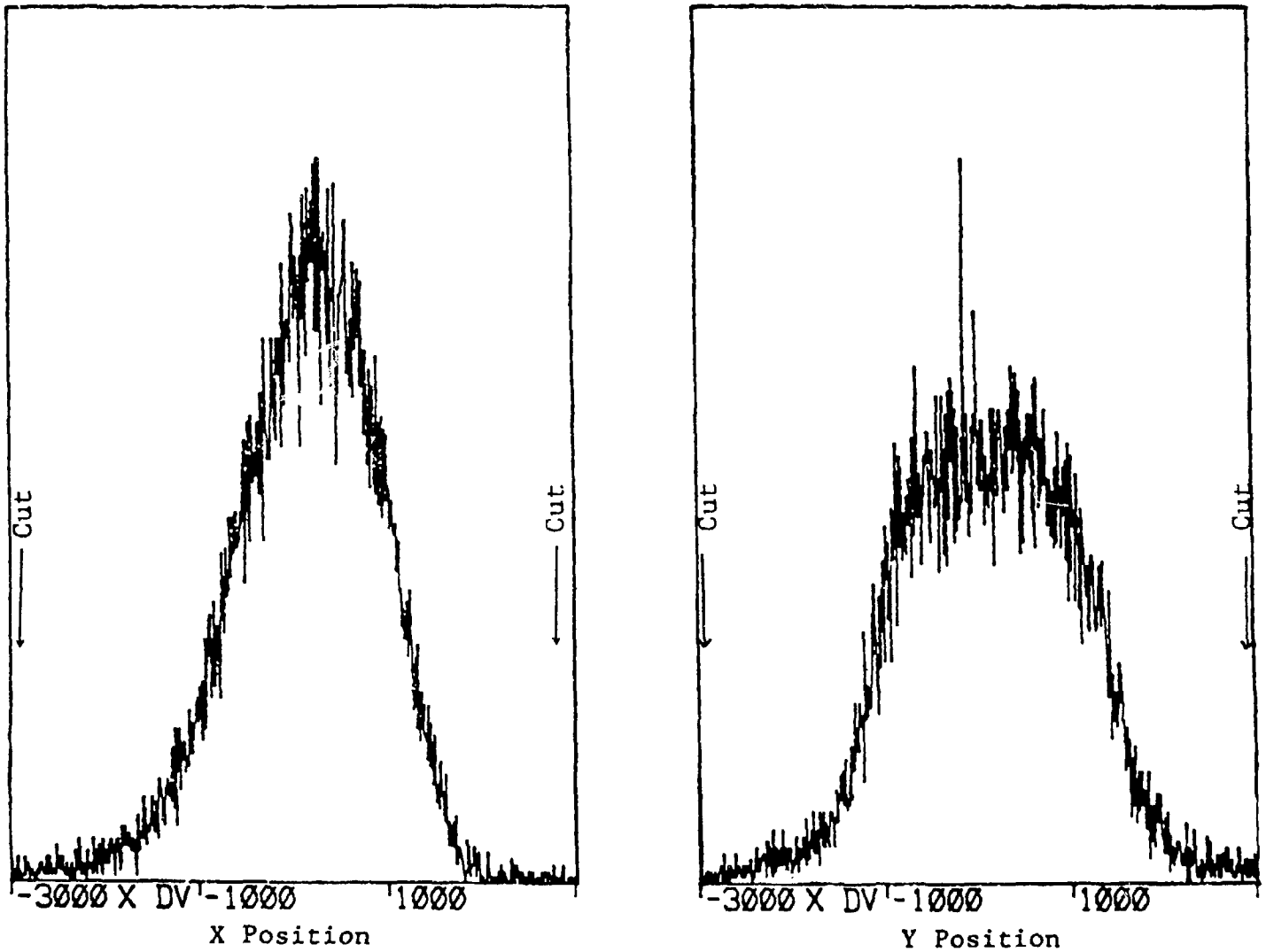

Figures 4-7

Examples of the Histograms showing:

a) X Positions, and b) Y Positions

at the Back JANUS Scintillator Plane

(Scale is 0.01 cm/channel)

above, the analysis required one of the four sets of chamber planes to have three good checksums so that at least one of the residual cuts could be applied. Cuts of ±1 mm were used for the residuals (again, this corresponds to the convention used by the three laboratories mentioned above).

4.1.6 Target Projections

The track information provided by the front Janus chambers and the front LAS chambers were projected back to the target to provide a "picture" of the target from both detectors. Fig. 4-8a shows a 2-dimensional histogram of the y-projection versus the x-projection for JANUS; Fig. 4-8b shows a similar histogram for the LAS. A cut is placed around the peaks to cut out background.

4.1.7 Time of flight

As mentioned in Secs. 2.2.3 and 2.2.4, time-of-flight difference (TOF) information was recorded for both the front-to-back scintillator planes on the LAS (or S1-PS2 for the pion telescope) and the front-to-front scintillators on the LAS (or pion telescope) and JANUS. Examples of these spectra are shown in Fig. 4-9. Again, cuts were placed around the peaks.

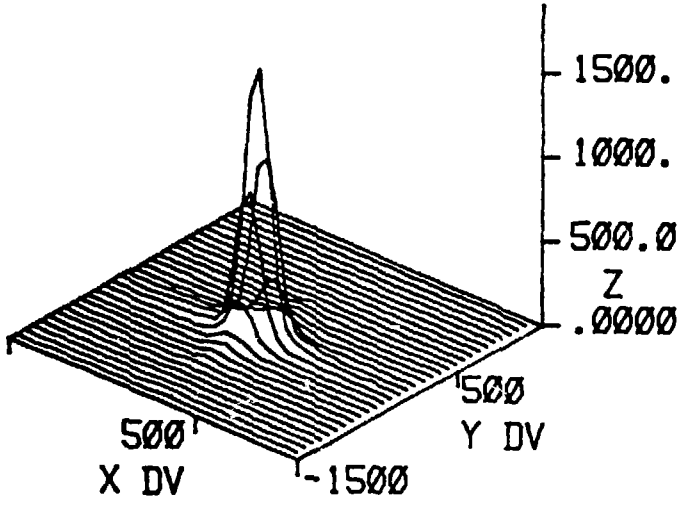

JANUS

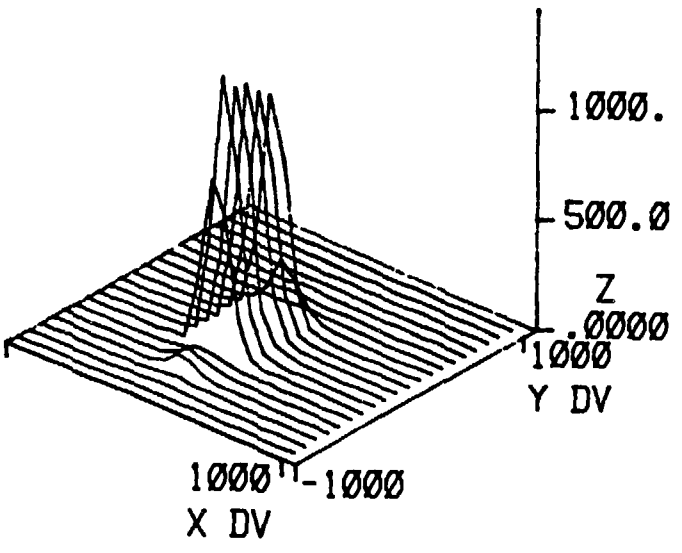

LAS

Figures 4-8

Example of Target Projections for:

a) JANUS, and b) the LAS

(Scale is 0.01 cm/channel)

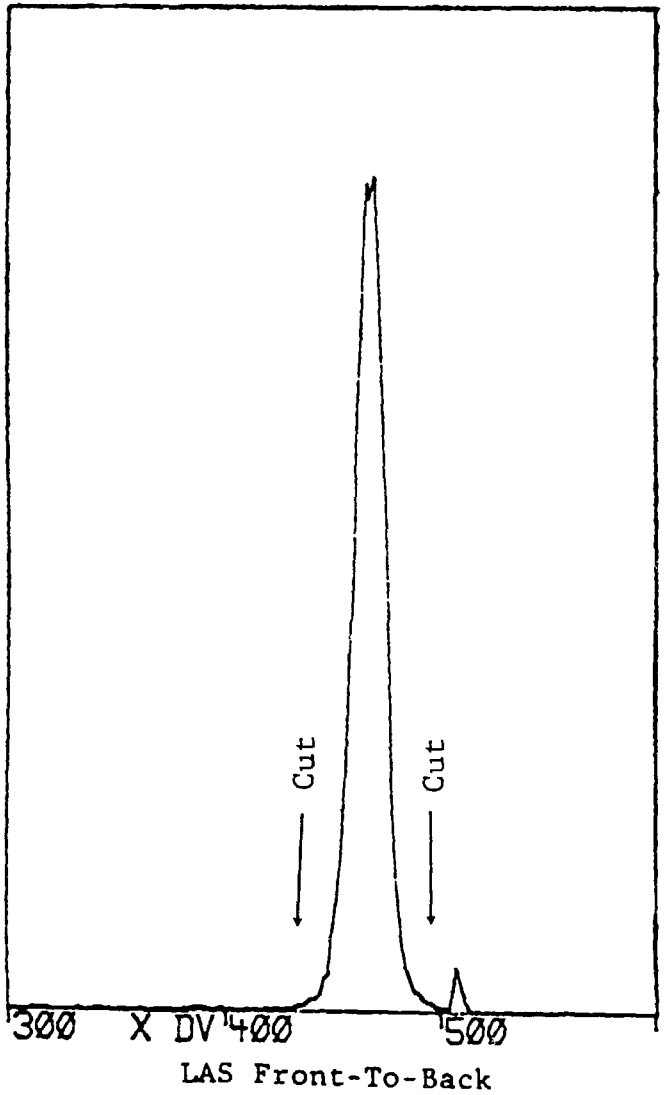

LAS Front-To-Back

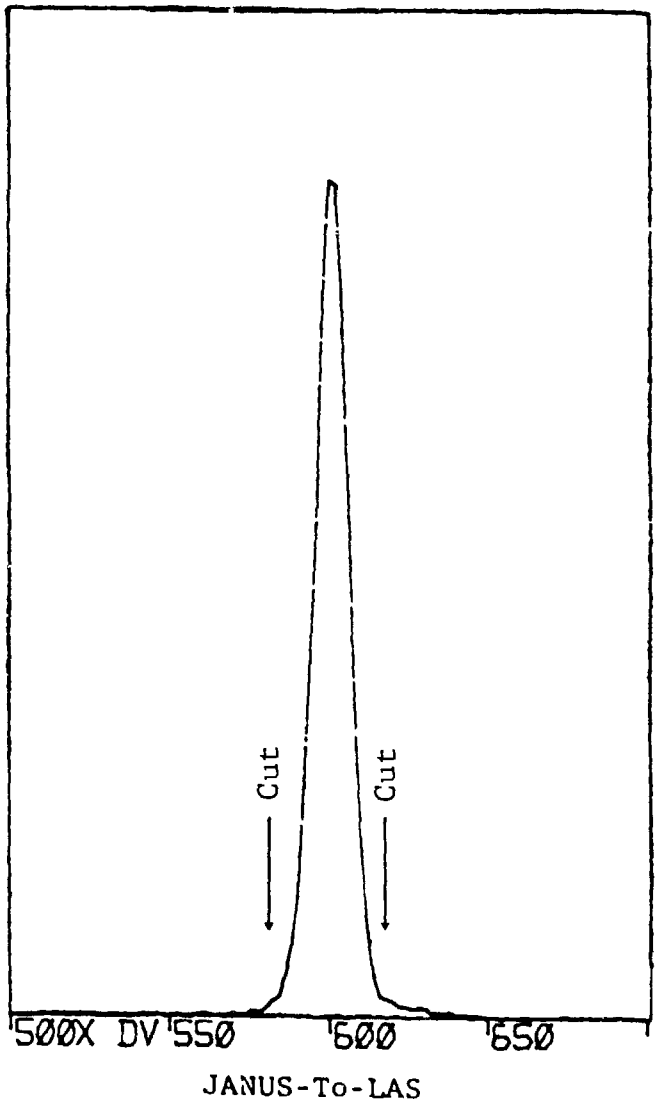

JANUS-To-LAS

Figure 4-9

Time-of-Flight Spectra for:

a) Front-to-Back of the LAS,

and b) Front of the LAS to Front of JANUS

(Scale is 100 ps/channel)

4.1.8 Pion Momentum

The momentum of a pion scattered at the central angle of the LAS spectrometer was calculated from two-body kinematics using the momentum of the beam pions and the value of the central angle. This value was then used in conjunction with track information provided by the LAS wire chambers to determine the momentum of the scattered pion for each event.

The path of a particle traversing a magnetic field of strength B directed perpendicularly to the velocity of the particle will curve with a radius r equal to

$$r = \frac{p_o}{qB} \quad , \qquad (4\text{-}1.1)$$

where p_o is the momentum of the particle and q is its charge. Solving Eq. (4-1.1) for p_o yields

$$p_o = qBr \quad . \qquad (4\text{-}1.2)$$

Fig. 4-10 depicts a particle of momentum p_o traversing the magnet of the LAS, which was positioned at a bend angle, θ_b, of 30°. Various distances and angles are also defined in this figure. From Fig. (4-10) it is easily seen from geometrical arguments that

$$d = r\sin\theta_n + r\sin(\theta_b - \theta_n)$$

and, therefore, that

$$p_o = \frac{qBr}{\sin\theta_n + \sin(\theta_b - \theta_n)} \quad . \qquad (4\text{-}1.3)$$

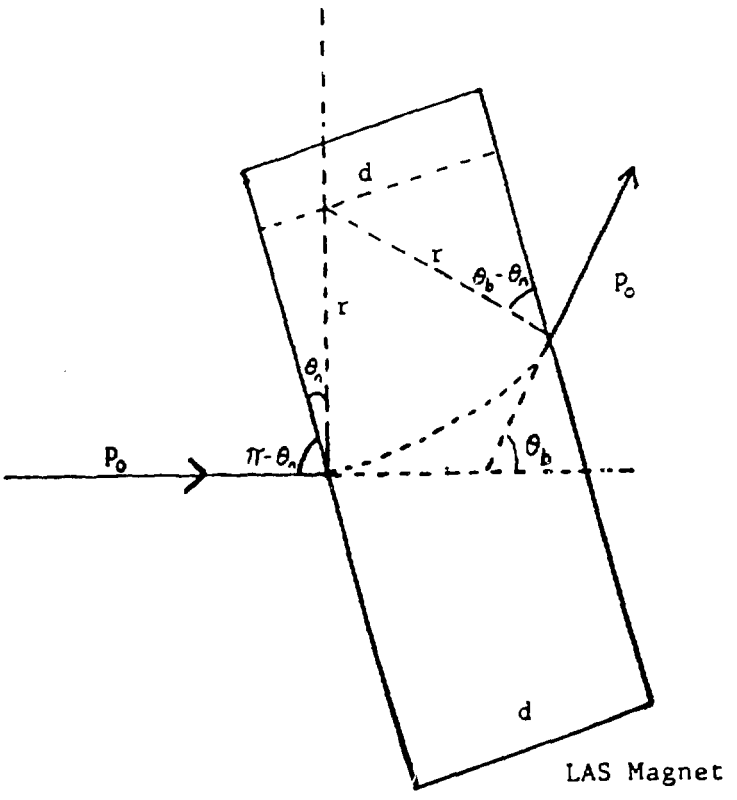

Figure 4-10

Particle of Momentum p_o Traversing the LAS Magnet

If θ_o and θ_d are defined as

$$\theta_o \equiv \tfrac{1}{2}\theta_b \ , \ \theta_d \equiv \theta_n - \theta_o \ ,$$

then Eq. (4-1.3) can be written as

$$p_o = \frac{qBr}{\sin(\theta_o+(\theta_n-\theta_o))+\sin(\theta_o-(\theta_n-\theta_o))}$$

$$= \frac{qBr}{2\sin\theta_o\cos\theta_d} \ . \qquad (4\text{-}1.4)$$

Fig. 4-11 depicts two particles traversing the LAS magnet, one with a momentum p_o and one with a different momentum p. The primed angles refer to the particle with momentum p. For this particle

$$p = \frac{qBr}{2\sin\theta_o'\cos\theta_d'} \ . \qquad (4\text{-}1.5)$$

Again, from geometrical arguments

$$\theta_n' = \theta_n + x_f \ ,$$

$$\theta_b' = \theta_b + (x_f - x_r) \ ,$$

$$\theta_o' = \frac{\theta_b'}{2} = \frac{\theta_b+(x_f-x_r)}{2} = \theta_o + \frac{x_f-x_r}{2} \ ,$$

$$\theta_d' = -\theta_o' + \theta_n' = (\theta_n+x_f) - (\theta_0+\frac{x_f-x_r}{2}) = \theta_d + \frac{x_f+x_r}{2} \ .$$

Eq. (4-1.5) becomes

$$p = \frac{qBr}{\sin(\theta_o+\frac{x_f-x_r}{2})\cos(\theta_d+\frac{x_f+x_r}{2})} \ . \qquad (4\text{-}1.6)$$

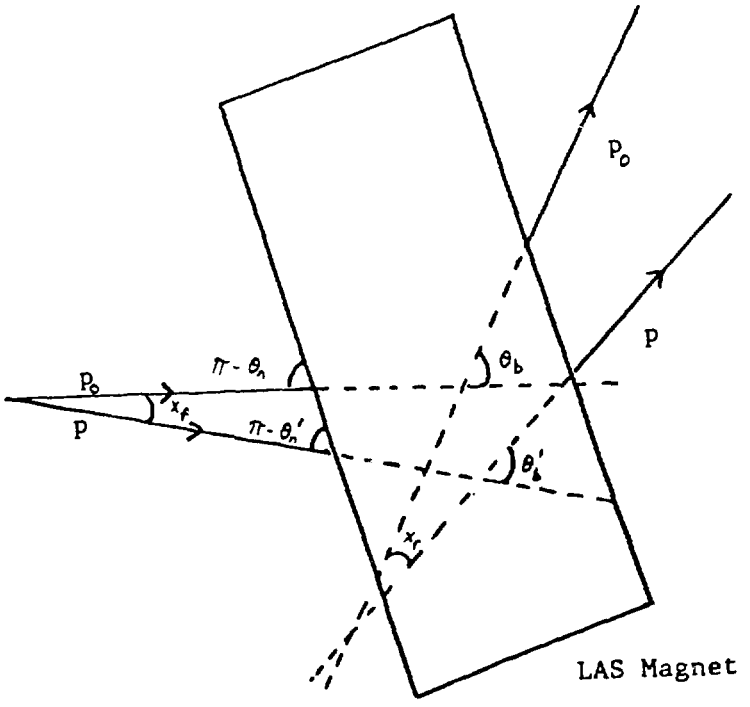

$$\pi - \theta_n = \pi - \theta_n' + x_f \Rightarrow \theta_n' = \theta_n + x_f$$

$$\theta_b + x_f = \theta_b' + x_r \Rightarrow \theta_b' = \theta_b + (x_f - x_r)$$

Figure 4-11

Two Particles of Different Momenta Traversing the LAS Magnet

The momentum is obtained by dividing Eq. (4-1.6) by Eq. (4-1.4):

$$\Delta \equiv \frac{p}{p_o} = \frac{\sin\theta_o \cos\theta_d}{\sin(\theta_o + \frac{x_f - x_r}{2})\cos(\theta_d + \frac{x_f + x_r}{2})} \quad . \qquad (4\text{-}1.7)$$

For the LAS spectrometer,

$$\theta_o = \tfrac{1}{2}\theta_b = 15^\circ \text{ and } \theta_d = \theta_n - \theta_o = 7.5^\circ .$$

The two angles x_f and x_r are calculated using the track information from the front and back wire chambers of the spectrometer. The momentum of the particle is then calculated using

$$p = p_o(1+\Delta) \ .$$

The histogram of this quantity is shown in Fig. 4-12. Cuts are place on this histogram to help reject background events.

Section 2: Determination of the Recoil Proton Polarization

4.2.1 Calculation of the Scattering Angles

Eq. (1-1.23) shows that, if the left-right asymmetry is measured and the carbon analyzing power is known, the recoil proton polarization can be determined. The left-right asymmetry depends upon the azimuthal scattering angle, φ, of each proton rescattering event in the carbon analyzer, while the carbon analyzing power depends upon the polar scattering angle, θ_C.

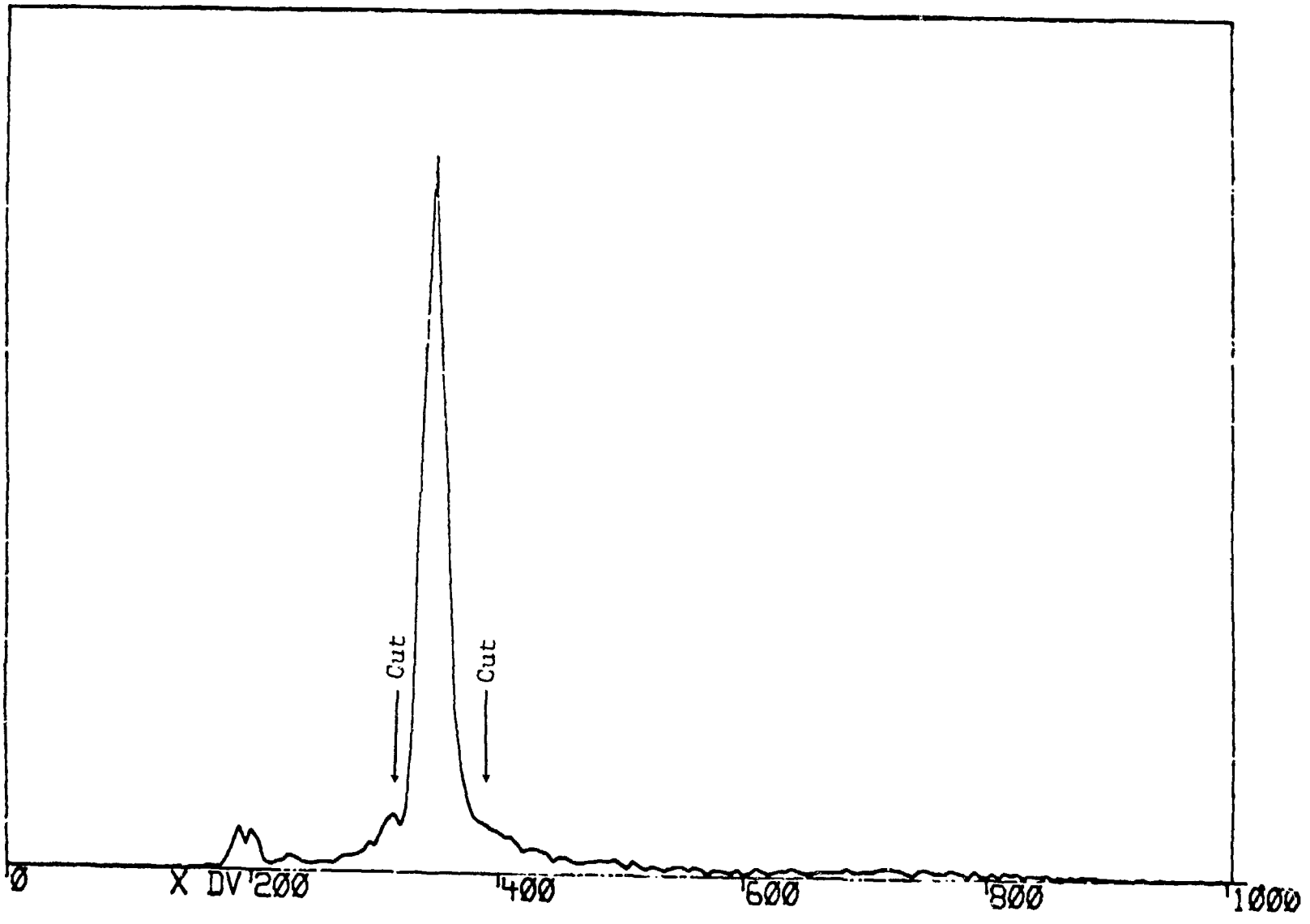

Figure 4-12

Example of the Pion Momentum Histogram for the LAS

(Scale is 1 MeV/c per channel)

Calculation of φ is complicated by the fact that the direction in which $\varphi = 0$ must be defined and consistently applied.

In order to make such a definition a coordinate system must be developed for the proton as it recoils from the LH_2 target. The following discussion refers to Fig. 4-13. The y-axis is defined to be

$$\hat{y} = \frac{\vec{k}_b \times \vec{k}_r}{|\vec{k}_b \times \vec{k}_r|} , \qquad (4\text{-}2.1)$$

where $\vec{k}_b$ is the incident pion momentum and $\vec{k}_r$ is the recoil proton momentum. The y-axis is perpendicular to the first scattering plane. The z-axis is then defined to be in this plane along $\vec{k}_r$; in order to form a right-handed coordinate system, the x-axis must also lie in the plane. In terms of this system, $\varphi = 0$ is defined to be along the positive x-axis.

The momentum of the proton after scattering from the carbon analyzer is called $\vec{k}_r'$. The two vectors $\vec{k}_r$ and $\vec{k}_r'$ form the plane of the second scatter. A perpendicular to to this scattering plane can be constructed by taking the cross product of $\vec{k}_r$ and $\vec{k}_r'$:

$$\hat{y}' = \frac{\vec{k}_r \times \vec{k}_r'}{|\vec{k}_r \times \vec{k}_r'|} . \qquad (4\text{-}2.2)$$

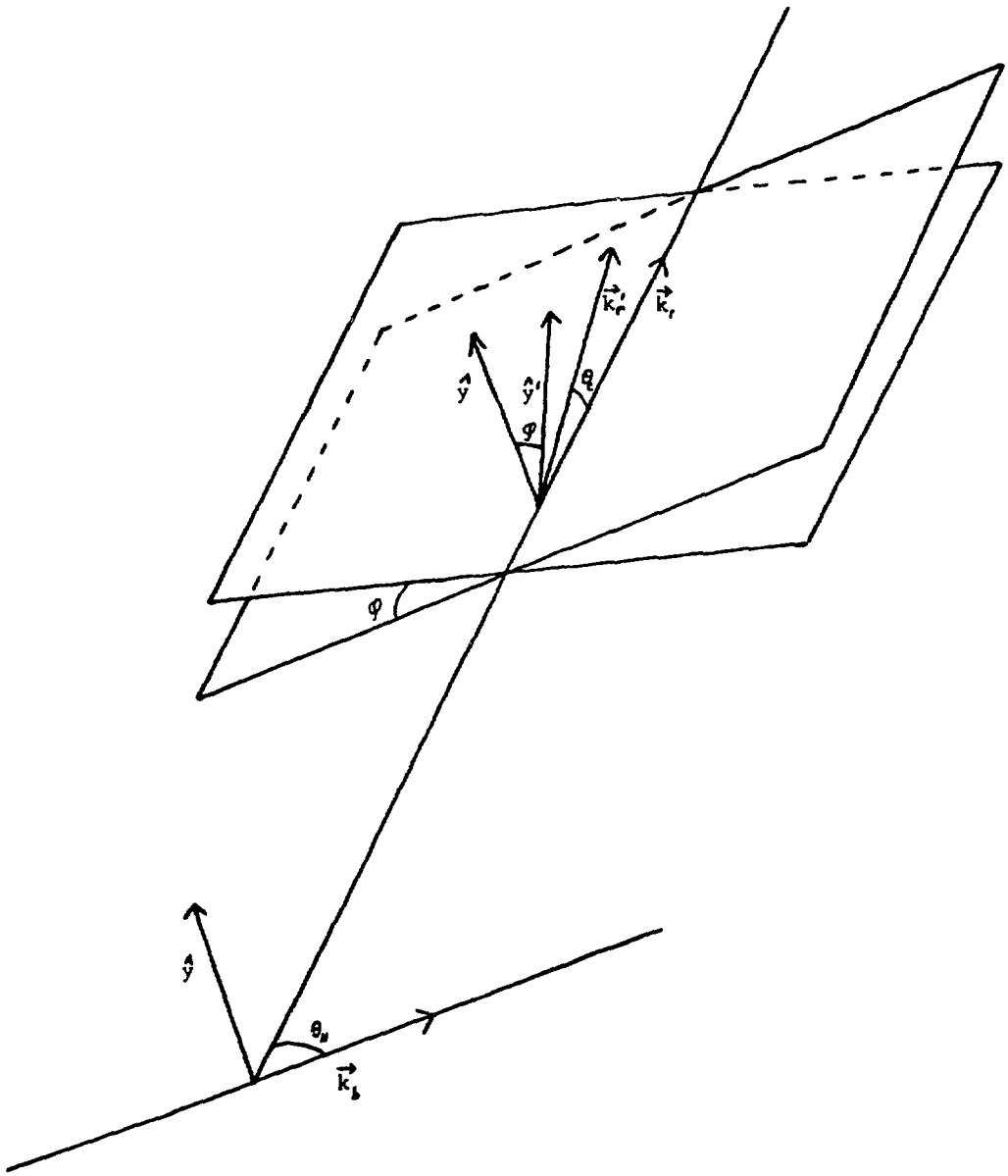

Figure 4-13

Definition of the Scattering Planes and the Azimuthal Scattering Angle

The angle φ is just the angle between the two scattering planes, which is also the angle between $\hat{y}$ and $\hat{y}'$.

For each event, the track of the recoil proton before it scattered from the carbon was calculated; this corresponded to the vector $\vec{k}_r$. This vector was crossed with a vector along the beam direction to determine $\hat{y}$. The track of the recoil proton after it scattered from the carbon was also calculated; this vector corresponded to $\vec{k}_r'$. The vector $\vec{k}_r$ was then crossed with $\vec{k}_r'$ as in Eq. (4-2.2) to produce y'. The angle φ was then simply obtained from the following relation:

$$\varphi = \cos^{-1}(\hat{y} \cdot \hat{y}') \quad . \tag{4-2.3}$$

The angle θ_C was calculated from the above quantities using the relation:

$$\theta_C = \cos^{-1} \frac{\vec{k}_r \cdot \vec{k}_r'}{|\vec{k}_r||\vec{k}_r'|} \quad . \tag{4-2.4}$$

4.2.2 The Carbon Analyzing Power

Besides having a large analyzing power over a wide energy region, the reason that carbon is the principal analyzer used in polarimeters is because its analyzing power is extremely well known. A comparison of measurements made at LAMPF,[31] TRIUMF,[32] and SIN[33] shows excellent agreement (Fig. 4-14). Before the recoil proton polarization could be calculated, values for the carbon

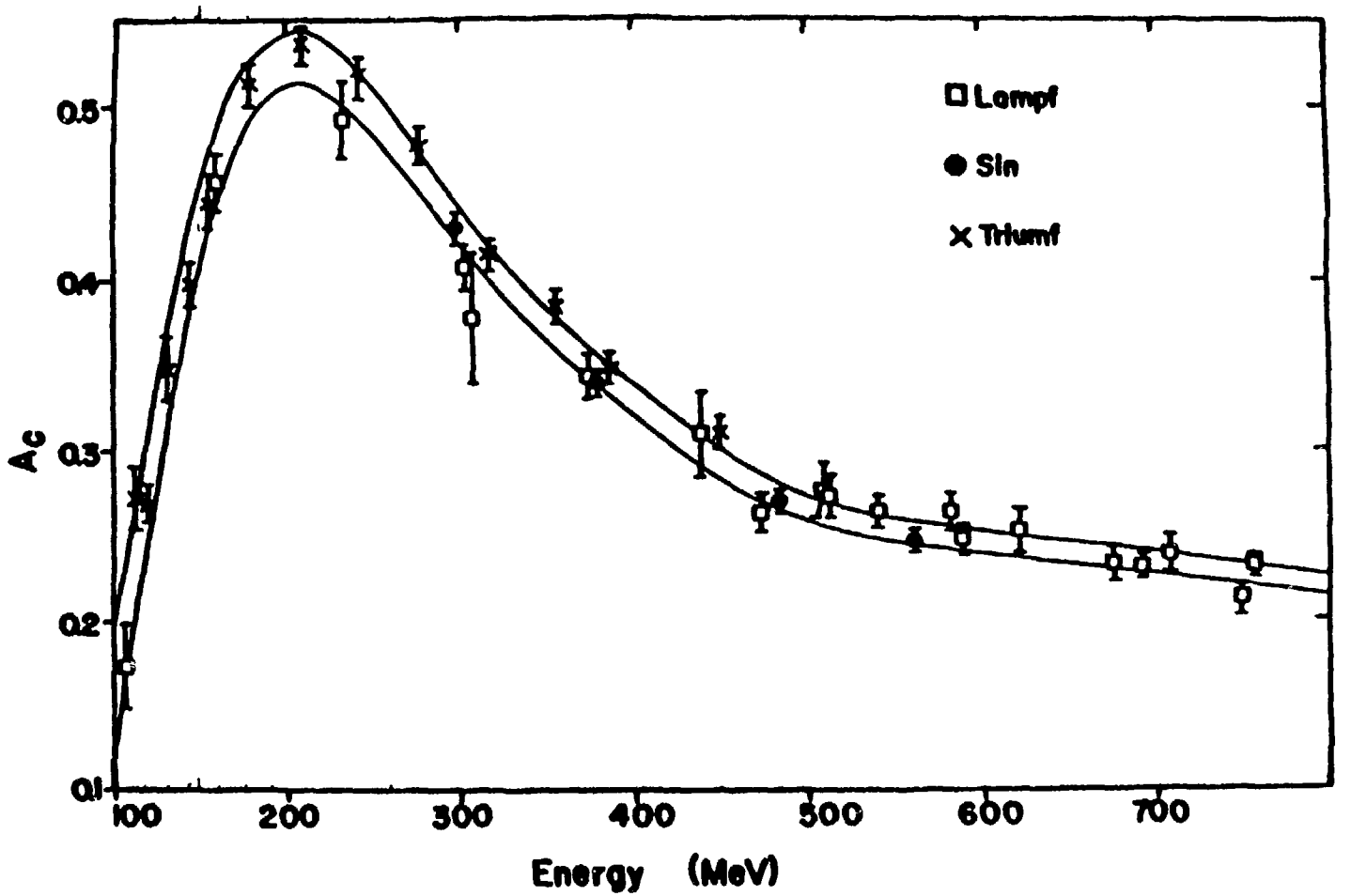

Figure 4-14

Comparison of A_c from LAMPF, TRIUMF, and SIN

analyzing power, A_C, had to be determined from the data set provided by these three labs.

To make use of this data, the analyzing power was parameterized as a function of both energy and angle. The parameterization found to give the best fit to the data in this energy region was[31]

$$A_C(\theta_C, E_C) = \frac{ar}{1+br^2+cr^4} ;$$

θ_C is the polar scattering angle as calculated in Sec. 4.1.1, E_C is the mean energy at the center of the carbon, and $r = p\sin\theta_C$ (where p is the recoil proton momentum). The coefficients a, b, and c are fit to the polynomials[31]

$$a = a_0 + a_1p' + a_2p'^2 + a_3p'^3 + a_4p'^4,$$

$$b = b_0 + b_1p' + b_2p'^2 + b_3p'^3 + b_4p'^4,$$

$$c = c_0 + c_1p' + c_2p'^2 + c_3p'^3 + c_4p'^4,$$

where $p' = p - 0.7$ GeV/c. The values determined by this fit are given in Table 4-2.

The energy of the proton at the center of the analyzer was determined by calculating the energy of the proton before entering the carbon and the energy loss of the proton through the carbon. The energy of the proton before entering the carbon was calculated from two-body kinematics

TABLE 4-2

COEFFICIENTS FOR THE PARAMETERIZATION OF A_c

	0	1	2	3	4
a	5.3346	-5.5361	2.8353	61.915	-145.54
b	-12.774	-68.339	1333.5	-3713.5	3738.3
c	1095.3	949.5	-28012.0	96833.0	-118830.0

using the pion beam energy and pion scattering angle. The energy loss of the pion was determined by an iteration of the Bethe-Bloch equation,[34] beginning with the original proton energy. A calculation was performed for every 0.5 mm of carbon. The resulting energy loss was then subtracted from the original proton energy to obtain E_C.

4.2.3 Calculation of the Asymmetries

In Chapter 1 the following equation was derived (Eq. 1-1.32):

$$I = I_o(1 + \epsilon_{UD}\sin\varphi + \epsilon_{LR}\cos\varphi) \ .$$

Since this equation only involves sine and cosine terms, Fourier analysis can be used to extract the up-down and left-right asymmetries. If I_o is assumed to be independent of φ then:

$$\epsilon_{UD} = (2/I_o)\int I(\varphi)\sin\varphi d\varphi \ ,$$

$$\epsilon_{LR} = (2/I_o)\int I(\varphi)\cos\varphi d\varphi \ .$$

$$1 = (2/I_0)\int I(\varphi)d\varphi \ .$$

By approximating the integrals with sums,[35]

$$\epsilon_{UD} = \frac{2\Sigma\sin\varphi}{N} \ ,$$

$$\epsilon_{LR} = \frac{2\Sigma\cos\varphi}{N} \ ,$$

where N is the number of events. The uncertainties can be

shown to be[35]

$$\sigma_{\epsilon_{LR}} = \left[\frac{2 - \epsilon_{LR}^2}{N}\right]^{\frac{1}{2}},$$

$$\sigma_{\epsilon_{UD}} = \left[\frac{2 - \epsilon_{UD}^2}{N}\right]^{\frac{1}{2}}.$$

In a real experiment I_o is directly related to the acceptance of the polarimeter, which is determined by the back scintillator plane. I_o is constant only if, for a given polar scattering angle θ, all values of the azimuthal scattering angle φ fall within the acceptance of the polarimeter. For events scattering near the edge of the polarimeter, this is not the case (see Fig. 4-15). Because such events would have to be thrown out if Fourier analysis were used, another method was adopted for the analysis.

The method used was developed by D. Besset[35] and allows events to be used as long as, for an a given θ, both φ and $\varphi+\pi$ are within the acceptance. In this case, the integrals can be expressed in the following form:

$$\int I(\varphi)\cos\varphi d\varphi = \epsilon_{LR}\int I(\varphi)\cos\varphi d\varphi + \epsilon_{UD}\int I(\varphi)\sin\varphi\cos\varphi d\varphi ,$$

$$\int I(\varphi)\sin\varphi d\varphi = \epsilon_{UD}\int I(\varphi)\sin\varphi d\varphi + \epsilon_{LR}\int I(\varphi)\sin\varphi\cos\varphi d\varphi .$$

These integrals can be estimated with sums and the two equations expressed in matrix form:

$$\begin{bmatrix}\Sigma\cos\varphi \\ \Sigma\sin\varphi\end{bmatrix} = \begin{bmatrix}\Sigma\cos^2\varphi & \Sigma\sin\varphi\cos\varphi \\ \Sigma\sin\varphi\cos\varphi & \Sigma\sin^2\varphi\end{bmatrix}\begin{bmatrix}\epsilon_{LR} \\ \epsilon_{UD}\end{bmatrix} . \quad (4\text{-}2.5)$$

The uncertainties in the asymmetries calculated using this

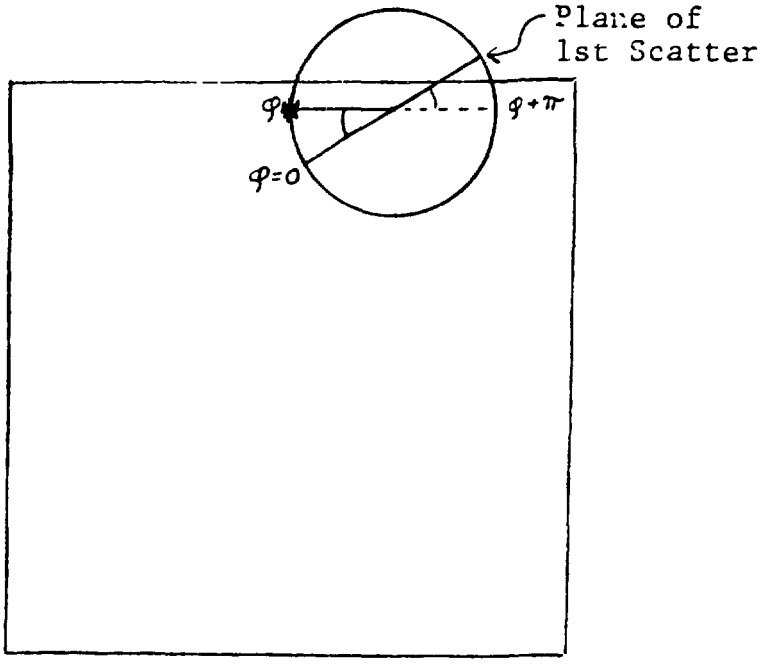

Example of event which would have been rejected if Fourier analysis had been used. Since both φ (the hit position of the event) and $\varphi+\pi$ are within the acceptance of the polarimeter, this even can be used in Besset's analysis.

Figure 4-15

Edge Effects of a JANUS Wire Chamber Plane

method become:[35]

$$\sigma_{\epsilon_{LR}} = \left[\frac{2 - (3/2)\epsilon_{LR}^2}{N}\right]^{\frac{1}{2}}.$$

$$\sigma_{\epsilon_{UD}} = \left[\frac{2 - (3/2)\epsilon_{UD}^2}{N}\right]^{\frac{1}{2}}.$$

4.2.4 Calculation of the Polarization

A series of data runs were made for each angle at each momentum. For each good event in a data run, the scattering angles were determined. The results were divided into twelve separate bins according to θ_C. (Some of the bins with small θ_C were excluded by the sinθ cut, so the number of actual bins used in the analysis varied with angle.)

Two different analyses were done. In the first, the five sums in Eq. (4-2.5) were obtained and the left-right and up-down asymmetries were determined for each bin for each data run. The analyzing power of carbon was determined for each bin using E_C and θ_C. A result for the transverse polarization and the polarization in the scattering plane was calculated for each data run by taking a weighted average of the results from the individual bins.

In the second method of analysis, the five sums were obtained by adding together the results of each individual run to form one large data set. The left-right and up-down

asymmetries and the analyzing power were then calculated for each θ_c bin in the combined data set and the polarizations determined. A final result for the transverse polarization was determined by taking a weighted average of the results from the individual bins of the combined set.

A comparison of the results from each data run with the result from the combined set served as a check on the consistency of the analysis.

CHAPTER 5

RESULTS AND CONCLUSIONS

Section 1: Consistency Checks

Tables 5-1 through 5-5 present the results for the transverse and in-plane polarization for each usable data run and the results for the combined data set at each of the five points presented here. These results, graphically shown in Figs. 5-1 and 5-2, show at least 75 percent of the individual measurements falling within one standard deviation of the combined measurement at each momenta. Tables 5-6 through 5-10 present the results of the combined data set for each of the five points for the different θ_c bins. These results, graphically presented in Figs. 5-3 and 5-4, also show excellent agreement. There is therefore no indication of any problems with consistency during data acquisition or data analysis.

Section 2: Results

The results of our measurements of the recoil proton polarization for π^+p and π^-p elastic scattering at 547 and 625 MeV/c are given in Table 5-11.

TABLE 6-1

COMPARISON OF DIFFERENT RUNS AT 547 MeV/c π^+, $\cos\theta_{CM} = -.26$

WITH THE COMBINED RUN

Run #	Transverse Polarization		Unc
139	0.05	+/-	.07
140	-0.03	+/-	.09
141	-0.04	+/-	.17
142	-0.06	+/-	.07
144	0.08	+/-	.12
145	0.13	+/-	.12
146	0.05	+/-	.09
149	-0.22	+/-	.11
150	0.05	+/-	.19
156	-0.10	+/-	.08
157	-0.44	+/-	.25
158	0.08	+/-	.09
159	0.21	+/-	.15
Total	0.00	+/-	.03

Run #	In-Plane Polarization		Unc
139	-0.21	+/-	.07
140	-0.02	+/-	.09
141	-0.13	+/-	.17
142	-0.02	+/-	.07
144	-0.09	+/-	.11
145	0.11	+/-	.12
146	-0.08	+/-	.07
149	-0.08	+/-	.11
150	-0.11	+/-	.19
156	-0.08	+/-	.08
157	0.70	+/-	.40
158	-0.21	+/-	.09
159	-0.11	+/-	.15
Total	-0.08	+/-	.03

TABLE 5-2

COMPARISON OF DIFFERENT RUNS AT 547 MeV/c π^-, $\cos\theta_{CM} = -0.5$

WITH THE COMBINED RUN

Run #	Transverse Polarization		Unc
106	1.16	+/-	.11
107	1.20	+/-	.09
108	0.87	+/-	.11
109	0.99	+/-	.14
110	1.11	+/-	.11
111	0.88	+/-	.14
112	0.97	+/-	.13
113	0.99	+/-	.14
Total	0.98	+/-	.04

Run #	In-Plane Polarization		Unc
106	0.00	+/-	.11
107	-0.17	+/-	.07
108	-0.14	+/-	.12
109	0.01	+/-	.15
110	0.06	+/-	.13
111	0.07	+/-	.12
112	0.13	+/-	.15
113	-0.03	+/-	.15
Total	-0.03	+/-	.05

TABLE 5-3

COMPARISON OF DIFFERENT RUNS AT 625 MeV/c π^+, $\cos\theta_{CM} = -.52$

WITH THE COMBINED RUN

Run #	Transverse Polarization		Unc
131	-1.29	+/-	.15
132	-0.95	+/-	.27
133	-0.91	+/-	.09
134	-0.83	+/-	.13
135	-1.16	+/-	.09
Total	-0.94	+/-	.05

Run #	In-Plane Polarization		Unc
131	-0.36	+/-	.18
132	0.95	+/-	.23
133	-0.05	+/-	.10
134	-0.13	+/-	.14
135	-0.01	+/-	.11
Total	-0.07	+/-	.06

TABLE 5-4

COMPARISON OF DIFFERENT RUNS AT 625 MeV/c π^-, $\cos\theta_{CM} = -.43$

WITH THE COMBINED RUN

Run #	Transverse Polarization		Unc
119	0.91	+/-	.16
120	0.58	+/-	.19
121	0.86	+/-	.18
122	0.84	+/-	.26
123	1.00	+/-	.09
124	0.96	+/-	.19
125	0.78	+/-	.15
Total	0.82	+/-	.06

Run #	In-Plane Polarization		Unc
119	0.24	+/-	.18
120	-0.35	+/-	.18
121	0.11	+/-	.20
122	-0.26	+/-	.29
123	-0.04	+/-	.11
124	-0.14	+/-	.21
125	0.42	+/-	.16
Total	0.09	+/-	.07

TABLE 5-5

COMPARISON OF DIFFERENT RUNS AT 625 MeV/c π^-, $\cos\theta_{CM} = -.52$

WITH THE COMBINED RUN

Run #	Transverse Polarization		Unc
126	0.82	+/-	.19
127	0.86	+/-	.12
128	0.68	+/-	.13
129	0.31	+/-	.21
Total	0.74	+/-	.08

Run #	In-Plane Polarization		Unc
126	-0.15	+/-	.20
127	-0.05	+/-	.13
128	-0.12	+/-	.14
129	0.21	+/-	.23
Total	0.04	+/-	.08

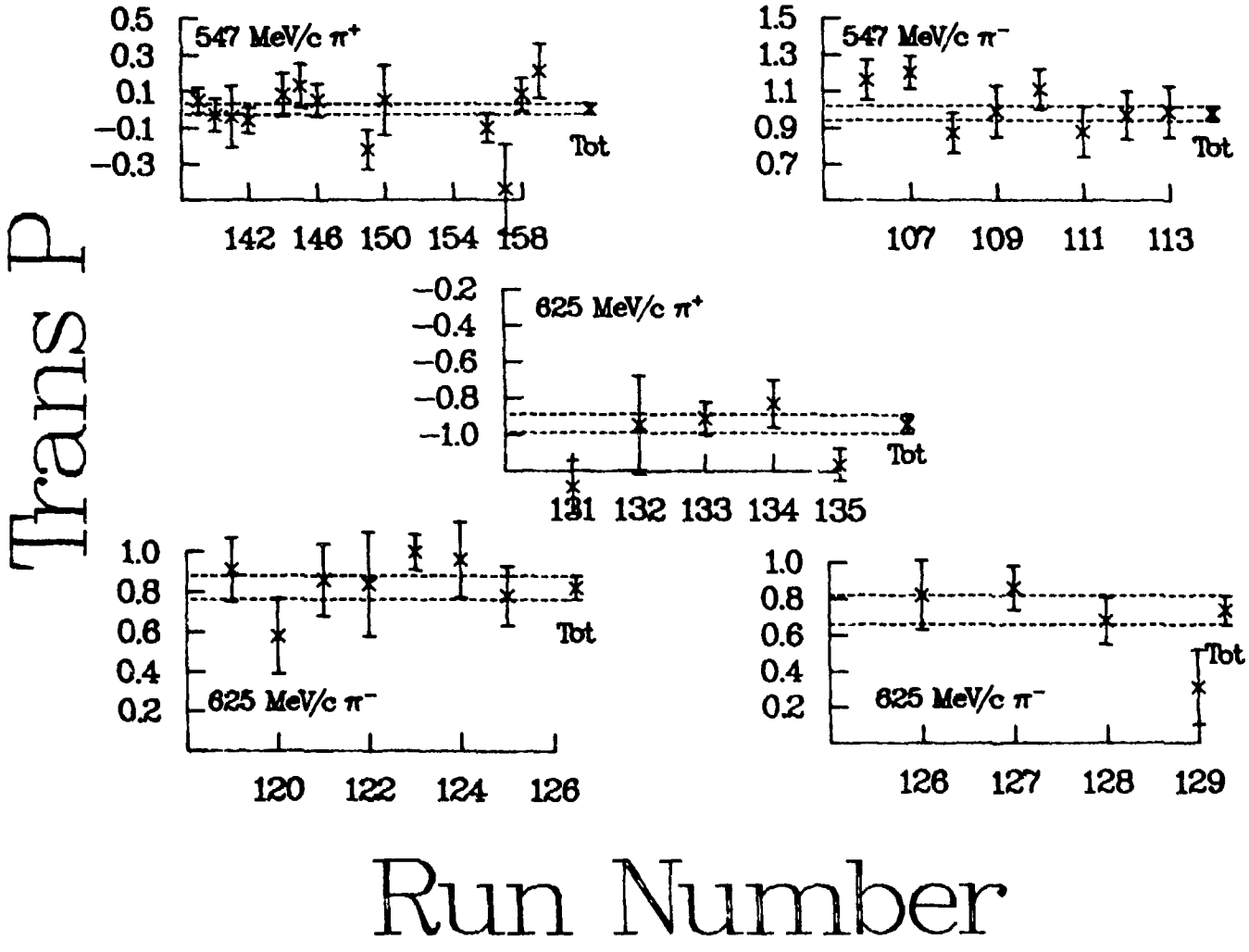

Figure 5-1

Comparison of the Transverse Polarization for

Different Runs of a Data Set

With the Combined Run

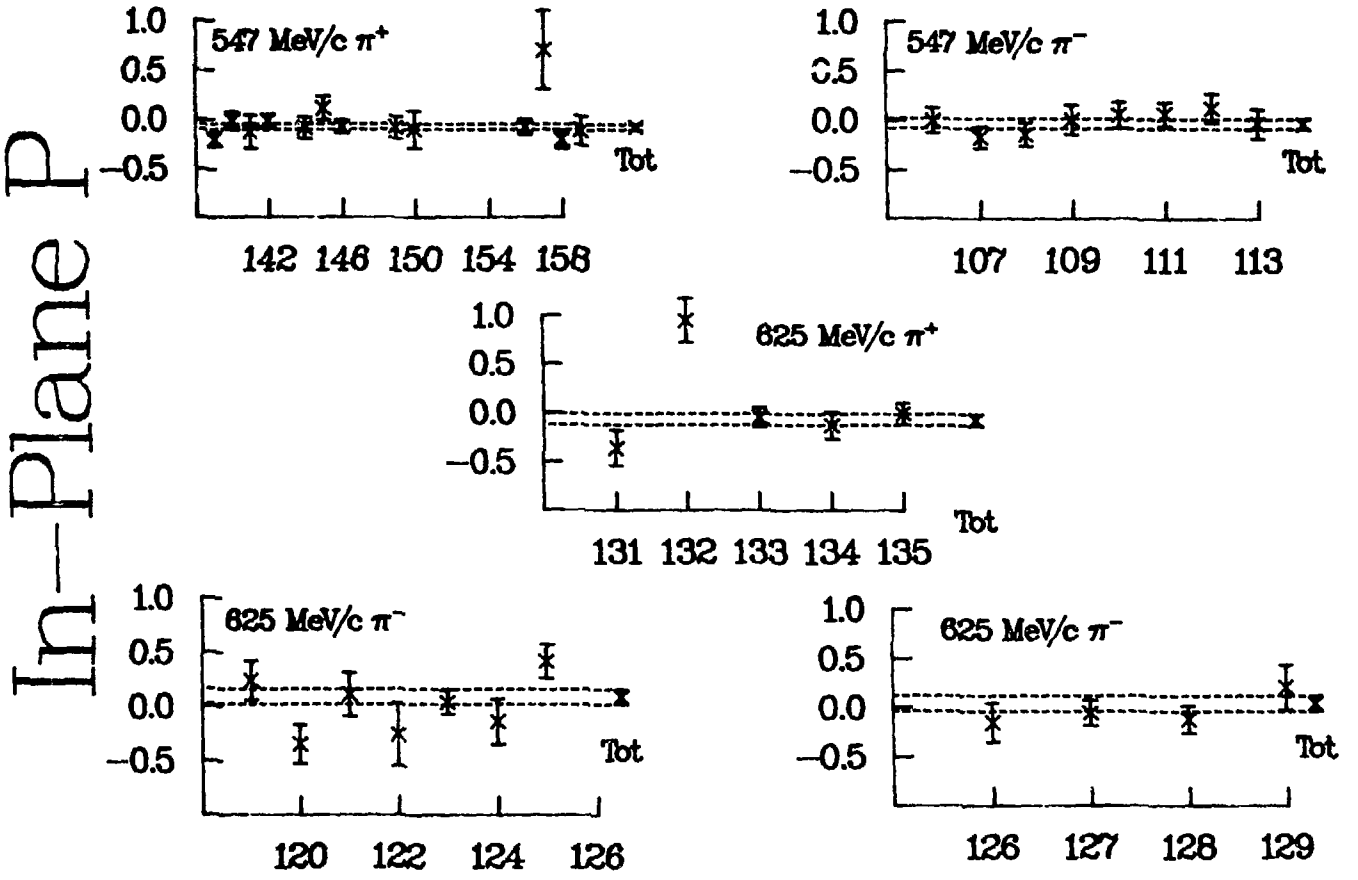

Figure 5-2

Comparison of the In-Plane Polarization for

Different Runs of a Data Set

With the Combined Run

TABLE 5-6

COMPARISON OF DIFFERENT BINS OF THE COMBINED DATA SET

AT 547 MeV/c π^+, $\cos\theta_{CM} = -0.26$

WITH THE WEIGHTED AVERAGE OF THE BINS

Bin #	Mean Angle(°)	Transverse Polarization		Unc
6	7.52	-0.01	+/-	.09
7	8.63	0.00	+/-	.08
8	9.80	-0.03	+/-	.07
9	11.26	0.07	+/-	.06
10	13.26	-0.02	+/-	.06
11	15.79	-0.05	+/-	.07
12	18.23	0.03	+/-	.13
Avg		0.00	+/-	.03

Bin #	Mean Angle(°)	In-Plane Polarization		Unc
6	7.52	-0.08	+/-	.09
7	8.63	-0.01	+/-	.08
8	9.80	-0.06	+/-	.07
9	11.26	-0.17	+/-	.06
10	13.26	-0.06	+/-	.06
11	15.79	-0.12	+/-	.07
12	18.23	0.03	+/-	.13
Avg		-0.08	+/-	.03

TABLE 5-7

COMPARISON OF DIFFERENT BINS OF THE COMBINED DATA SET

AT 547 MeV/c π^-, $\cos\theta_{CM} = -0.50$

WITH THE WEIGHTED AVERAGE OF THE BINS

Bin #	Mean Angle(°)	Transverse Polarization		Unc
5	6.36	1.11	+/-	.17
6	7.47	1.00	+/-	.15
7	8.63	0.91	+/-	.13
8	9.80	0.97	+/-	.11
9	11.26	0.97	+/-	.09
10	13.26	1.04	+/-	.09
11	15.79	0.88	+/-	.13
12	18.36	1.10	+/-	.23
Avg		0.98	+/-	.04

Bin #	Mean Angle(°)	In-Plane Polarization		Unc
5	6.36	-0.11	+/-	.17
6	7.47	0.18	+/-	.15
7	8.63	-0.09	+/-	.14
8	9.80	0.06	+/-	.12
9	11.26	0.00	+/-	.10
10	13.26	-0.09	+/-	.10
11	15.79	-0.12	+/-	.14
12	18.36	0.01	+/-	.26
Avg		-0.03	+/-	.05

TABLE 5-8

COMPARISON OF DIFFERENT BINS OF THE COMBINED DATA SET

AT 625 MeV/c π^+, $cos\theta_{CM} = -0.52$

WITH THE WEIGHTED AVERAGE OF THE BINS

Bin #	Mean Angle(°)	Transverse Polarization		Unc
5	6.36	-0.81	+/-	.20
6	7.46	-0.79	+/-	.17
7	8.63	-0.72	+/-	.16
8	9.81	-0.95	+/-	.13
9	11.25	-0.92	+/-	.11
10	13.26	-1.09	+/-	.12
11	15.82	-1.21	+/-	.18
Avg		-0.94	+/-	.05

Bin #	Mean Angle(°)	In-Plane Polarization		Unc
5	6.36	0.05	+/-	.21
6	7.46	-0.11	+/-	.18
7	8.63	0.18	+/-	.17
8	9.81	-0.50	+/-	.14
9	11.25	-0.02	+/-	.13
10	13.26	0.12	+/-	.14
11	15.82	-0.18	+/-	.20
Avg		-0.07	+/-	.06

TABLE 5-9

COMPARISON OF DIFFERENT BINS OF THE COMBINED DATA SET

AT 625 MeV/c π^-, $\cos\theta_{CM} = -0.43$

WITH THE WEIGHTED AVERAGE OF THE BINS

Bin #	Mean Angle(°)	Transverse Polarization		Unc
5	6.36	0.92	+/-	.23
6	7.52	0.50	+/-	.25
7	8.63	0.62	+/-	.21
8	9.80	0.95	+/-	.18
9	11.26	0.61	+/-	.16
10	13.27	0.79	+/-	.17
11	15.88	0.82	+/-	.24
12	18.55	1.05	+/-	.44
Avg		0.74	+/-	.08

Bin #	Mean Angle(°)	In-Plane Polarization		Unc
5	6.36	0.15	+/-	.24
6	7.52	0.05	+/-	.21
7	8.63	-0.08	+/-	.18
8	9.80	0.37	+/-	.18
9	11.26	-0.03	+/-	.14
10	13.27	0.29	+/-	.14
11	15.88	-0.20	+/-	.21
12	18.55	0.13	+/-	.50
Avg		0.09	+/-	.07

TABLE 5-10

COMPARISON OF DIFFERENT BINS OF THE COMBINED DATA SET

AT 625 MeV/c π^-, $\cos\theta_{CM} = -0.52$

WITH THE WEIGHTED AVERAGE OF THE BINS

Bin #	Mean Angle(°)	Transverse Polarization		Unc
6	7.52	0.51	+/-	.25
7	8.63	0.62	+/-	.21
8	9.80	0.95	+/-	.18
9	11.26	0.61	+/-	.16
10	13.27	0.79	+/-	.17
11	15.88	0.82	+/-	.24
12	18.55	1.05	+/-	.44
Avg		0.74	+/-	.08

Bin #	Mean Angle(°)	In-Plane Polarization		Unc
6	7.52	-0.08	+/-	.26
7	8.63	0.19	+/-	.22
8	9.80	-0.04	+/-	.20
9	11.26	-0.11	+/-	.17
10	13.27	-0.05	+/-	.19
11	15.88	-0.03	+/-	.25
12	18.55	0.52	+/-	.46
Avg		-0.04	+/-	.08

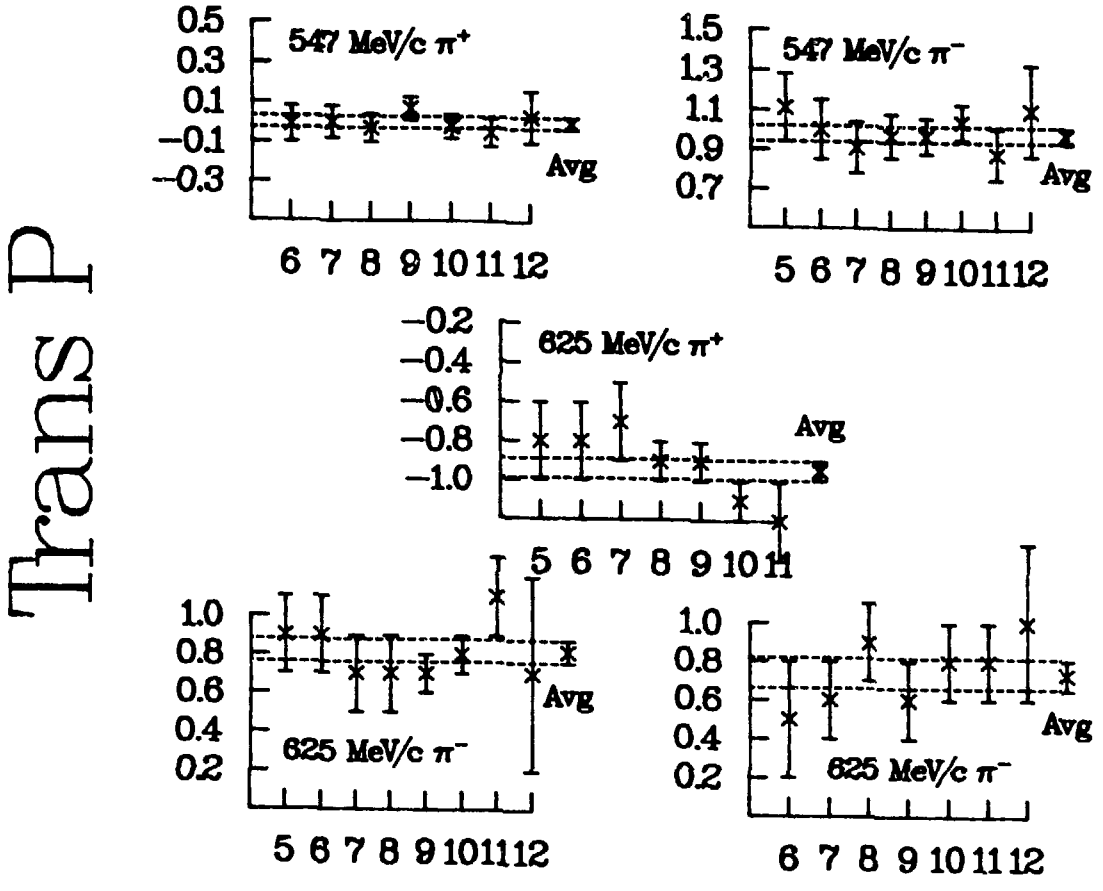

Figure 5-3

Comparison of the Transverse Polarization for

Different Bins of the Combined Data Set

With the Weighted Average of the Bins

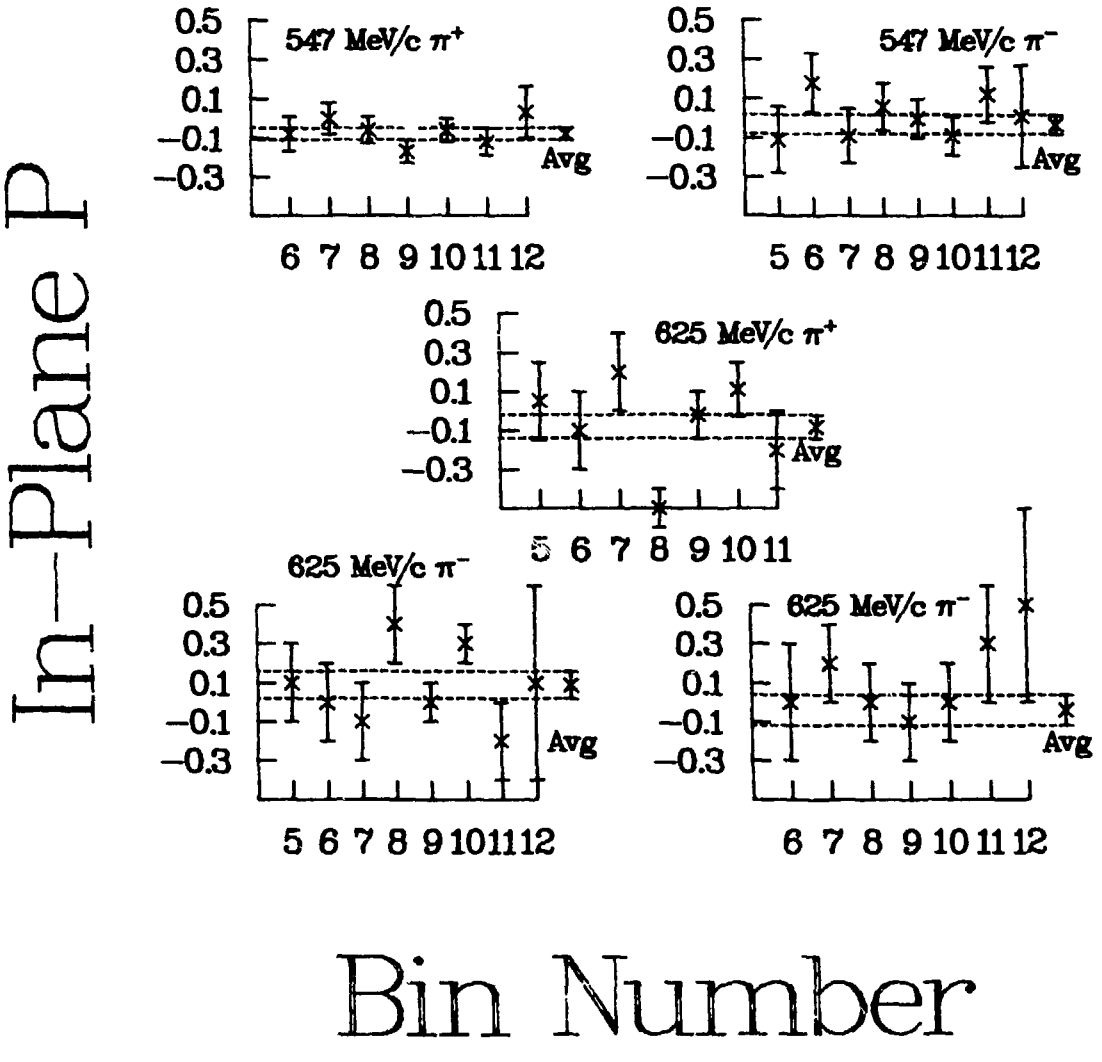

Figure 5-4

Comparison of the In-Plane Polarization for

Different Bins of the Combined Data Set

With the Weighted Average of the Bins

TABLE 5-11

RESULTS

Transverse Polarization

Mom	Polarity	$\cos\theta_{CM}$	Polarization		Unc
547	-	-0.50	0.98	+/-	.04
547	+	-0.26	0.00	+/-	.03
625	-	-0.43	0.82	+/-	.06
625	-	-0.52	0.74	+/-	.08
625	+	-0.52	-0.94	+/-	.05

Up-Down Polarization

Mom	Polarity	$\cos\theta_{CM}$	Polarization		Unc
547	-	-0.50	-0.03	+/-	.05
547	+	-0.26	-0.08	+/-	.03
625	-	-0.43	0.09	+/-	.07
625	-	-0.52	0.04	+/-	.08
625	+	-0.52	-0.07	+/-	.06

Also shown in Table 5-11 are the results of determining the polarization in the scattering plane using the up-down asymmetry. These results show that the up-down asymmetry is, within statistical errors, consistent with zero.

A more detailed presentation of the results for the transverse polarization obtained for π^+p elastic scattering at 547 MeV/c is given in Table 5-12. A comparison of the measurements obtained using the LAS spectrometer with measurements obtained using the pion telescope shows agreement between the two methods. Furthermore, a comparison of the measurements obtained using the pion telescope and JANUS with the measurements obtained with the detectors placed on the opposite sides of the beam also shows agreement. These results, combined with the fact that measurements of the up-down asymmetry were consistent with zero and the consistency of individual data runs and different θ_c bins, indicate that systematic uncertainties were well below statistical uncertainties. Therefore, the errors quoted are only statistical in nature.

Due to the large angular acceptance of the experimental apparatus (approximately 6° at the middle of the carbon analyzer in JANUS) the results may be divided into two separate angular bins. These results, shown in Table 5-13, help to map out the angular distributions near regions of interests (such as peaks or dips).

TABLE 5-12

COMPARISON OF RUNS AT 547 MeV/c π^+

	Polarization		Unc
With LAS Spectrometer	-0.01	+/-	.03
With Pion Telescope	0.00	+/-	.03
JANUS & Telescope Switched	0.01	+/-	.04

TABLE 5-13

RESULTS FOR THE TRANSVERSE POLARIZATION

(MORE THAN ONE BIN)

Mom	Polarity	$\cos\theta_{CM}$	Polarization		Unc
547	-	-0.48	0.99	+/-	.06
547	-	-0.51	1.03	+/-	.06
547	+	-0.25	0.00	+/-	.04
547	+	-0.27	0.00	+/-	.04
625	-	-0.42	0.89	+/-	.08
625	-	-0.45	0.77	+/-	.09
625	-	-0.50	0.79	+/-	.11
625	-	-0.53	0.66	+/-	.12
625	+	-0.50	-0.91	+/-	.08
625	+	-0.53	-0.93	+/-	.08

Section 3: Comparison to Previous Measurements

The results of Table 5-13 are presented graphically in Figs. 5-5 through 5-8, together with this group's previous measurements of the analyzing power (Mokhtari et al.[20]) and the polarization measurements of Bareyre et al.[36,37]

At 547 MeV/c, the results of this experiment agree, within the errors, to those of Bareyre. Bareyre's results at 617 MeV/c show good qualitative agreement with those from this experiment; the difference in momentum between the two experiments precludes a more quantitative measure.

The results from the measurement of the analyzing power by Mokhtari et al. also agree well with this experiment's results, with one exception. Mokhtari's measurement of A_n for $\cos\theta_{CM} = -0.47$ at 547 MeV/c π^- was a single-arm measurement in which only the protons were detected;[20] it is therefore subject to a larger systematic uncertainty than his coincidence measurements. Overall, there is no indication of any violation of the polarization-analyzing power equality.

Section 4: Comparison to Partial-Wave Analyses

Figs. 5-9 through 5-12 show the results of this experiment with those of the three partial-wave analyses

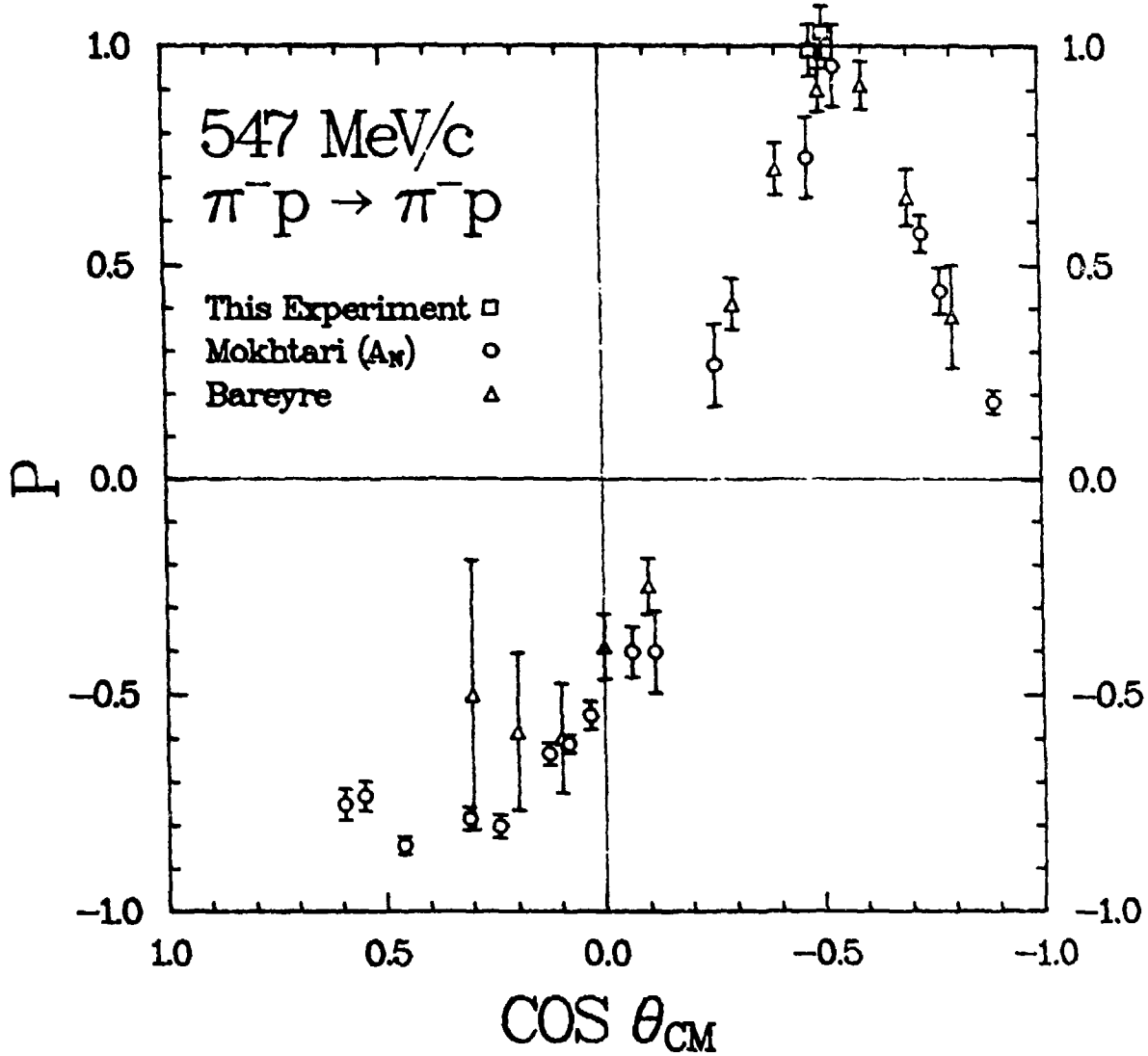

Figure 5-5

Results from this Experiment, Mokhtari et al.,

and Bareyre et al. for 547 MeV/c π^-

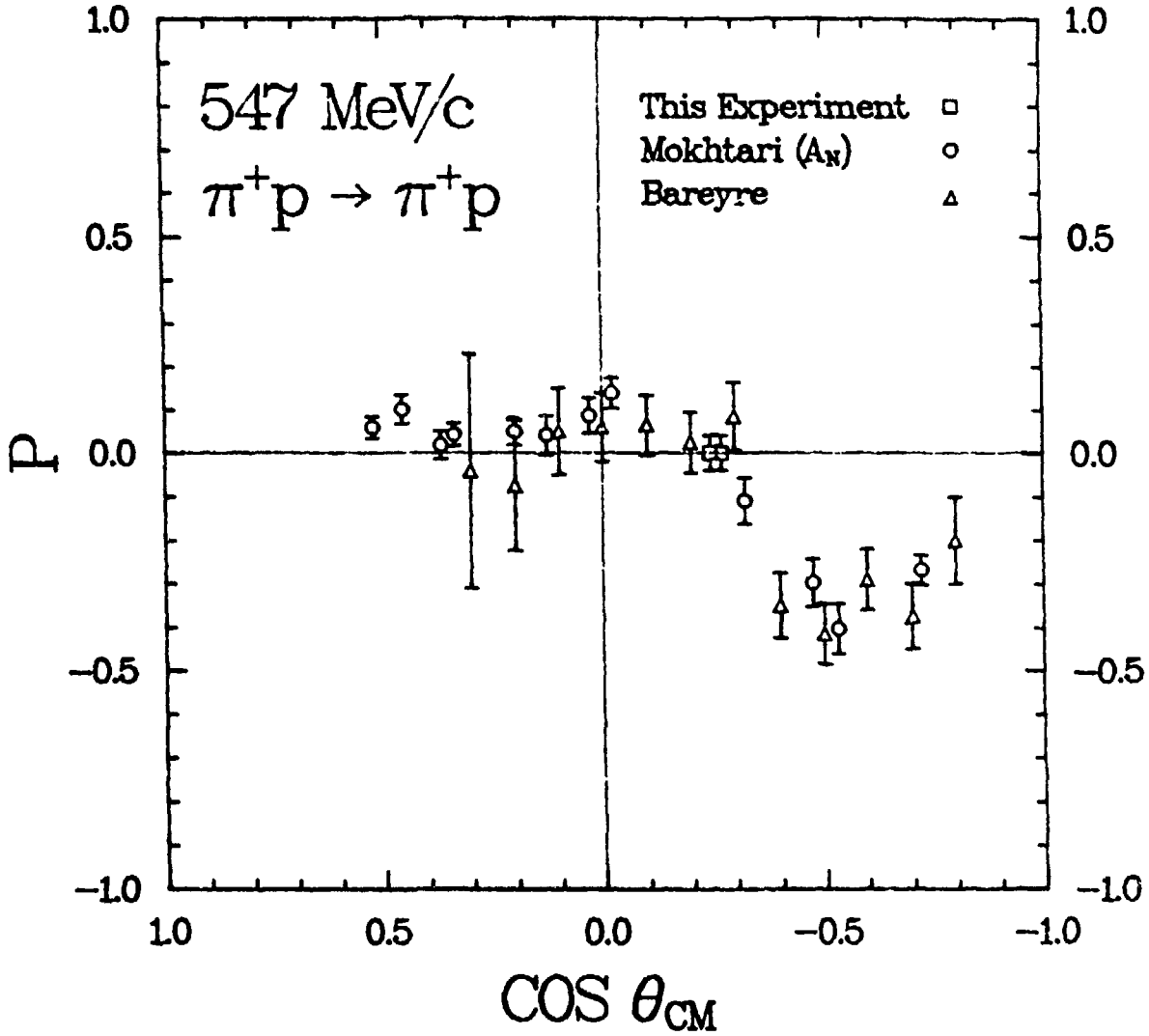

Figure 5-6

Results from this Experiment, Mokhtari et al.,

and Bareyre et al. for 547 MeV/c π^+

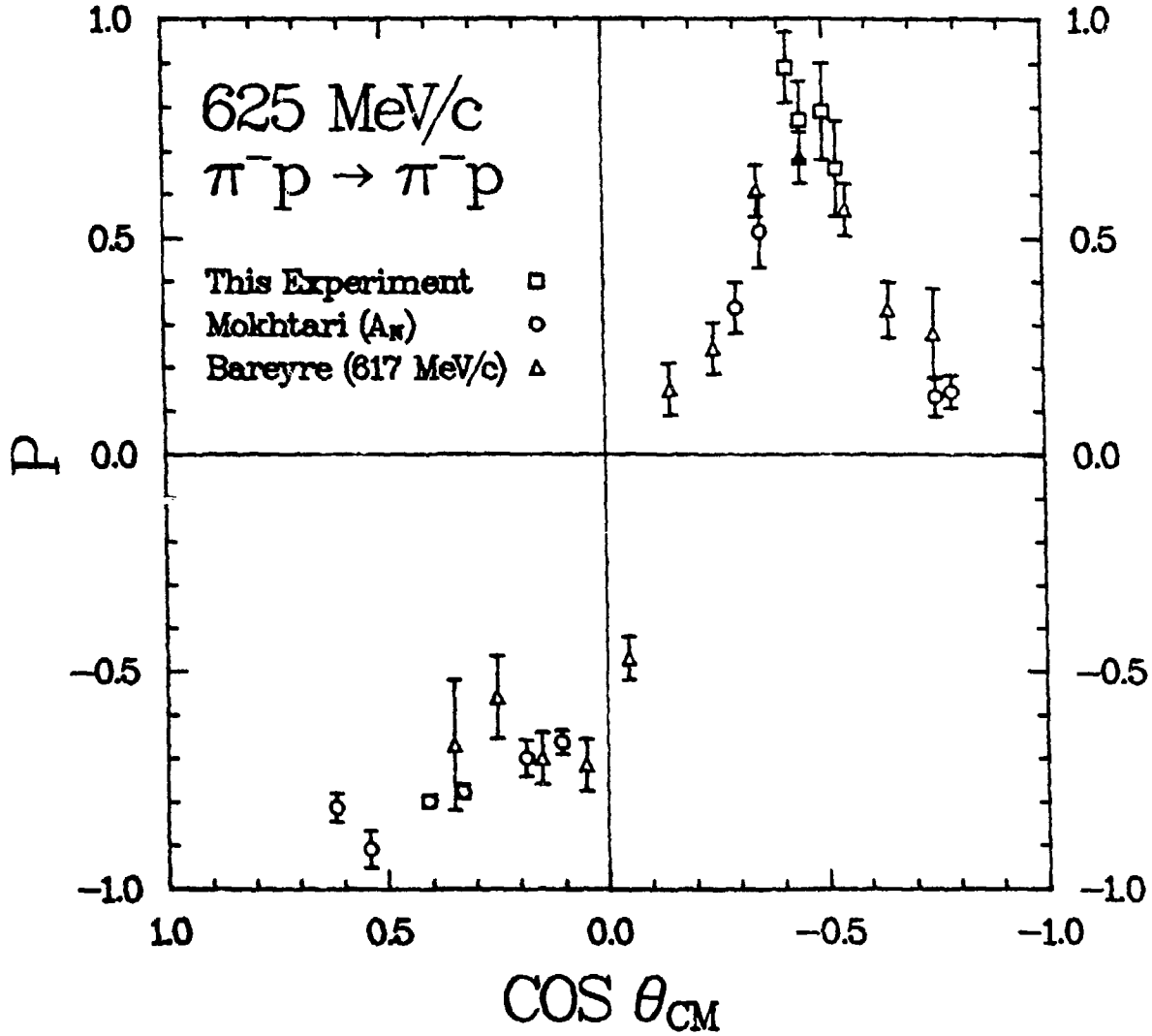

Figure 5-7

Results from this Experiment and Mokhtari et al.

at 625 MeV/c, and

Bareyre et al. at 617 MeV/c π^-

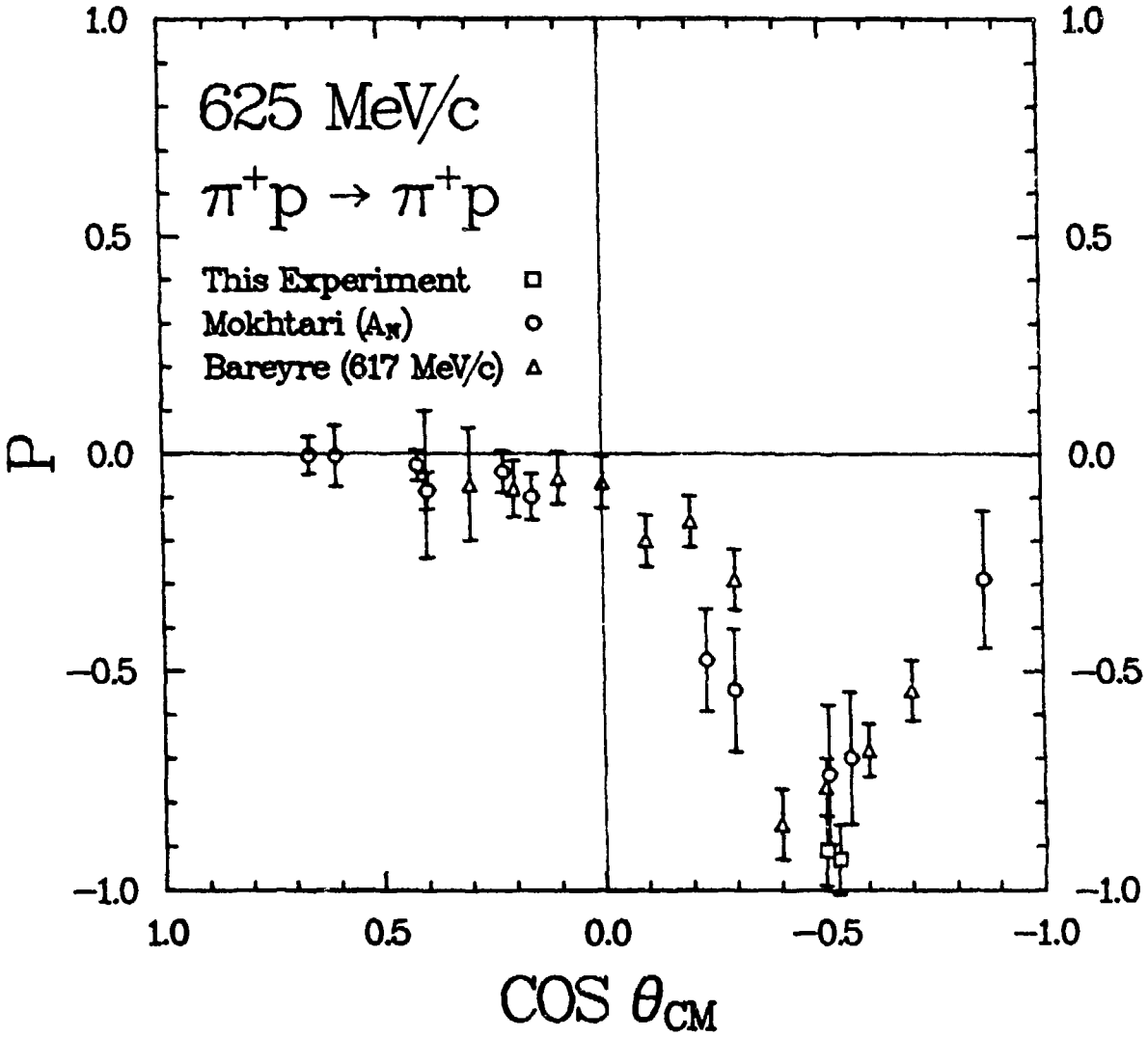

Figure 5-8

Results from this Experiment and Mokhtari et al.

at 625 MeV/c, and

Bareyre et al. at 617 MeV/c π^+

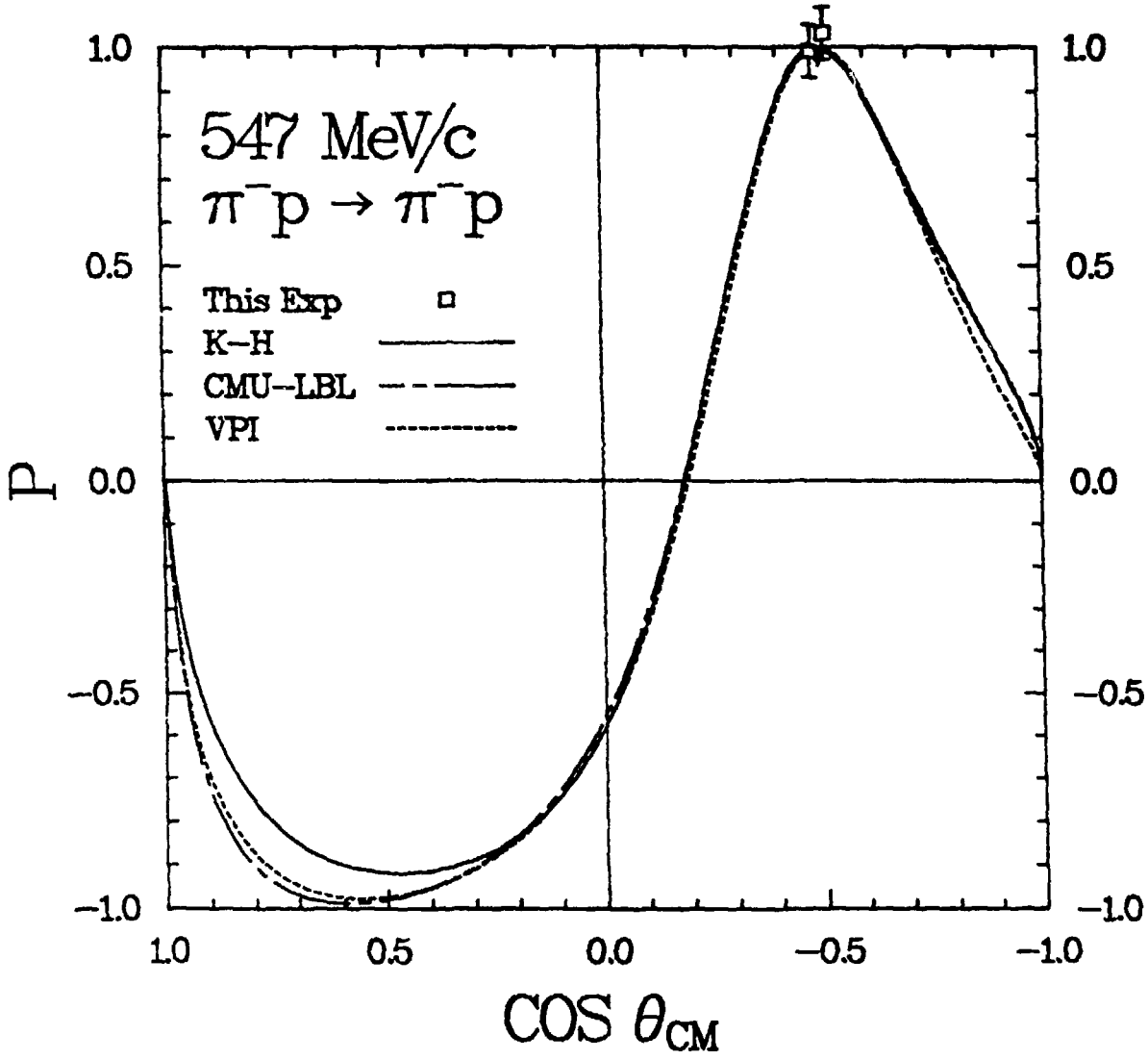

Figure 5-9

Results from this Experiment Compared to Partial-Wave Predictions from K-H, CMU-LBL, and VPI for 547 MeV/c π^-

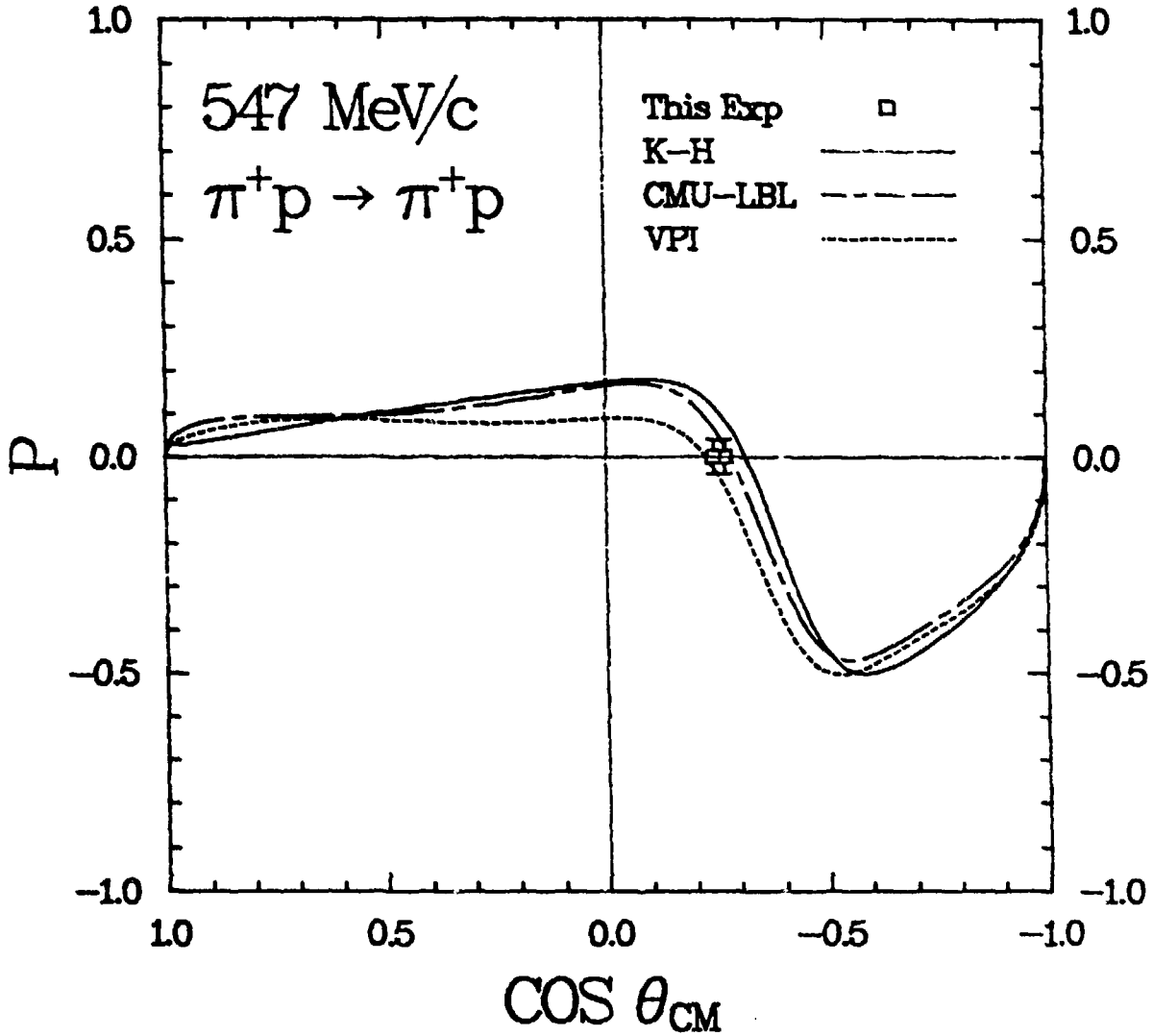

Figure 5-10

Results from this Experiment Compared to Partial-Wave Predictions from K-H, CMU-LBL, and VPI for 547 MeV/c π^+

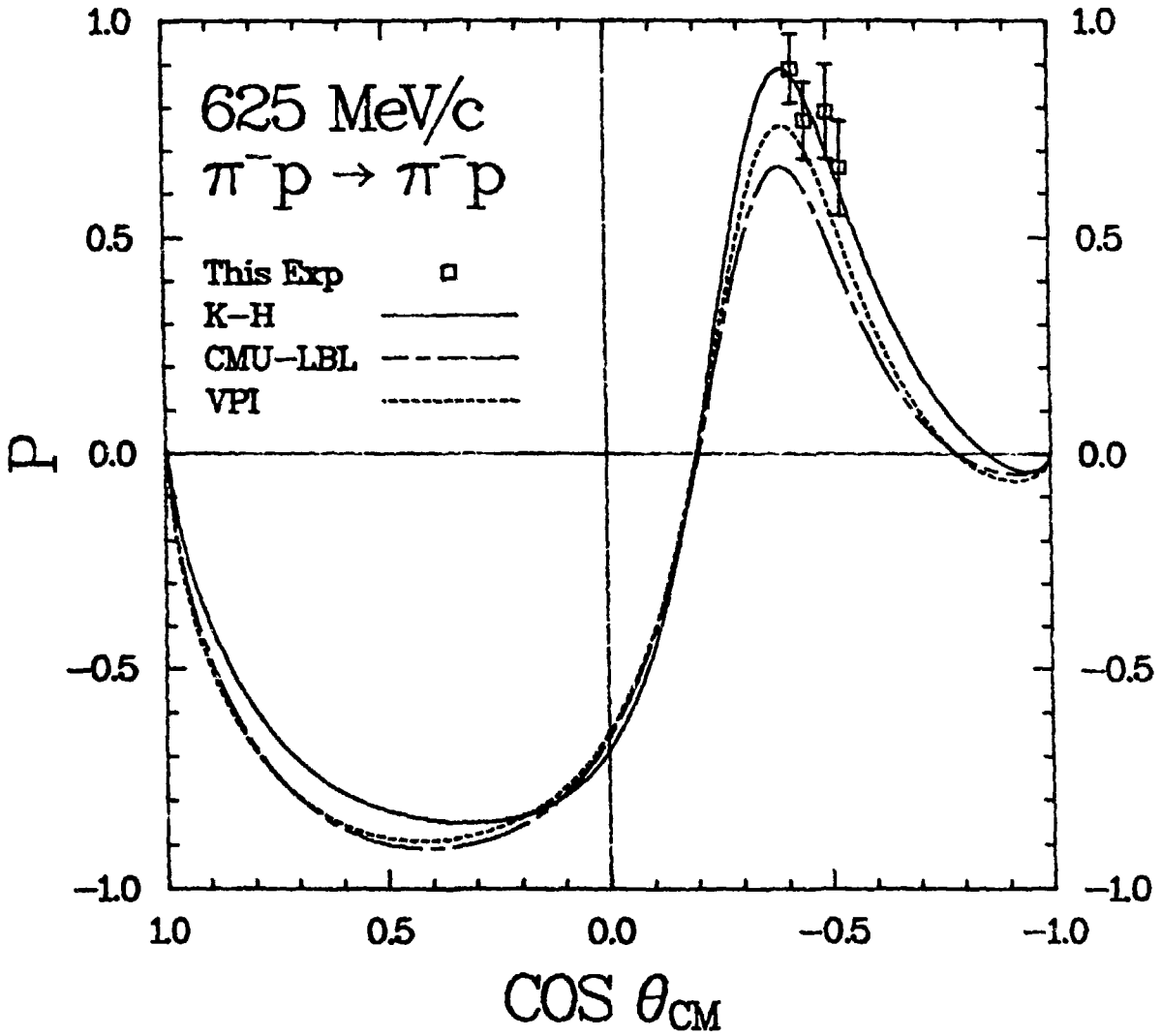

Figure 5-11

Results from this Experiment Compared to Partial-Wave Predictions from K-H, CMU-LBL, and VPI for 625 MeV/c π^-

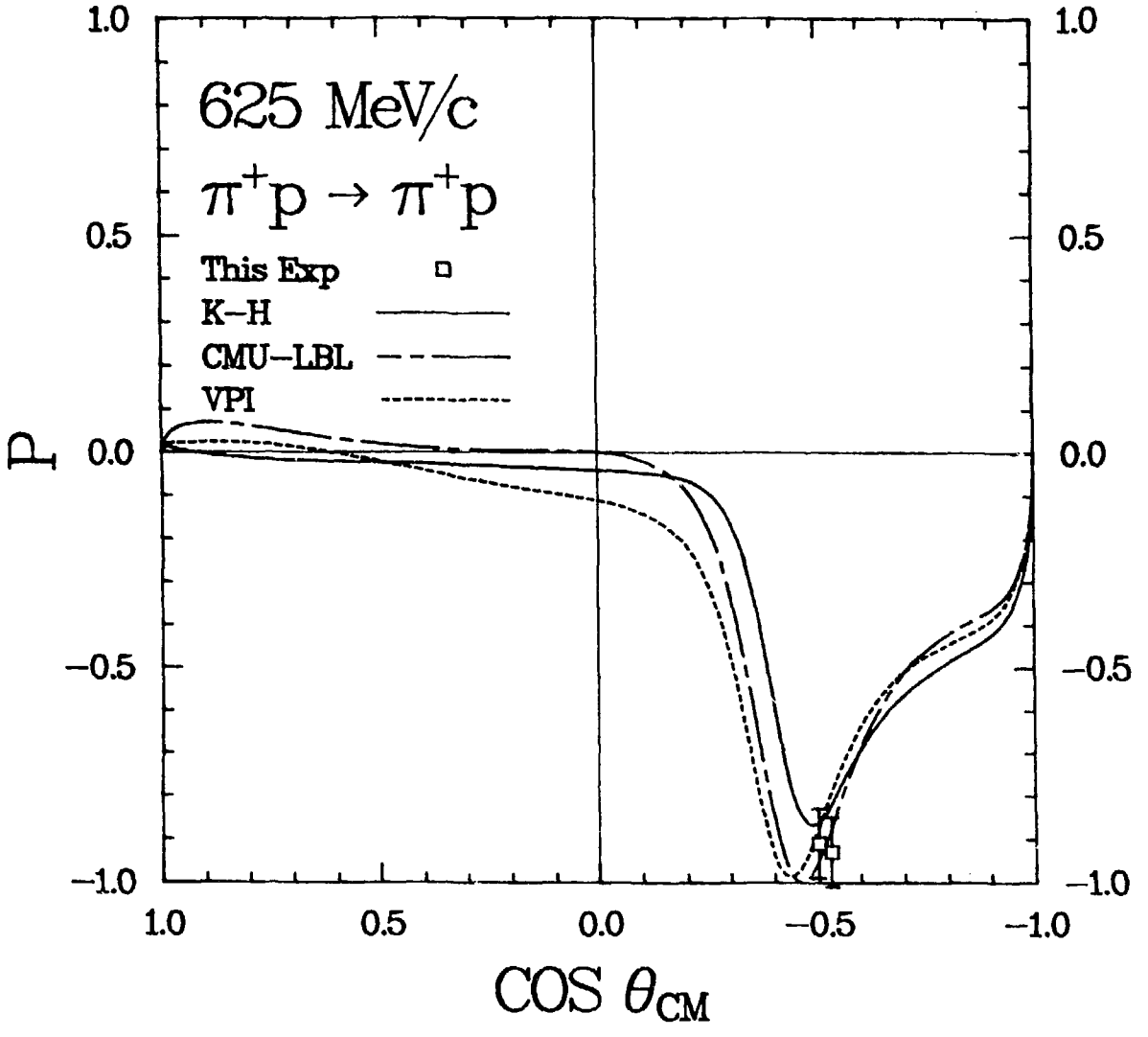

Figure 5-12

Results from this Experiment Compared to Partial-Wave Predictions from K-H, CMU-LBL, and VPI for 625 MeV/c π^+

discussed in Chap. 1.[15-17] Of the three analyses, only those of VPI contain the results of Mokhtari et al.

For 547 MeV/c π^-, all three analyses agree, within the errors, to the results presented here. The results at 547 MeV/c π^+ agree with both the VPI and CMU-LBL solutions. The results at 625 MeV π^- and π^+ favor the K-H solution, although the VPI solution falls just outside the error bars

The KH analysis has recently been updated to include more recent πN measurements, including those of Refs. 19-22. Preliminary results from this analysis agree, within the error bars, to all of the results contained here.[38]

Section 5: Summary and Conclusions

The results from this experiment can be summarized as follows:

1) The results obtained using the pion telescope agree with those using the LAS spectrometer. Furthermore, the results obtained by placing JANUS at the same angle but on the opposite side of the beam line and the pion telescope at the same angle but on the opposite side of the beam line agree with those obtained when the two detectors were at their original positions. Therefore, there is no indication of any large systematic uncertainties resulting from instrumental asymmetries.

2) The agreement between these measurements and the measurements of the analyzing power performed by Mokhtari et al. indicate the successful calibration of the JANUS polarimeter in the high background area of P^3 East.

From the results shown, the following conclusions can be drawn:

1) Preliminary results from the updated KH analysis show slightly better agreement with the results presented here than does the VPI solution. However, a better judgement can be made only upon the completion of the analysis for the spin-rotation parameters and the incorporation of the data set into both analyses.

2) Except at $\cos\theta_{CM} = -0.47$ for 547 MeV/c π^-, the results presented here agree, within experimental error, with the results of Mokhtari et al. for the analyzing power. The single-arm measurement of the analyzing power performed at $\cos\theta_{CM} = -0.47$ was subject to larger systematic uncertainties than his coincidence measurements. The disagreement between it and the measurement of the recoil polarization indicates that the value obtained for A_n at this point should be used with caution. Overall, there is no indication of the violation of the polarization-

analyzing power equality and, as a result, no indication of parity violation.

After analysis is completed on the last two parameters needed for a complete data set, the next logical step would be to conduct experiments at higher energies (especially since the present data set ends at the onset of the P_{11} resonance). Unfortunately, such experiments must wait for a higher energy pion factory.

APPENDIX A

A COMPLETE SET OF MEASUREMENTS

A.1 The Spin Rotation Parameters for πN Scattering

In the following discussion, the incident pion beam momentum is assumed to lie along the z-direction and the initial polarization of the target to lie in the scattering (x-z) plane along the x-axis: $\vec{P}_i = P_i\hat{x}$. From Eq. (1-1.19), the polarization of the recoil proton (multiplied by the differential cross section) becomes

$$I_o\vec{P}_f = (|f|^2-|g|^2)P_i\hat{x} + (f^*g+fg^*)\hat{y} + i(fg^*-f^*g)P_i(\hat{x}\times\hat{y}). \tag{A-1}$$

A transformation is made from this initial reference frame, S, to a new frame, S', where z' lies along the direction of the recoil proton momentum. The two frames are related by a rotation around the y-axis by the scattering angle, θ:

$$x = x'\cos\theta + z'\sin\theta$$

$$y = y'$$

$$z = -x'\sin\theta + z'\cos\theta$$

By substituting into Eq. (1-1.19) for P_f and using the fact that

$$2\mathrm{Im}(fg^*) = -i(fg^*-f^*g) ,$$

Eq. (1-1.19) becomes

$$I_o\vec{P}_f = \left[(|f|^2-|g|^2)P_i\cos\theta + 2\mathrm{Im}(fg^*)P_i\sin\theta\right]\hat{x}'$$

$$+ (f^*g + fg^*)\hat{y}'$$

$$+ \left[(|f|^2-|g|^2)P_i\sin\theta - 2\mathrm{Im}(fg^*)P_i\cos\theta\right]\hat{z}' \quad .$$

If the A and R parameters are defined by:

$$I_oA \equiv (|f|^2 - |g|^2)\sin\theta - 2\mathrm{Im}(fg^*)\cos\theta \qquad (A\text{-}2)$$

$$I_oR \equiv (|f|^2 - |g|^2)\cos\theta + 2\mathrm{Im}(fg^*)\sin\theta \qquad (A\text{-}3)$$

then $\vec{P}_f$ becomes

$$\vec{P}_f = RP_i\hat{x}' + A_n\hat{y}' + AP_i\hat{z}' \quad . \qquad (A\text{-}4)$$

A and R can be rewritten by noting that, from Eqs. (1-1.12) (1-1.13), and (1-1.14),

$$|f+g|^2 = |f|^2 + |g|^2 + (f^*g+fg^*) = I_o(1+A_n)$$

$$|f-g|^2 = |f|^2 + |g|^2 - (f^*g+fg^*) = I_o(1-A_n) \quad .$$

Therefore,

$$(f+g) = \sqrt{I_o(1+A_n)}\; e^{i(\alpha-\beta/2)}$$

$$(f-g) = \sqrt{I_o(1-A_n)}\; e^{i(\alpha+\beta/2)}$$

which define the phase factors α and β. Multiplying the first equation above by the complex conjugate of the second

gives

$$|f|^2 - |g|^2 - (fg^* - f^*g) = I_0\sqrt{(1-A_n^2)}\,(\cos\beta - i\sin\beta) ,$$

$$|f|^2 - |g|^2 - 2i\,\mathrm{Im}(fg^*) = I_0\sqrt{(1-A_n^2)}\,(\cos\beta - i\sin\beta) .$$

Equating the real and imaginary parts gives

$$|f|^2 - |g|^2 = I_0\sqrt{(1-A_n^2)}\cos\beta ,$$

$$2\,\mathrm{Im}(fg^*) = I_0\sqrt{(1-A_n^2)}\sin\beta .$$

Upon substituting the above relations into Eqs. (A-2) and (A-3), A and R become

$$R = \sqrt{(1-A_n^2)}\cos(\beta-\theta) , \qquad (A-5)$$

$$A = \sqrt{(1-A_n^2)}\sin(\theta-\beta) . \qquad (A-6)$$

A and R are called spin rotation parameters because β is the angle by which the projection of the spin in the scattering plane is rotated.[39]

From the above relations it can be seen that

$$A^2 + R^2 + P^2 = 1. \qquad (A-7)$$

A.2 Measurement of A and R

A measurement of A and R again involves rescattering the recoil proton from a carbon analyzer. For the following discussion the coordinate system of Sec. (1.1.3) will again be used. From Eq. (A-2),

$$\vec{P} = (RP_{ix}, A_n, AP_{iz}) .$$

Substitution into Eq. (1-1.15) yields

$$I = I_o(1 - A_n R P_{fx} \sin\varphi + A_n A P_{fy} \cos\varphi) \ . \qquad (A\text{-}8)$$

Eq. (1-1.28) now becomes

$$\left[\frac{d\sigma}{d\Omega}\right]_{\varphi=\pi/2} \equiv U = I_o(1 - A_n R P_{ix}) \ , \qquad (A\text{-}9)$$

and Eq. (1-1.29) becomes

$$\left[\frac{d\sigma}{d\Omega}\right]_{\varphi=3\pi/2} \equiv D = I_o(1 + A_n R P_{ix}) \ . \qquad (A\text{-}10)$$

Dividing Eq. (A-9) by (A-10) gives

$$P_{fx} R A_n = \frac{D - U}{D + U} \equiv \epsilon_{DU} = -\epsilon_{UD} .$$

Eqs. (A-5) and (1-1.15) show that the polarization along the direction of the recoil proton (perpendicular to the plane of the analyzing material) cannot be measured. This means that, if the target is polarized in the scattering plane, R can be determined (from the up-down asymmetry) but not A. However, if the recoil protons are passed through a dipole magnet, their spins can be precessed such that P_z is rotated into the y direction. A simultaneous measurement of A and R can then be made by determining both asymmetries.

A.3 Ambiguities

A discussion of ambiguities inherent in the determination of f and g from an incomplete data set will help to clarify the need for measurements of all four of

the above parameters. If the interchange

$$f \rightarrow ig \text{ and } ig \rightarrow f,$$

is made, the differential cross section does not change. The sign of the transverse polarization (or analyzing power) does change, however, and its measurement resolves the ambiguity. A more general form of this ambiguity (known as the Minami ambiguity) is

$$f \rightarrow ig^{*} \text{ and } ig \rightarrow f^{*}$$

which has no effect on either the differential cross section or the transverse polarization; resolution of this ambiguity can come only from a measurement of A or R.

In the Yang ambiguity,

$$f \rightarrow -f \text{ and } g \rightarrow g \text{ or } f \rightarrow f \text{ and } g \rightarrow -g,$$

the differential cross section remains the same but the sign of the transverse polarization changes. A more general form of the Yang ambiguity exists:

$$f \rightarrow f^{*} \text{ and } g \rightarrow g^{*} \text{ or } f \rightarrow -f^{*} \text{ and } g \rightarrow -g^{*}.$$

In this case both the differential cross section and the transverse polarization are left unchanged and a measurement of A or R is necessary.

Finally, a measurement of A will allow a determination of the magnitude of the spin rotation angle, β, from the relation

$$A = \sqrt{(1-A_n^2)}\sin(\theta-\beta)$$

but a sign ambiguity is left. To resolve this sign ambiguity a measurement of R must also be carried out.

A.4 Summary

The determination of the scattering amplitudes f and g (apart from an overall phase) requires four measurements.

A measurement of the differential cross section from an unpolarized target yields

$$I_o = |f|^2 + |g|^2 .$$

Measurement of the recoil proton polarization of an unpolarized target (or the analyzing power of a transversely polarized) target leads to

$$I_o A_n = 2\mathrm{Re}(fg^*) .$$

Measurement of the A and R parameters gives

$$I_o A \equiv (|f|^2 - |g|^2)\sin\theta - 2\mathrm{Im}(fg^*)\cos\theta$$

$$= \sqrt{(1-A_n^2)}\sin(\theta-\beta)$$

$$I_o R \equiv (|f|^2 - |g|^2)\cos\theta + 2\mathrm{Im}(fg^*)\sin\theta$$

$$= \sqrt{(1-A_n^2)}\cos(\beta-\theta) .$$

From the above relations

$$|f|^2 - |g|^2 = I_o(R\cos\theta + A\sin\theta)$$

$$2\mathrm{Im}(fg^*) = I_o(R\sin\theta - A\cos\theta)$$

which finally gives

$$|f|^2 = \tfrac{1}{2}I_o(1 + R\cos\theta + A\sin\theta)$$

$$|g|^2 = \tfrac{1}{2}I_o(1 - R\cos\theta - A\sin\theta)$$

$$fg^* = \tfrac{1}{2}I_o(A_n + iR\sin\theta - iA\cos\theta).$$

APPENDIX B

PARTIAL-WAVE ANALYSIS

If the incident momentum is assumed to lie along the z-axis then Eq. (1-1.2) becomes

$$|\Psi_\mu\rangle = e^{ikz}|\chi_\mu\rangle + \frac{e^{ikr}}{r} M_{\nu\mu}|\chi_\nu\rangle$$

$$|\Psi_\mu\rangle = e^{ikz}|\chi_\mu\rangle + \left[f(\theta)|\chi_\mu\rangle + g(\theta,\varphi)|\chi_{-\mu}\rangle\right]\frac{e^{ikr}}{r}. \qquad \text{(B-1)}$$

The term e^{ikz} can be expanded in Legendre polynomials:

$$e^{ikz} = \sum_\ell i^\ell (2\ell+1) j_\ell(kr) P_\ell(\cos\theta) \ , \qquad \text{(B-2)}$$

where ℓ is the angular momentum quantum number and j_ℓ are the spherical Bessel functions. Since the asymptotic region of the scattering is the one of interest, $j_\ell(kr)$ can be replaced with its asymptotic value:

$$j_\ell(kr) \xrightarrow{r\to\infty} \frac{1}{kr}\sin(kr - \frac{\ell\pi}{2}). \qquad \text{(B-2)}$$

By rewriting the Legendre polynomials in terms of spherical harmonics,

$$Y_\ell(\theta,\varphi) = \left[\frac{(2\ell+1)}{4\pi}\right]^{\frac{1}{2}} P_\ell(\cos\theta) \ ,$$

and substituting into Eq. (B-2) the asymptotic values of

the spherical Bessel functions, e^{ikz} becomes

$$e^{ikz} \xrightarrow{r\to\infty} \frac{1}{kr}\sum_{\ell} i^{\ell}\sqrt{4\pi(2\ell+1)}\sin(kr - \frac{\ell\pi}{2})Y_{\ell}^{0}(\theta,\varphi)$$

$$= \frac{1}{2ikr}\sum_{\ell} i^{\ell}\sqrt{4\pi(2\ell+1)}\left[e^{ikr}-(-1)^{\ell}e^{-ikr}\right] Y_{\ell}^{0}(\theta,\varphi).$$

The amplitudes f and g can be expanded in spherical harmonics:

$$f(\theta) = \sum_{\ell=0}^{\infty} f_{\ell}Y_{\ell}^{0}(\theta,\varphi)$$

$$g(\theta,\varphi) = \sum_{\ell=1}^{\infty} g_{\ell}Y_{\ell}^{2m_s}(\theta,\varphi) \ ;$$

where $-s \le m_s < s$, and s is the spin quantum number of the particle. Eq. (B-1) finally becomes

$$|\Psi_{\mu}\rangle = \frac{i}{2kr}e^{-ikr}\sum_{\ell,j}(-1)^{\ell}\sqrt{4\pi(2\ell+1)}|\chi_m\rangle Y_{\ell}^{0} -$$

$$\frac{i}{2kr}e^{ikr}\sum_{\ell,j}\left[(\sqrt{4\pi(2l+1)} + 2ikf_{\ell})|\chi_m\rangle Y_{\ell}^{0} + 2ikg_{\ell}|\chi_{-m}\rangle Y_{\ell}^{2m_s}\right].$$

The first term on the right represents an incoming spherical wave while the second term represents an outgoing spherical wave. For elastic scattering the total incoming flux must equal the total outgoing flux. Since angular momentum is conserved, this conservation of probability must hold for each independent ℓ. This means that the amplitudes for the incoming and outgoing waves must be

equal (apart from a phase factor):

$$\left[f_\ell + \frac{\sqrt{4\pi(2\ell+1)}}{2ik}\right]|\chi_m\rangle Y_\ell^0 + g_\ell|\chi_{-m}\rangle Y_\ell^{2m_s}$$

$$= e^{2\delta_{\ell j}} \frac{\sqrt{4\pi(2\ell+1)}}{2ik} |\chi_m\rangle Y_\ell^0 \ .$$

The quantity $\delta_{\ell j}$ is known as the phase shift.[40] Because the scattering is invariant under rotation, the phase shift does not depend on m.

If the partial-wave amplitude is defined as

$$a_{\ell j} = \frac{1}{2i}\left[e^{2i\delta_{\ell j}} - 1\right] = e^{i\delta_{\ell j}} \sin\delta_{\ell j} \ ,$$

then

$$f_\ell|\chi_m\rangle Y_\ell^0 + g_\ell|\chi_{-m}\rangle Y_\ell^{2m_s} = \frac{\sqrt{4\pi(2\ell+1)}}{k} a_{\ell j} |\chi_m\rangle Y_\ell^0 \ . \qquad \text{(B-4)}$$

Now the spinors and spherical harmonics can be rewritten in terms of the Clebsch-Gordan coefficients $\langle \ell, m_\ell; s, m_s | j, m_j\rangle$ as[40]

$$|\chi_m\rangle Y_\ell^0 = \sum_{\ell=j+\frac{1}{2}} \langle \ell, 0; \tfrac{1}{2}, m_s | j, m_s\rangle |j, m_s\rangle \ ,$$

$$|\chi_{-m}\rangle Y_\ell^{2m_s} = \sum_{\ell=j+\frac{1}{2}} \langle \ell, 2m_s; \tfrac{1}{2}, -m_s | j, m_s\rangle |j, m_s\rangle \ .$$

Substitution into equation (B-4) gives

$$f_\ell \langle \ell, 0; \tfrac{1}{2}, m_s | j, m_s \rangle + g_\ell \langle \ell, 2m_s; \tfrac{1}{2}, -m_s | j, m_s \rangle$$

$$= \frac{\sqrt{4\pi(2\ell+1)}}{k} a_{\ell j} \langle \ell, 0; \tfrac{1}{2}, m_s | j, m_s \rangle \ .$$

The above expression is now multiplied by $\langle \ell, 0; \frac{1}{2}, m_s | j, m_s \rangle$ and summed over j; evaluating the Clebsch-Gordan coefficients, an expression for f_ℓ is obtained:

$$f_\ell = \frac{1}{k} \left[\frac{4\pi}{2\ell+1}\right]^{\frac{1}{2}} [(\ell+1)a_{\ell,\ell+\frac{1}{2}} + \ell a_{\ell,\ell-\frac{1}{2}}] . \qquad \text{(B-5)}$$

If the multiplication factor is instead $\langle \ell, 2m_s; \frac{1}{2}, -m_s | j, m_s \rangle$ and then the summation over j is performed, an expression for g_ℓ is obtained:

$$g_\ell = \frac{1}{k} \left[\frac{4\pi}{2\ell+1}\right]^{\frac{1}{2}} \sqrt{\ell(\ell+1)}(a_{\ell,\ell+\frac{1}{2}} - a_{\ell,\ell-\frac{1}{2}}) . \qquad \text{(B-6)}$$

If low-energy scattering is assumed so that only s and p waves are important, then the unpolarized differential cross section is equal to

$$I_0 = |f|^2 + |g|^2$$

$$= |\Sigma f_\ell Y_\ell^0|^2 + |\Sigma g_\ell Y_\ell^{2m}|^2 .$$

$$= |f_0 Y_0^0 + f_1 Y_1^0|^2 + |g_1 Y_1^1|^2 . \qquad \text{(B-7)}$$

By evaluating the above amplitudes from Eqs. (B-5) and (B-6), and explicitly writing out the spherical harmonics;

$$f_0 = \left[\frac{4\pi}{k^2}\right]^{\frac{1}{2}} a_{0,1/2} \ ; \qquad Y_0^0 = \left[\frac{1}{4\pi}\right]^{\frac{1}{2}}$$

$$f_1 = \left[\frac{4\pi}{3k^2}\right]^{\frac{1}{2}}(2a_{1,3/2} + a_{1,1/2}), \qquad Y_1^0 = \left[\frac{3}{4\pi}\right]^{\frac{1}{2}}\cos\theta$$

$$g_1 = \left[\frac{4\pi}{3k^2}\right]^{\frac{1}{2}}(a_{1,3/2} - a_{1,1/2}) . \qquad Y_1^1 = -\left[\frac{3}{8\pi}\right]^{\frac{1}{2}} e^{i\varphi}\sin\theta;$$

Eq. (B-7) becomes

$$I_o = \frac{1}{k^2}\left[|a_{0,1/2} + (2a_{1,3/2}+a_{1,1/2})\cos\theta|^2 + |(a_{1,3/2}-a_{1,1/2})\sin\theta|^2\right] .$$

$$= \frac{1}{k^2}\left\{ |a_{0,1/2}|^2 + |a_{1,3/2}-a_{1,1/2}|^2 + 2\mathrm{Re}[a^*_{0,1/2}(2a_{1,3/2}+a_{1,1/2})]\cos\theta + \left[|2a_{1,3/2}+a_{1,1/2}|^2 - |a_{1,3/2}-a_{1,1/2}|^2\right]\cos^2\theta \right\}.$$

If three parameters are defined such that

$$A = |a_{0,1/2}|^2 + |a_{1,3/2}-a_{1,1/2}|^2$$

$$B = 2\mathrm{Re}[a^*_{0,1/2}(2a_{1,3/2}+a_{1,1/2})]$$

$$C = |2a_{1,3/2}+a_{1,1/2}|^2 - |a_{1,3/2}-a_{1,1/2}|^2 ,$$

then I_o can be written in a simpler form:

$$I_o = \frac{1}{k^2}(A + B\cos\theta + C\cos^2\theta) \qquad \text{(B-8)}$$

From Eq. (1-1.18),

$$I_o P = (f^* g + f g^*) = \mathrm{Re}(f^* g) \ .$$

A similar calculation to the one above gives

$$I_o P = \frac{-2}{k^2} \mathrm{Im}[(D + E\cos\theta) F^* \sin\theta] \ , \qquad \text{(B-9)}$$

where

$$D = a_{0,1/2} \ ,$$

$$E = a_{1,3/2} + a_{1,1/2} \ ,$$

$$F = a^*_{1,3/2} - a^*_{1,1/2} \ .$$

If higher partial waves are included higher-order terms in $\cos\theta$ are obtained.

Equations (B-8) and (B-9) contain the essence of partial-wave analysis. By making a fit to the total data available on the πN interaction parameters such as A through F can be determined. These parameters are related to the phase shifts which, in turn, are related to the scattering amplitudes. A determination of a functional form for $f(\theta)$ and $g(\theta,\varphi)$ can therefore be made.

APPENDIX C

DISPERSION RELATIONS

C.1 General Formalism

For a function of a complex variable, $f(\eta)$, that is analytic in the upper half of the complex plane ($\mathrm{Im}\eta > 0$) Cauchy's theorem states

$$f(\eta) = \frac{1}{2\pi i}\int_C \frac{f(\eta')}{(\eta'-\eta)}\,d\eta'$$

where the integration is along the closed contour consisting of a segment of the real axis from $\eta'=-R$ to $\eta'=R$ closed by a semicircle of radius R in the upper half plane, and where η lies within the contour C.[41] If $f(\eta)$ vanishes sufficiently rapidly for large $|\eta|$, the semicircle will not contribute to the integra' as $R\to\infty$, and

$$f(\eta) = \frac{1}{2\pi i}\int_{-\infty}^{\infty} \frac{f(\eta')}{(\eta'-\eta)}\,d\eta' .$$

By writing $\eta \to \zeta \pm i\epsilon$, where ζ and ϵ are real ($\epsilon>0$), and taking the limit $\epsilon\to 0$, the identity

$$\frac{1}{(\zeta'-\zeta\mp i\epsilon)} \equiv P\,\frac{1}{(\zeta'-\zeta)} \pm i\pi\delta(\zeta'-\zeta),$$

where the P indicates that the principal value of the

integral is to be taken, can be used:

$$f(\zeta) = \frac{1}{\pi i} P \int_{-\infty}^{\infty} \frac{f(\zeta')}{(\zeta'-\zeta)} d\zeta' .$$

The real and imaginary parts of the above equation can be equated to find

$$\text{Re } f(\zeta) = \frac{1}{\pi} P \int_{-\infty}^{\infty} \frac{\text{Im } f(\zeta')}{\zeta'-\zeta} d\zeta' \qquad (C-1)$$

$$\text{Im } f(\zeta) = -\frac{1}{\pi} P \int_{-\infty}^{\infty} \frac{\text{Re } f(\zeta')}{\zeta'-\zeta} d\zeta' . \qquad (C-2)$$

Equations (C-1) and (C-2) are known as dispersion relations.[41] The name comes from the fact that they were first derived by Kronig and Kramers to relate the refractive and absorptive part of the refractive index at different frequencies, but the term is applied to any such integral relationship between real and imaginary parts of a complex function.

If the physical range of the interaction runs along the positive part of the real axis ($\zeta>0$) and if $f(-\zeta) = +f^*(\zeta)$ (even symmetry), then, for Ref(ζ):

$$f(\zeta) = \frac{1}{\pi i} \int_{\infty}^{0} \frac{f^*(\zeta')}{(\zeta'+\zeta)} d\zeta' + \frac{1}{\pi i} P \int_{0}^{\infty} \frac{f(\zeta')}{(\zeta'-\zeta)} d\zeta'$$

$$\Rightarrow \text{Re } f(\zeta) = \frac{1}{\pi} P \int_{\infty}^{0} \frac{\text{Im} f(\zeta')}{\zeta'+\zeta} d\zeta' - \frac{1}{\pi} P \int_{0}^{\infty} \frac{\text{Im} f(\zeta')}{\zeta'-\zeta} d\zeta'$$

$$= \frac{1}{\pi} P \int_{\zeta}^{\infty} \text{Im} f(\zeta') \left\{ \frac{1}{\zeta'+\zeta} - \frac{1}{\zeta'-\zeta} \right\} d\zeta' . \qquad (C-3)$$

Similar results hold for $f(-\zeta) = -f^*(\zeta)$ (odd symmetry).

If $f(\zeta)$ is analytic everywhere except for a pole inside the contour and for branch lines from $+\zeta$ to ∞ and $-\zeta$ to ∞ then the above equations can be generalized. Specifically, for equation (C-3):

$$\text{Re } f(\zeta) = \begin{matrix}\text{Residue} \\ \text{at pole}\end{matrix} + \frac{1}{\pi} P \int_{\zeta}^{\infty} \text{Im} f(\zeta') \left\{ \frac{1}{\zeta' + \zeta} - \frac{1}{\zeta' - \zeta} \right\} d\zeta' \quad . \quad \text{(C-4)}$$

C.2 <u>πN Scattering</u>

Dispersion relations can be written for the πN scattering amplitudes. However, the two amplitudes defined in Section 1 are not Lorentz invariant and, therefore, do not form a natural starting point for dispersion theory.

In order to construct Lorentz invariant amplitudes, the Dirac theory must be used. In this relativistic theory the nucleon spin properties are described by four-component Dirac spinors $u(\vec{p},s)$ where $\vec{p}$ is the momentum and s the spin of the particle. The normalization condition

$$u^{t}(\vec{p},s)u(\vec{p},s) = \frac{E}{m} ,$$

$$\bar{u}(\vec{p},s)u(\vec{p},s) = u^{t}(\vec{p},s)\gamma^{0}u(\vec{p},s) = 1,$$

where E and m are the energy and mass of the nucleon, respectively, will be adopted.

The invariant transition matrix, T_{fi}, for scattering from an initial state i with pion four-momentum k_i, nucleon four-momentum p_i, and spin s to a final state f with pion

four-momentum k_f, nucleon four-momentum p_f, and spin r is

$$T_{fi} = \frac{m}{16\pi^2}\bar{u}(\vec{p}_f, r)M(k_i, p_i; k_f, p_f)u(\vec{p}_i, s) \ .$$

M is now a 4×4 matrix that can be expanded in terms of the sixteen independent Dirac matrices:

$$M = A + \gamma^{\mu}B_{\mu} + \sigma^{\mu\nu}C_{\mu\nu} + D_{\mu}\gamma^{\mu}\gamma_5 + E\gamma_5 \ ,$$

where the summations are implied. The quantities A to E transform like a scalar, vector, second-rank tensor, pseudovector, and pseudoscalar, respectively.[39] The only two quantities available to construct A to E are k_i and p_i. Because of four-momentum conservation, only three of the quantities k_i, k_f, p_i, and p_f are independent, and we can form the following combinations:

$$P = \tfrac{1}{2}(p_i + p_f), \quad Q = \tfrac{1}{2}(k_i + k_f),$$

$$K = \tfrac{1}{2}(k_i - k_f) = \tfrac{1}{2}(p_f - p_i).$$

No pseudoscalar or pseudovector can be formed from P, Q, and K, so E and D must be equal to zero.[39] The tensor term C can be reduced to scalar or vector terms like A or B_{μ}.[39] The term B_{μ} could be of the form $(BQ_{\mu}+B'P_{\mu}+B''K_{\mu})$, but terms like $\gamma_{\mu}P_{\mu}$ and $\gamma_{\mu}K_{\mu}$ can be reduced to scalar terms like A through the Dirac equation.[39] The only surviving terms of M are then of the form

$$M = A + (\gamma^{\mu}Q_{\mu})B \qquad (C\text{-}5)$$

where A and B are independent invariants, which are functions of two scalars determined by the center-of-mass

energy, W, and the center-of-mass scattering angle, θ_{cm}. The fact that the number of independent amplitudes is two already followed from Chap. 1, and we can relate A and B to $f(\theta)$ and $g(\theta,\varphi)$.

The elastic scattering amplitude in the center-of-mass system, $F(\theta,\varphi)$, is

$$F(\theta,\varphi) = \frac{4\pi}{W} T_{fi} =$$

$$\left[\frac{m}{4\pi W}\right] [u(\vec{k}_f, s_f)\gamma^0 \{A + \tfrac{1}{2}\gamma^\mu (k_{\mu f}+k_{\mu i})B\}u(\vec{k}_i, s_i)] \ .$$

Let q_f and q_i be defined as follows:

$$\vec{q}_i = \vec{p}_i = -\vec{k}_i; \quad \vec{q}_f = -\vec{k}_f = \vec{p}_f \ .$$

For elastic scattering $|\vec{q}_i| = |\vec{q}_f| = q$.

The Dirac spinor can be written in terms of the two-dimensional Pauli spinor $\chi(s)$,

$$u(\vec{p},s) = \begin{bmatrix} (E+m)\chi(s) \\ (\vec{\sigma}\cdot\vec{p})\chi(s) \end{bmatrix} ,$$

so that the scattering amplitude becomes[39]

$$F(\theta,\varphi) = \chi^t(s_f) \left[f_1 + f_2 \frac{1}{q^2}(\vec{\sigma}\cdot\vec{q}_i)(\vec{\sigma}\cdot\vec{q}_f)\right]\chi(s_i) \ . \qquad \text{(C-6)}$$

The quantities f_1 and f_2 are defined by

$$f_1 = \frac{E+m}{8\pi W} [A + (W-m)B]$$

$$f_2 = -\frac{E-m}{8\pi W} [A - (W+m)B]$$

and E is the center-of-mass energy of the nucleon:

$$E = (m^2 + q^2)^{\frac{1}{2}} .$$

Substituting the relation

$$(\vec{\sigma}\cdot\vec{q}_i)(\vec{\sigma}\cdot\vec{q}_f) = \vec{q}_i\cdot\vec{q}_f + i\vec{\sigma}\cdot(\vec{q}_i\times\vec{q}_f)$$

$$= q^2[\cos\theta + i\vec{\sigma}\cdot(\hat{i}\times\hat{f})]$$

into Eq. (C-6) gives

$$F(\theta,\varphi) = \chi^{\dagger}(s_f)\left[f_1 + f_2[\cos\theta + i\vec{\sigma}\cdot(\hat{i}\times\hat{f})]\right]\chi(s_i) , \qquad (C-7)$$

where $\hat{i}$ and $\hat{f}$ are unit vectors in the direction of $\vec{q}_i$ and $\vec{q}_f$, respectively.

From Chap. 1

$$M = f + g\vec{\sigma}\cdot\hat{n} .$$

This equation was derived in the lab system, but it holds equally well in the center-of-mass system:

$$M = f + g\vec{\sigma}\cdot\frac{\vec{q}_i\times\vec{q}_f}{|\vec{q}_i\times\vec{q}_f|} = f + g\vec{\sigma}\cdot(\hat{i}\times\hat{f}) . \qquad (C-8)$$

A comparison of Eqs. (C-7) and (C-8) shows that

$$f = f_1 + f_2\cos\theta$$

$$g = if_2\sin\theta .$$

It is convenient to define three invariant scalars:

$$s = (k_i + p_i)^2 = (k_f + p_f)^2$$

$$t = (k_i - k_f)^2 = (p_i - p_f)^2$$

$$u = (k_i - p_f)^2 = (p_i - k_f)^2 .$$

The three scalars (called Mandelstam variables) are not independent, but are connected by the relation:

$$s + t + u = 2(m^2 + \mu^2) \qquad (C-9)$$

where m is the mass of the nucleon and μ is the mass of the pion. In the center-of-mass system, s is the square of the center-of-mass energy W, and t is the negative of the square of the momentum transfer. Another variable, ν, can be defined, where

$$\nu = \frac{1}{4m}(s-u) . \qquad (C-10)$$

Solving Eq. (C-9) for u and substituting into Eq. (C-10) gives

$$\nu = \frac{1}{2m}(s - m^2 - \mu^2 + t/2) . \qquad (C-11)$$

Rewriting s in terms of center-of-mass quantities gives

$$s = W^2 = \left[(q^2+m^2)^{\frac{1}{2}} + (q^2+\mu^2)^{\frac{1}{2}}\right]^2 ,$$

$$s = 2q^2 + m^2 + \mu^2 + 2(q^2+m^2)^{\frac{1}{2}}(q^2+\mu^2)^{\frac{1}{2}} . \qquad (C-12)$$

In terms of lab quantities s becomes

$$s = m^2 + \mu^2 + 2m\omega \ , \qquad \text{(C-13)}$$

where ω is the pion energy in the lab. Solving Eq. (C-13) for ω,

$$\omega = \frac{1}{2m}(s - m^2 - \mu^2) \ . \qquad \text{(C-14)}$$

Substituting this expression into Eq. (C-11) yields

$$\nu = \omega + \frac{1}{4m}t \ . \qquad \text{(C-15)}$$

Substitution of Eq. (C-12) into Eq. (C-14) and the result into Eq. (C-15) gives

$$m\nu = q^2 + (q^2+m^2)^{\frac{1}{2}}(q^2+\mu^2)^{\frac{1}{2}} + \frac{t}{4} \ . \qquad \text{(C-16)}$$

In the center-of-mass system

$$t = -2q^2(1 - \cos\theta_{cm});$$

for physical scattering t must be negative. Since $|\cos\theta_{cm}| \leq 1$, $q^2 \geq -t/4$ for fixed negative t. Therefore, Eq. (C-16) becomes

$$m\nu > \left[(m^2 - \frac{t}{4})(\mu^2 - \frac{t}{4})\right]^{\frac{1}{2}} \equiv \nu_1 \ . \qquad \text{(C-17)}$$

A bound state (corresponding to a neutron) occurs in the $\pi^- p$ system. In the laboratory frame, $E_n = E_p + \omega$, $E_p = m$, $E_n = (p^2+m^2)^{\frac{1}{2}}$, and $\omega = (p^2+\mu^2)^{\frac{1}{2}}$. Solving these

relations for ω yields

$$\omega = \pm \frac{\mu^2}{2m} \quad ,$$

where the plus sign corresponds to π^+ scattering and the minus sign corresponds to π^- scattering. Substituting into Eq. (C-15) gives

$$\nu = \left[\frac{t}{4m} \pm \frac{\mu^2}{2m}\right] \equiv \nu_B \quad . \qquad \text{(C-18)}$$

The minus sign is used because this pole corresponds to a neutron which can only be produced by π^- scattering. Since $|\omega| < \mu$ this energy is inaccessible and lies in the non-physical region of ν.

C.3 <u>πN Dispersion Relations</u>

If a fixed, non-zero value for the momentum transfer, t, is assumed, then a particle moving forward in time with energy ω can be thought of as an anti-particle moving backward in time with energy $-\omega$. For π^+p elastic scattering, changing ω to $-\omega$ is equivalent to "crossing" the π^+p reaction to get π^-p scattering with a pion of incoming momentum $-\vec{k}_f$ and a pion of outgoing momentum $-\vec{k}_i$. Since the transition matrix is hermitian,[39] it follows that

$$\langle k_i, p_i | T^+ | k_f, p_f \rangle = \langle -k_f, p_i | T^- | -k_i, p_f \rangle^* \quad ,$$

where T^+ is the matrix for π^+ and T^- is the matrix for π^-. By crossing the reaction, s and u have been interchanged,

which means that $\nu \to -\nu$, and

$$\Rightarrow T^{+}(\nu,t) = T^{-*}(-\nu,t) \ .$$

Since A transforms as a scalar and B transforms as a vector:

$$A^{\pm}(-\nu,t) = {}^{\pm}A^{*}(\nu,t)$$

$$B^{\pm}(-\nu,t) = {}^{\mp}B^{*}(\nu,t) \ .$$

The following fixed-t dispersion relations for A and B can therefore be written:

$$\text{Re } A^{\pm}(\nu,t) = \begin{matrix}\text{Residue} \\ \text{at pole}\end{matrix} + \frac{1}{\pi} P \int_{\nu_1}^{\infty} \text{Im}A(\nu') \left\{ \frac{1}{\nu'+\nu} \pm \frac{1}{\nu'-\nu} \right\} d\nu' ,$$

$$\text{Re } B^{\pm}(\nu,t) = \begin{matrix}\text{Residue} \\ \text{at pole}\end{matrix} + \frac{1}{\pi} P \int_{\nu_1}^{\infty} \text{Im}B(\nu') \left\{ \frac{1}{\nu'+\nu} \mp \frac{1}{\nu'-\nu} \right\} d\nu' ,$$

where

$$\nu_1 = \left[\frac{\mu^2}{2m} - \frac{t}{4m} \right] \ .$$

It can be shown that the neutron pole contains a factor of $\not{\epsilon}_\mu$;[39] it therefore only contributes to the amplitude B.

The bound state inside the contour can be accounted for by adding a Breit-Wigner resonance B and letting the width, Γ, approach zero:[42]

$$B^{B}(\nu,t) = \lim_{\Gamma \to 0} \frac{\Gamma}{(\omega - \mu^2/2m) + i\Gamma/2}$$

$$\Rightarrow \text{Im } B^{B}(\nu,t) = \lim_{\Gamma \to 0} \frac{\Gamma^2/2}{(\omega - \mu^2/2m)^2 + \Gamma^2/4} = 2\pi\delta(\omega - \mu^2/2m).$$

Evaluating the residue and substituting into the dispersion relation yields

$$\text{Re } B^{\pm}(\nu,t) = \frac{g^2}{2M}\left[\frac{1}{(\nu_B-\nu)} - \frac{1}{(\nu_B+\nu)}\right] + \frac{1}{\pi} P \int_{\nu_t}^{\infty} \text{Im}B(\nu') \left\{\frac{1}{\nu'+\nu} \mp \frac{1}{\nu'-\nu}\right\} d\nu' ,$$

where g is the πN pseudovector coupling constant and is determined from experiment.[42]

It is convenient to introduce another scattering amplitude, C, that is a combination of A and B:

$$C(\nu,t) = A(\nu,t) + \frac{\nu}{1 - (t/4m^2)} B(\nu,t)$$

Using the optical theorem the imaginary part of C can be related to the total cross sections for forward scattering (θ=0 => t=0):

$$\text{Im}C(\nu,0) = k\sigma .$$

By experimentally determining the total cross sections for $\pi^{\pm}$p elastic scattering at θ=0 the imaginary part of the scattering amplitude can be determined;[42] substitution of these values into the dispersion relations gives values for the real part of the scattering amplitudes which can then be compared to the values determined by phase shifts.

REFERENCES

1. T. Barnes and F.E. Close, Phys. Lett. 123B, 89 (1983).

2. J.D. Breit and C.R. Nappi, Phys. Rev. Lett. 53, 889 (1984).

3. K.C. Bowler and A.J.G. Hey, Phys. Lett. 69B, 469 (1977).

4. J. Carlson, J.B. Kogut, and V.R. Pandharipande, Phys. Rev. D28, 2807 (1983).

5. A. Chodos, R.L. Jaffe, K. Johnson, C.F. Thorn, and V.F. Weisskopf, Phys. Rev. D9, 3471 (1974).

6. F.E. Close and R.R. Horgan, Nucl. Phys. B164, 413 (1980).

7. T.A. DeGrand and C. Rebbi, Phys. Rev. D17, 2358 (1978).

8. A. DeRujula, H. Georgi, and S.L. Lashow, Phys. Rev. D12, 147 (1975).

9. G. Eckart, A. Hayashi, and G. Holzwarth, Nucl. Phys. A448, 732 (1986).

10. E. Golowich, E. Haqq, and G. Karl, Phys. Rev. D28, 160 (1983).

11. A. Hayashi et al., Phys. Lett. 147B, 5 (1984).

12. N. Isgur and G. Karl, Phys. Rev. D19, 2653 (1979).

13. M.P. Mattis and M. Karliner, Phys. Rev. D31, 2833 (1985).

14. Eric Umland, Ian Duck, and W. von Witsch, Phys. Rev. D27, 2678 (1983).

15. R.E. Cutkosky et al., Phys. Rev. D20, 2804 (1979).

16. G.H. Hohler et al., Handbook of Pion-Nucleon Scattering, Physics Data 12-1, Karlsruhe, Germany (1979); Pion-Nucleon Scattering: Phenomenological Analyses, Landolt-Bornstein Vol. I/9b2, Springer-Verlag, Berlin (1983).

17. R.A. Arndt, L.D. Roper, and J. Ford, Phys. Rev. D32, 1085 (1985).

18. F.O. Borcherding, PhD Thesis, UCLA (1982).

19. G.J. Kim, PhD Thesis, UCLA (1988), and to be published in Phys. Rev. D.

20. A. Mokhtari et al.,, Phys. Rev. D35, 810 (1987).

21. M.E. Sadler et al., Phys. Rev. D35, 2718 (1987).

22. J.A. Wightman et al., Phys. Rev. D36, 3529 (1987).

23. M.E. Sadler, Proceedings of the Conference on Physics with Light Mesons and the Second International Workshop on πN Physics, LANL Report LA-11184-C, 200 (1987).

24. J.J. Sakurai, Invariance Principles and Elementary Particle Physics, Princeton University Press, NJ (1964).

25. N.W. Dean and Ping Lee, Phys. Rev. D5, 2741 (1972).

26. W.J. Briscoe et al., Nucl. Instrum. and Meth. 197, 277 (1982).

27. M. Kellogg et al., Introduction to Q, LASL Report, LA-7001-M (1978).

28. M.W. McNaughton, Introduction to the LAMPF Recoil Polarimeter (JANUS), LANL Report X100-01 (1985).

29. L.G. Atencio et al., Nucl. Instr. and Meth. 187, 381 (1981).

30. A. Breskin, G. Charpak, and F. Sauli, Nucl. Instr. Meth. 151, 473 (1977).

31. M.W. McNaughton et al., Nucl. Instr. Meth. A241, 435 (1985).

32. G. Waters et al., Nucl. Instr. Meth. 153, 401 (1978).

33. E. Aprile-Giboni et al., Nucl. Instr. Meth. 216 (1983).

34. Particle Data Group, Phys. Lett. 170B, 44 (1986).

35. D. Besset et al., Nucl. Instr. Meth. 166,515 (1979).

36. Bareyre, Phys. Rev. Lett. 14, 199 (1965).

37. Bareyre, Phys. Rev. Lett. 14, 878 (1965).

38. G.H. Hohler, private communication

39. B.H. Bransden and R.G. Moorhouse, The Pion-Nucleon System, Princeton University Press, NJ (1973).

40. G. Kallen, Elementary Particle Physics, Addison-Wesley, MA (1964).

41. L.M. Jones, An Introduction to Mathematical Methods of Physics, The Benjamin/Cummings Publishing Co., CA (1979).

42. R.J. Cence, Pion-Nucleon Scattering, Princeton University Press, NJ (1969).

ACKNOWLEDGEMENTS

I would like to thank my co-advisors, Dr. Bill Briscoe and Dr. Morty Taragin, for their much needed help, support, and guidance throughout this experiment and my graduate education. I would also like to thank them for allowing me, over the years, to do things the way I thought they should be done and not the way others wanted me to do them, and for putting up with me. I am also very much indebted to Dr. Ali Mokhtari for his invaluable help with every aspect of this thesis, and for sticking around long enough to make sure I didn't get into too much trouble. I am grateful to Dr. Dan Sober for his many helpful comments and suggestions concerning the writing of this dissertation.

Most experiments concerning nuclear physics could not be successfully completed without the help of many individuals, and my experiment was no exception. Among them were Dr. Ben Nefkens, who conceived the original experimental program of which this experiment was part, and Dr. Mike Sadler, whose contributions of time and experience were greatly appreciated. Dr. Chandra Pillai, Dr. Dave Barlow, Steve Adrian, and Anton Bergmann also contributed much to the success of this experiment.

I am grateful to Dr. Mike McNaughton for explaining the ins and outs of how a polarimeter worked to those of us who originally had no idea and for allowing me to reprint Figs. 2-6, 2-7, and 4-14. I am also indebted to: Dr. Kok Heong McNaughton for patiently answering all of our questions concerning JANUS software; Dr. J. C. Peng for providing beam tunes and the pion momentum derivation given in Sec. 4.1.8; Dr. Peter Gram for his assistance with the LAS spectrometer; and to Norm Hoffman and the target group. As always, MP7, MP8, and MP-13 (now MP-5) provided excellent assistance.

Figs. 2-1, 2-2, and 2-3 were obtained from LAMPF. Support for this work was provided by NSF grant PHYS-8604524. Funds necessary for the purchase and maintenance of the MicroVAX were provided by NSF grant PHYS-8700306.